

**Exploring Spontaneous Emission Phenomena  
using Ultracold Atomic Matter Waves**

A Dissertation presented

by

**Ludwig Krinner**

to

The Graduate School

in Partial Fulfillment of the

Requirements

for the Degree of

**Doctor of Philosophy**

in

**Physics**

Stony Brook University

**August 2018**

**Stony Brook University**

The Graduate School

**Ludwig Krinner**

We, the dissertation committee for the above candidate for the  
Doctor of Philosophy degree, hereby recommend  
acceptance of this dissertation.

Dominik Schneble - Dissertation Advisor  
Associate Professor, Department of Physics and Astronomy

Philip Allen - Chairperson of Defense  
Professor Emeritus, Department of Physics and Astronomy

Eden Figueroa  
Assistant Professor, Department of Physics and Astronomy

Andrew Daley  
Professor, Department of Physics and SUPA  
University of Strathclyde

This dissertation is accepted by the Graduate School.

Dean of the Graduate School

Abstract of the Dissertation

# Exploring Spontaneous Emission Phenomena using Ultracold Atomic Matter Waves

by

**Ludwig Krinner**

**Doctor of Philosophy**

in

**Physics**

Stony Brook University

**2018**

The controllability of ultracold quantum gases in optical lattices offers new perspectives on problems in various subfields of physics. In this dissertation, we study spontaneous emission, a fundamental concept in quantum electrodynamics, using engineered emitters, realized with  $^{87}\text{Rb}$  atoms in a hyperfine ground state selective optical lattice (a lattice potential that confines one internal hyperfine ground state without confining the other), that send single atoms into one-dimensional matter-waveguides. On a fundamental level, each emitter is described by the Weisskopf-Wigner model. The system allows for easy tunability of the coupling strength and excited state energy, allowing the direct observation of how Markovian dynamics, giving rise to the usually observed exponential decay, transform into non-Markovian dynamics as the excited state energy approaches the coupling strength. This has allowed the first direct observation of a bound state, which was long predicted to exist for spontaneous emission in the context of photonic bandgap materials. We

study its spatial characteristics in momentum-space and are able to infer its real-space extent.

The ability to carry out these experiments in our apparatus depends on two technical developments. First is the development of a technique which allows a precise characterization of magnetic fields at Gauss-level fields used in our apparatus. This is achieved by utilizing transitions to unused hyperfine states, which creates a ‘tag’ that characterizes the field at the position of the atoms at the time of the experiment to an accuracy of better than  $100 \mu\text{G}$  for every single experimental repetition. This allows post-selection stabilization on a level which is comparable to state-of-the-art active stabilization techniques. The second development is an image analysis technique which allows for the removal of spurious unwanted fringes in our absorption images, which allows a reliable detection of small (on the order of several hundred) atom number.

The experimental work presented in this dissertation realizes a platform for future studies of dissipative many-body physics in ultraold atomic gases mirroring one of the current frontiers in quantum optics.

# Contents

<b>1</b>	<b>Introduction</b>	<b>1</b>
<b>2</b>	<b>Theoretical and Experimental Basics</b>	<b>7</b>
2.1	BEC in the Schneble Laboratory . . . . .	7
2.1.1	Laser Cooling and Magneto Optical Trapping . . . . .	8
2.1.2	Magnetic Trapping . . . . .	10
2.1.3	Optical Trapping . . . . .	12
2.1.4	Evaporative Cooling . . . . .	13
2.1.5	Achieving BEC . . . . .	14
2.2	Condensates in Optical Lattices . . . . .	18
2.2.1	Optical BEC, Detection and Optical Schematic . . . . .	18
2.2.2	Optical Lattices and Lattice Calibration Using Talbot Kicking . . . . .	20
2.2.3	Hyperfine-State Rabi Oscillations . . . . .	24
2.2.4	Hyperfine Structure in Magnetic Fields . . . . .	27
2.2.5	State-Selective Trapping Potential . . . . .	28
2.2.6	Bose-Hubbard Model and Interacting Bosons . . . . .	31
<b>3</b>	<b>Experimental Upgrades</b>	<b>36</b>
3.1	Laser Cooling and Trapping . . . . .	36
3.2	Rubidium Source . . . . .	37
3.3	Optical Pumping . . . . .	42
3.4	Quadrupole Magnetic Coils . . . . .	46
3.5	Evaporation Speed Increase . . . . .	47
3.6	Summary and Current Performance . . . . .	47
<b>4</b>	<b>Image Analysis</b>	<b>49</b>
4.1	Backgrounds and Fringes . . . . .	49
4.2	Reference Fringes . . . . .	50
4.3	Principal Component Analysis . . . . .	50

4.4	Discussion of Errors . . . . .	52
4.5	Results . . . . .	55
<b>5</b>	<b>In-Situ Magnetometry</b>	<b>61</b>
5.1	Introduction . . . . .	61
5.2	Method and Implementation . . . . .	62
5.2.1	Principle of Operation . . . . .	62
5.2.2	Experimental Implementation . . . . .	64
5.3	Characterization of Performance . . . . .	66
5.3.1	Slow Rabi Cycling . . . . .	66
5.3.2	Theoretical Accuracy & Operation Range . . . . .	68
5.4	Application: Spectroscopy of State - Selective Optical Lattices	69
5.5	Conclusions . . . . .	71
<b>6</b>	<b>Review of the Weisskopf-Wigner Model</b>	<b>72</b>
6.1	Electric Dipole Hamiltonian . . . . .	72
6.2	Field Quantization and Weisskopf-Wigner Hamiltonian . . . . .	74
6.3	Decay Rate and Lamb Shift . . . . .	75
<b>7</b>	<b>Spontaneous Emission of Matter Waves from a Tunable Open Quantum System</b>	<b>77</b>
7.1	Introduction . . . . .	77
7.2	Introduction to the System . . . . .	79
7.3	Sample Preparation . . . . .	81
7.4	Markovian Dynamics . . . . .	82
7.5	Non-Markovian Dynamics . . . . .	85
7.6	Experimental Details . . . . .	88
7.6.1	Experimental Procedures . . . . .	88
7.6.2	Characterization of Magnetic Fields and Optical Potentials	89
7.6.3	Background Subtraction . . . . .	93
7.6.4	Energy Shift Data . . . . .	94
7.7	Numerical Simulation of Array Effects in Weak Harmonic Trapping Potential . . . . .	95
7.8	(*) Comparison to Non-Adiabatic Diffraction . . . . .	98
<b>8</b>	<b>Conclusion and Outlook</b>	<b>99</b>
	<b>Bibliography</b>	<b>101</b>
	<b>Appendix A Simulation of Mean-Field Shift</b>	<b>123</b>

<b>Appendix B Other Measurements</b>	<b>125</b>
B.1 Controlling the Scattering Length: Interspecies Feshbach Resonances . . . . .	125
B.2 Measuring Mott-Shell Populations . . . . .	128
<b>Appendix C Electronics</b>	<b>129</b>
C.1 AC-line Trigger . . . . .	129
C.2 Schmitt-Trigger Circuit . . . . .	129
C.3 Stable Amplified Photo-diodes. . . . .	130
<b>Appendix D Development of Smart Laboratory Devices</b>	<b>134</b>
D.1 Introductory Project: FPGA Based Down Counter for Ultrafast Experiments . . . . .	135
D.1.1 Basic Idea: Code snippet . . . . .	137
D.1.2 Hardware and Implementation . . . . .	138
D.1.3 Entire Source Code . . . . .	138
D.2 Outlook . . . . .	141

# List of Figures

1.1	Spontaneous emission of matter waves. For details see chapter 7.	4
1.2	Characterization of magnetic fields. For details, see chapter 5.	5
2.1	Schematic of apparatus for BEC production . . . . .	14
2.2	Level diagram of Rubidium . . . . .	16
2.3	Optical schematic for main experiments . . . . .	17
2.4	Raw camera illuminations with and without atoms . . . . .	19
2.5	Typical absorption images . . . . .	20
2.6	Result of Kapitza-Dirac diffraction . . . . .	22
2.7	Simulation of Talbot-resonant kicking . . . . .	24
2.8	Rabi Spectra . . . . .	26
2.9	Rabi resonance . . . . .	27
2.10	Breit-Rabi diagram for $^{87}\text{Rb}$ . . . . .	28
2.11	Potential depth and scattering rate for state-selective optical potential . . . . .	29
2.12	Bloch-bands . . . . .	32
2.13	Wannier and Bloch Functions . . . . .	32
3.1	Temperature control for Rb source . . . . .	38
3.2	Diagram for calculating pressure and flow in vacuum. . . . .	39
3.3	Lifetime of Rb-atoms in vapor cell . . . . .	41
3.4	Optical schematic for improved optical pumping . . . . .	43
3.5	Level diagram for optical pumping . . . . .	44
3.6	Performance characterization of improved optical pumping . . . . .	45
3.7	Number stability after improvements . . . . .	48
4.1	Sample images for fringe-removal . . . . .	56
4.2	Comparison of masking and not masking the atomic signal . . . . .	57
4.3	Sample principal components and their Fourier transforms . . . . .	58
4.4	Mean overlap of principal components with a sample set of images . . . . .	58
5.1	In situ magnetometry scheme . . . . .	63

5.2	Measurement of AC-field fluctuations . . . . .	66
5.3	Slow Rabi cycling using field post selection . . . . .	67
5.4	Simulated field reconstruction . . . . .	69
5.5	Microwave spectroscopy of a free-to-bound transition into a state-selective optical lattice . . . . .	70
6.1	Spontaneous emission. . . . .	72
7.1	Realization of matter-wave emitters . . . . .	80
7.2	Study of matter-wave emitters in the Markovian regime . . . . .	83
7.3	Study of non-Markovian dynamics and bound state of matter-wave emitters . . . . .	86
7.4	Average free-to-bound microwave spectrum . . . . .	91
7.5	Background subtraction . . . . .	93
7.6	Raw data for energy shift . . . . .	94
7.7	Simulated decay dynamics . . . . .	95
7.8	Simulated time evolution in the Markovian regime showing finite size effects. . . . .	97
A.1	Mean Field Shifted Spectrum . . . . .	124
B.1	Interspecies Feshbach resonance . . . . .	126
B.2	Two-photon spectroscopy of a Mott-insulator . . . . .	127
C.1	Schematic of the setup for the line trigger . . . . .	130
C.2	Electronic schematic for Schmitt-trigger circuit . . . . .	131
C.3	Electronic schematic for logarithmic photo-diodes . . . . .	132
C.4	Schematic for PI-control with logarithmic photo-diodes . . . . .	133
D.1	Photo-Diode to Trigger Circuit . . . . .	135
D.2	Picture of FPGA Board . . . . .	136
D.3	Downcounter FPGA Pinout . . . . .	141

## Acknowledgements

This is dedicated to the people who have supported me in turning my dream of pursuing this advanced degree into reality. It is impossible to overstate the importance of the support and help I have received from the people around me, allowing me to evolve both personally and professionally.

I want to first thank my advisor Dominik Schneble, who is an endless source of great ideas, physical intuition, helpful, wanted, and needed criticism, and most importantly ceaseless enthusiasm for the physics in our laboratory. Witnessing his unwavering support for and belief in his students is a constant source of encouragement, pushing us on to new experiments every day. He has first introduced me to the field of atomic physics and ultracold atomic physics, which I have been in love with ever since. Motivation and advice were always welcome, and came in plentiful amounts, which made discussions with him always intriguing, fruitful and interesting. I want to thank him for imbuing me with the perseverance and skills needed for pursuing a career in physics and beyond.

In the laboratory I had the incredible pleasure to work and collaborate with a plethora of outstanding people and physicist. During my first year at Stony Brook, I enjoyed training from the renowned Bryce Gadway, who has not only taught me to understand physics and ultracold physics, but also to pass that knowledge along. Jeremy Reeves has taught me many of my laboratory skills along with doing a significant part of the work on which this dissertation is based. Without him I would not be where I am today, and I would certainly not be as good a physicist without his help and explanations throughout my first four years at Stony Brook. Michael Stewart, who joined the group shortly after me, is an incredibly talented physicist and I had the pleasure of discuss with him some of the most intriguing and difficult questions I have had during my Ph. D. His deep knowledge and understanding of mathematics (and language) provide a novel viewpoint and understanding of most topics, which was invaluable for fleshing out physical ideas for publications. Arturo Pazmiño has been a great colleague and an invaluable help during my time in the laboratory. I have always been able to count on him for helpful advice in and around the lab. Joonhyuk Kwon, the most recent addition to our group, can always be relied on to ask intriguing questions about the publications which we are writing or about daily lab-work. He is an excellent graduate student and I look forward to his continued great contributions and work in the upcoming

years. Departing from such an excellent group of people leaves me with a heavy heart, but I am more than looking forward to their future work. I will miss lunch breaks and driving to conferences with you!

The committee for my dissertation defense has accompanied and mentored me during my Ph. D. years. For their time, mentorship, effort, help, and support, I want to thank Andrew Daley, Philip Allen, and Eden Figueroa. Thank you for your guidance along the way and thank you for attending my defense. My committee has accompanied my development from a young graduate student to a graduating student with many helpful questions during the yearly updates. While Andrew Daley was not formally on my committee until the defense, I have had the pleasure of interacting with him and learning from him during his visits to Stony Brook and during DAMOP meetings, which makes him an excellent choice for the external committee member. Thank you also to professors Thomas Weinacht, Hal Metcalf and Tom Bergeman, for always answering the tricky questions I had and for offering advice and guidance along the way. Martin Cohen has also been a constant presence throughout my Ph. D. and I am thankful for his guidance in technical questions, as well as his unwavering endurance in reading and discussing the publications of our group with me. He is a steady source of good advice and an amazing listener.

I am grateful for the general support of the department chairs Laszlo Mihaly and Axel Drees, the graduate program director Jacobus Verbaarschot, as well as the detailed support of the main office staff Sara Lutterbie, Donald Sheehan, Diane Diaferia, Socoro Delquaglio, Linda Dixon, Jin Bentley and Nathan Leoce-Schappin. I have received great help from the staff in the machine shop with building various prototypes, namely Mark Jablonski, Jeffrey Slehta and Jeffrey Thomas. I am also grateful for the help I received from Eugene Shafto and Charles Pancake working with electronic circuits. Thanks also to Rich Berscak and Frank Chin for keeping the building and labs running, as well as to Andrzej Lipski and Richard Lefferts for technical help and encouraging conversations.

Outside of my group I have had the pleasure of being a part of the wonderful community that makes Stony Brook atomic physics an outstanding place to pursue studies. I want to thank Spencer Horton for showing me that a world outside ultracold physics is also interesting and for helping me with many of my projects, either directly or indirectly. Mehdi Namazi, who is an excellent physicist and friend, and who made long evenings at the university enjoyable. I want to thank Bertus Jordaan and Brian Arnold for great times in the physics basement, help with tricky projects and great road trips. Thanks to Chris C., Peter S., John E., Oumarou N., Arthur Z., Yusong L., Brian K., Chris I., Taichi I., Chuan C., Mael F., Guodong C., Samet D., Steve S., Sonali G., ,

Thomas M., Sam R., Alessia S., and everybody that I have failed to mention for making my time here unforgettable and great.

Outside of the AMO-basement, I want to thank my house-mates over the years, Lukas, Johannes, Hans, Patrick, Tristan, Cameron and Niveditha. It was always a pleasure to come home and to be greeted by great people, be able to share a meal and discuss physics and more importantly discuss the world in general. Thank you for making my stay on Long Island a pleasant one. Special thanks to Hans, Yiqian, Patrick, Adrian and Kent for accompanying me on the entirety of my journey and for hanging out on many evenings, allowing me to forget the daily challenges for a bit.

I want to thank colleagues, friends and faculty from Universität Würzburg, especially Johannes, Martin, Marvin, Verena, David, Jan and Matthäus for remaining awesome friends over the years and Prof. Assaad for leading and enabling the exchange program that got me to Stony Brook in the first place, along with all the other professors, tutors and friends at Würzburg, who have helped make me the physicist that I am today.

I want to thank the excellent technical support staff from Toptica, TDK Lambda, Mini-Circuits, Princeton Instruments and Coherent for answering my odd requests and weird questions, and really helping me understand their products or helping me fix a piece of equipment on site. A special thanks to the notorious Jason Reeves from Menlo USA, for being an amazing Stony Brook graduate and always being the gathering place at conferences ('is he in the audience?').

I want to thank the great community in and around weightlifting at Stony Brook, which I had the great pleasure of learning from and lifting with. After a stressful day at work, I always found great comfort in putting work aside and being able to enjoy the pleasures of simply picking up weights and putting them back down. Further, I would like to thank Station Pizza at Stony Brook for being the last place still open to feed hungry graduate students at 10:30 pm when running late nights.

My family has supported me throughout my Ph. D. and I am eternally thankful to them. I thank my parents Christine and Ludwig for being the best parents a child could wish for, for always supporting me and for teaching me the value of hard work, compassion, and kindness. I am eternally indebted to both of my sisters, Cordula and Judith, for they also did raise me in a way. They were stern with me when I needed it and always explained the world around me when I asked difficult or annoying questions. They raised a brother and son that is very proud of having received their training, kindness, and support.

Last but far from least, I want to thank you Naomi, for sticking with me for

all these years. When times were rough you kept with me through my antics, you helped me through my toughest times and enjoyed with me my best times, whether you were physically there or not. With you I always had someone to talk to, and this dissertation would certainly not have come together in the way it has today. You have taught me, maybe more than anyone, about the value of communication in science and in general. I am lucky to have found you and am looking forward to our future together, in the US, Germany or wherever life may take us.

We are grateful for the generous support by the National Science Foundation of the United States of America (NSF).

# Chapter 1

## Introduction

The theory of an ideal monatomic gas is one of the first topics that a beginning physics student encounters in the great (and vast) subject of statistical physics and thermodynamics [1]. Classically one can reduce the temperature of a gas arbitrarily without drastic changes to its behavior as long as interactions can be neglected. With e. g. attractive interactions present, the system of atoms should be able to change its phase from gaseous to liquid or solid. In quantum mechanics [2] and quantum statistical mechanics however, if we reduce the temperature of an ‘ideal’ noninteracting gas, its behavior changes due to the notion of ‘point-particles’ breaking down. Atoms of low enough kinetic energy gain a quantum-mechanical version of spatial extent, the (thermal) deBroglie wavelength [3]; if it exceeds the inter-particle spacing in the gas, the quantum statistics of the atoms (bosonic for integer spin and fermionic for half integer spin) dominate the behavior. The dilute-gas approximation breaks down in the sense that the occupation function for each energy is no longer classical but has to be replaced by the proper quantum analogue, either the Bose-Einstein distribution for bosonic atoms (such as alkali atoms with an uneven number of nucleons) or the Fermi-Dirac distribution for fermionic atoms (such as alkali atoms with an even number of nucleons).

In AMO physics (atomic, molecular and optical physics), the realizations of quantum gases are ultracold and dilute: Bose-Einstein condensates (BEC, for bosonic constituent particles) [4–6] or degenerate Fermi-Dirac-gases (DFG, for fermionic constituent particles) [7–9] respectively. Outside of AMO physics, aspects of BEC physics can be found in superfluid helium [10, 11] and conventional superconductors [12] and DFGs can be found in white dwarf stars and (at least to some degree) neutron stars [13], to name just a few examples.

The first realizations of quantum degenerate atomic gases, in 1995, were BECs of rubidium [14], lithium [15, 16] and sodium [17] atoms, a few years

later followed by a DFG of potassium atoms [18]. Ever since these initial realizations, the field has seen explosive growth and sustained interest. Early work in BECs studied the coherence of these gases [19] (leading to the first atom laser [20–22]), collective excitations and properties of sound [23, 24], the formation of vortices when imparting angular momentum [25], superfluidity and critical velocity [26, 27], superradiance [28, 29] and matter wave amplification (four-wave mixing) [30, 31], the emergence of solitons in BECs [32, 33], the utilization of Feshbach resonances to tune their interactions [34, 35], Bragg diffraction and spectroscopy [36], and their controlled collapse and explosion (Bosenova) [37, 38], among many other studies.

Over the past two decades, many other species have been brought to quantum degeneracy, including hydrogen [39], potassium [18, 40], metastable helium [41], cesium [42], ytterbium [43], chromium [44], calcium [45], strontium [46, 47], erbium [48], and dysprosium [49], which has enabled a plethora of other studies. The realization of bosonic molecules from two constituent fermions [50, 51] and the study of the BEC-BCS crossover for cold fermion [9] more recently culminated in the realization of ultracold polar molecules [52–54] and independently ultracold highly polar atoms [44, 48, 49, 55, 56] which both allow the implementation of long-range interactions in these ultracold gases.

With the realization of BECs in optical lattices [57, 58] it soon became obvious that ultracold atoms promise an outstanding degree of control over microscopic Hamiltonians and quantum states, allowing the study of engineered many-body systems [59, 60]. Among the more recent experimental advances of the field are the realization of single site resolved detection of bosons [61–63] and fermions [64–68] in two-dimensional lattice geometries, the study of disordered quantum gases [69], the emulation of model systems, such as artificial graphene [70] and the Haldane- [71] and Hofstadter models [72, 73], spin-orbit coupled systems [74–76], and very recently the realization of the Fermi-Hubbard model (FHM) and its emergent anti-ferromagnetic phase [77–81], and studies of conduction of fermions through 2D [82] and 1D channels [83]. In a broader sense, cold atoms in optical lattices can be used to experimentally access hard-to-compute quantum many-body models via direct quantum simulation [60, 84–86] and to realize models that have no analogue or realization anywhere else [71, 87].

In our laboratory we have a long history [88–91] of work with state-selective optical lattices, including the study of four-wave mixing of matter-waves [92], of superfluidity of bosonic mixtures [93], of (disordered) Bose-glass behavior [94], and of probing ultracold crystals using matter waves [95], as well as studies of non-adiabatic external-internal-state dynamics [96].

In this dissertation, we now use these state-selective optical lattices to

realize and study an open quantum system [97–99], whose Hamiltonian is that of the celebrated Weisskopf-Wigner model [100] describing how a two-level atom in its excited state can decay to its ground state by emitting a photon. However, we will see that in our system, what is emitted are not single photons but single atoms.

In the conventional Weisskopf-Wigner model, the necessary transition matrix element for the decay of an excited atom is provided by the coupling of the atomic dipole moment to the fluctuating quantum electrodynamic vacuum field. The detailed structure of the vacuum plays a major role in how this decay proceeds. It was originally realized by Purcell [101] that structuring of the environment (e. g. structuring of the refractive index, embedding emitters into ordered/disordered materials) modifies the vacuum. Some of the most prominent examples of modifying the QED-vacuum [102] are photonic crystals [103–105] and cavities [106], which can have a pronounced effect on the spontaneous emission of an atom. Taken to its extreme, modifying the vacuum can fully prohibit spontaneous emission altogether or even makes it a reversible process in the form of Rabi oscillations [106].

Since the first prediction of photonic bandgap (PBG) materials (also called photonic crystals) [103–105] and the first experimental realization of a three dimensional PBG in the microwave [107] and optical domains [108], these photonic crystals have been used extensively to manipulate and control spontaneous emission. This was first done in a one dimensional PBG material [109] (distributed Bragg reflector), and later using dies in colloidal opals [110] and ions in inverse opals [111], and has culminated in the incorporation of a quantum well [112] and quantum dots [113] into three dimensional photonic crystals.

Researchers were since able to isolate and image single emitters (quantum dots) incorporated into photonic crystals [114], map the local density of states using engineered emitters [115], find spectral evidence for non-Markovian decay [116] and modify the Lamb shift [117], to name only a few of the many advancements in this field. In more recent years, there has been a surge of interest in corrugated one-dimensional waveguides (i. e. photonic crystals in one dimension rather than one-dimensional photonic crystals) as promising candidates for future photonic devices in quantum information, starting with the first creation of corrugated waveguides [118] and the trapping (and thereby coupling) of atoms close to its surface [119]. This has led to the detection of superradiance in these devices [120] as well as coherent atom-atom interaction mediated by these corrugated waveguides [121]. Corrugated microwave guides using transmon-qubits as artificial microwave atoms were recently used to indirectly detect a photon bound state [122], and interactions of two artificial atoms in contact with a corrugated waveguide [123].

The focus of this dissertation is the realization of a close relative to such photonic systems (which in itself is of major recent theoretical interest [124–127]), in the form of a regularly spaced array of matter-wave emitters, coupled to a one-dimensional matter-wave guide. The dispersion of our massive particles (as opposed to massless photons) mimics the approximately quadratic dispersion relation of photons near a photonic bandgap.

As a result of the high tunability and flexibility of our system, we are able to observe directly, **for the first time in this type of system**, non-Markovian dynamics in real time (rather than using spectroscopy [116]) and are able to directly observe an exotic bound state, comprising evanescent waves, which, for photonic systems, has been predicted more than 40 years ago [103, 128].

Our experiments are technically (but not scientifically) based on previous work in our laboratory on non-adiabatic diffraction of matter waves [96] where we resonantly coupled a free BEC to a lattice-trapped state and observe diffraction beyond the usual approximation of an adiabatic potential. Now, the initial state is not a free BEC but a sparse array of localized atoms that get released into free space. The much lower coupling strengths used in the present experiment require a much finer control over the resonance condition than before and the preparation of the samples require detection of small atom numbers:

(1) Since a key prerequisite for the study of spontaneous emission in our matter-wave system is the precise knowledge and control of internal level spacings, namely the different hyperfine Zeeman level-spacings of the alkali atom under consideration, we need to better account for the main uncertainty, the magnitude of the magnetic field applied to the atoms. We develop a method [129] that enables the precise knowledge of the magnetic field at the time a measurement is taken, by employing a procedure which divides the set of all available hyperfine states into a subset that is used for the experiment and a subset which is used for determining the magnitude of the applied magnetic field. Through the use of a sequence of multiple RF-pulses, the magnetic field at the time of measurement can be reconstructed.

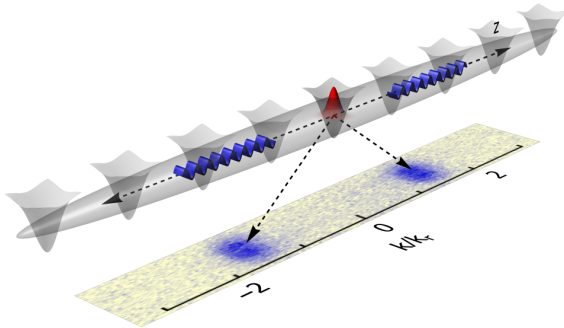


Figure 1.1: Spontaneous emission of matter waves. For details see chapter 7.

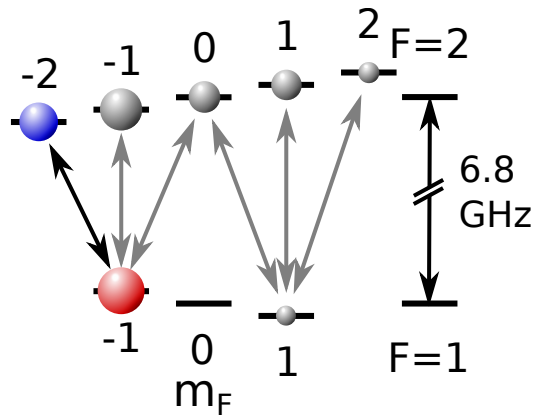


Figure 1.2: Characterization of magnetic fields. For details, see chapter 5.

(2) The small atom numbers required for sparse samples of matter-wave emitters rely on absorption images which are free of any artifacts, such as imaging fringes, in order to guarantee high fidelity detection. We describe a method to remove artifacts from pictures using empty images obtained during data-taking, based on principal component analysis in order to filter out only significant contributions from the empty images.

### Outline of the Dissertation

In chapter 2 we will give a brief overview of the fundamental experimental techniques, such as laser cooling, trapping of cold atoms using magnetic fields or light, and state-selective trapping potentials. In chapter 3 we will describe various experimental improvements and upgrades that we were able to contribute to the laboratory, which helped to achieve a more stable operation and increase the rate of data taking. Chapter 4 describes image analysis done to remove fringe artifacts from our images. The procedure used for (post-selection-) stabilization of magnetic fields is introduced in chapter 5. Chapter 6 gives a more technical introduction into the physics of spontaneous emission and spontaneous emission in matter-wave systems. Our experiments on matter-wave emission into matter-waveguides are described in chapter 7. We finally give an outlook into future experiments and directions in chapter 8.

**Publications of this PhD work described either in part or in full:**

- Chapter 5  
*In-situ magnetometry for experiments with atomic quantum gases*  
L. Krinner, M. Stewart, A. Pazmiño, and D. Schneble  
Review of Scientific Instruments **89**, 013108 (2018)
- Chapter 7  
*Spontaneous emission of matter waves from a tunable open quantum system*  
L. Krinner, M. Stewart, A. Pazmiño, J. Kwon, and D. Schneble  
Nature **559**, 589 (2018)

**Publications co-authored during the PhD work (covered in other theses):**

- *Analysis of non-Markovian coupling of a lattice-trapped atom to free space*  
M. Stewart, L. Krinner, A. Pazmiño, and D. Schneble  
Physical Review A **95**, 013626 (2017)
- *Nonadiabatic diffraction of matter waves*  
J. Reeves, L. Krinner, M. Stewart, A. Pazmiño, and D. Schneble  
Physical Review A **92**, 023628 (2015)
- *Evidence for a Quantum-to-Classical Transition in a Pair of Coupled Quantum Rotors*  
B. Gadway, J. Reeves, L. Krinner, and D. Schneble  
Physical Review Letters **110**, 190401 (2013)

# Chapter 2

## Theoretical and Experimental Basics

The techniques for creating and characterizing Bose-Einstein condensates have been well-established for two decades [130]; however the details are often dependent on the specific application. In the first section, we will briefly discuss the experimental apparatus and the scheme for creating a BEC in our laboratory and will then outline experimental techniques that are used in the remainder of the dissertation. A more detailed description can be found in [88, 89, 131–133] and in the original publication describing our apparatus [134].

### 2.1 BEC in the Schneble Laboratory

In this section we will outline the tools needed for achieving a Bose-Einstein condensates, and give a brief description of our specific apparatus.

A quantum degenerate gas has a temperature so low that the thermal deBroglie wavelength  $\lambda_{dB}$  of the constituent particles becomes comparable to the inter-particle spacing. The figure of merit we will seek to increase is the phase space density [135]:

$$PSD = n \times \lambda_{dB}^3 = n \left( \frac{2\pi\hbar^2}{mk_B T} \right)^{3/2},$$

with the density  $n$ , temperature  $T$ , mass of the atom  $m$ , the reduced Planck's constant  $\hbar$ , and the Boltzmann constant  $k_B$ . The phase transition to a BEC occurs when  $PSD \geq \zeta(3/2) \approx 2.61$  [6].

In general, the position space distribution function of  $N$  classical, trapped, non-interacting particles is given by a Boltzmann factor divided by a normalization factor (which equals the partition function of a trapped particle divided by the free particle partition function) ( $\beta = 1/k_B T$ ) [1]:

$$\begin{aligned} n(\vec{r}) &= N \times \exp(-V(\vec{r})\beta) \left( \int_{-\infty}^{\infty} d^3\vec{r} \exp(-V(\vec{r})\beta) \right)^{-1} \\ &= \frac{N}{Z'_1} \exp(-V(\vec{r})\beta), \end{aligned}$$

where  $V(\vec{r})$  is the trapping potential (see later in this chapter). It confines the atoms to a finite region of space and can be created using e. g. magnetic fields or light. The potential will usually be a harmonic oscillator potential, in which case the maximum density is given by  $N/Z'_1$ . Alternatively, the average density can also be approximated by the expectation value of the radial extent of the individual atoms [132] ( $\vec{r} = (x, y, z)$ ):

$$\langle r \rangle = \frac{N}{Z'_1} \int d^3\vec{r} \exp[-\beta V(\vec{r}) \sqrt{x^2 + y^2 + z^2}].$$

For particles in a three-dimensional harmonic potential the maximum density evaluates to

$$n_{HO} = \frac{N\omega_x\omega_y\omega_z(m\beta)^{3/2}}{\sqrt{8\pi^{3/2}}}.$$

For a linear potential of the form  $V(\vec{r}) = V_0\sqrt{ax^2 + by^2 + cz^2}$ , the maximum density is

$$n_{lin} = \frac{NV_0^3\beta^3\sqrt{abc}}{64\pi}.$$

### 2.1.1 Laser Cooling and Magneto Optical Trapping

The journey towards quantum degeneracy usually starts with a room temperature alkali vapor in an ultra-high vacuum chamber which is subsequently cooled most of the way to quantum degeneracy by using laser cooling [136, 137] in a magneto-optical trap (MOT) [138, 139] with subsequent molasses-cooling [140–142]. Laser cooling and trapping techniques [143] exploit the mechanical effects of light on neutral atoms at frequencies close to resonance and can yield atomic samples with typical temperatures in the range of tens of micro-Kelvins. Details about our magneto-optical trap can be found in [131].

For a brief description of the principle, let us first consider a two-level atom with two possible internal states  $|e\rangle$  and  $|g\rangle$  with a transition of energy  $E_{e,g} =$

$\hbar\omega_{e,g}$  and linewidth  $\Gamma$ . For simplicity, we will assume that the particle can only move in one dimension. Consider two counter-propagating laser beams, propagating in the (against the) direction of motion of the atom. The atom can absorb light (photons) from each laser beam. Upon absorption of a resonant photon, from one of the laser beams with frequency  $\omega_L = \omega_{e,g}$ , the atom recoils with the photon momentum  $\hbar k_r = \hbar 2\pi/\lambda = \hbar\omega_{e,g}/c$  (with  $c$  the speed of light) in the same direction of the propagation direction of the laser beam, i. e. it changes its momentum by that amount. Changing the frequency of the light away from transition frequency  $\omega_L = \omega_{e,g} + \delta$  (detuning  $\delta$ ) then implies that absorption events happen less frequently. We will assume that  $\delta < 0$ , i. e. that the laser beams are red-detuned. If an atom happens to be traveling towards one of the beams, it perceives a blue shift, towards resonance, of the frequency of that beam (due to the Doppler-effect), and a red shift of the frequency of the other beam. Hence the atom will scatter more strongly (more often) from the beam that it moves towards, and less photons from the beam it moves away from. Hence it will receive, on average, more recoil kicks in the direction opposite to its motion.

The absorption is followed by isotropic reemission, which means that on average (averaging over hundreds or thousands of scattering events), the reemission does not change the momentum of the atom. Furthermore, the emitted photons are blue-shifted with respect to the absorbed ones (in the laboratory frame). This means that the energy of the emitted radiation is higher than the energy of the absorbed radiation, where the difference is provided by the kinetic energy of the atom: kinetic energy is removed from the system by transferring it into the radiation field. If we consider motion in either direction and take into account both laser beams, one can show [143] that an effective linear friction force ( $\vec{F} \propto -\vec{v}$ ) arises for atoms which are slow enough. Note that this effect is reversed (anti-friction) for blue detuning  $\delta > 0$ , the emitted radiation being red-shifted with respect to the absorbed radiation in this case. The friction is generalized to three dimensions by employing three mutually orthogonal pairs of laser beams.

One can also spatially vary the transition frequency  $\omega_{e,g}$ , for example by using a quadrupole magnetic field (see also section 2.1.2 and Eq. 2.1) when there are magnetic sublevels of the excited state  $|e\rangle$  present. The quadrupole field varies the level spacing of excited and ground state due to differential Zeeman shifts (see section 2.2.4), and in a similar fashion as above, this spatial variation of the resonance frequency together with counter-propagating laser beams can create an effective restoring force  $\vec{F} \propto -\vec{x}$  towards the origin of the quadrupole magnetic field (again averaging over many absorption/reemission

cycles).

With three mutually orthogonal beam pairs, these ingredients thus create the magneto-optical trap (MOT). The friction and restoring forces are present everywhere within the capture range in real- and momentum-space, depending on the laser intensity, detuning, profile, and magnetic field gradient. In our density-limited (high atom number) MOT, the temperature is around 1 mK (significantly higher than the Doppler-temperature  $T_D = \hbar\Gamma/2k_B = 146 \mu\text{K}$  [144] due to re-scattering of photons), with the number of atoms close to  $10^{10}$  atoms [131], and densities in the  $10^{11}\text{cm}^{-3}$  range (the diameter of the atomic cloud loaded into our MOT is several mm).

When the magnetic field is switched to zero in a MOT, a configuration called optical molasses is achieved. The temperature one can reach when not requiring a restoring force is considerably lower; sub-Doppler cooling mechanisms [141, 142] that arise from optical pumping between the AC-Stark-shifted Zeeman sublevels of  $|g\rangle$  in the polarization structure of the light field, finally give temperatures on the order of several  $10 \mu\text{K}$  [131] in the last stage of our laser-cooling sequence.

### 2.1.2 Magnetic Trapping

We eventually need a way to spatially constrain our atoms in the absence of photon-scattering events in order to attain the low temperatures ( $\sim 100 \text{ nK}$ ) and high densities ( $\sim 10^{14}\text{cm}^{-3}$ ) necessary for our experiments. In the following, we will give a brief summary of the magnetic trapping techniques used in our apparatus. A detailed description of their implementation can be found in [132].

We first transfer the atoms from the MOT/molasses into a quadrupole magnetic trap [145]. A quadrupole magnetic field has the form

$$\vec{B}_Q = \frac{b}{2} \times \begin{pmatrix} -x \\ -y \\ 2z \end{pmatrix}, \quad (2.1)$$

where  $b$  is the gradient along the axial direction. The Hamiltonian for a stationary atom in a magnetic field is  $\hat{H} = -\vec{\mu} \cdot \vec{B} = \mu_B g_F m_F B$ , where  $g_F$  is the hyperfine Landé  $g$  factor (we assume the atom is in the ground state),  $F$  is the total magnetic quantum number,  $m_F$  is the projection of the total angular momentum  $\vec{F}$  along the quantization axis  $\vec{B}$ , and  $\mu_B$  is the Bohr magneton. If we assume that the internal state of the atom is fixed (i. e. the quantization axis can follow the direction of the local magnetic field direction adiabatically), the

Hamiltonian for an atom moving adiabatically in a spatially varying magnetic field is

$$\hat{H} = \frac{\hat{p}^2}{2m} + \mu \left| \vec{B}(\vec{r}) \right|, \quad (2.2)$$

where  $\vec{B}(\vec{r}) = \vec{B}_Q$  and  $\mu = m_F g_F \mu_B$  [132]. Hence, if  $m_F$  and  $g_F$  have identical signs, we have created a trap for an atom in such a hyperfine state (quadrupole magnetic trap). These types of atoms are called low-field seekers. For the  $5^2S_{1/2}$  ground state of  $^{87}\text{Rb}$ , low-field seekers are  $|F = 1, m_F = -1\rangle$ ,  $|2, 1\rangle$  and  $|2, 2\rangle$ .

A major drawback for quadrupole magnetic trap is that it can only hold atoms down to a certain minimum temperature. The assumption made initially that the atoms stay in the same hyperfine state (including  $m_F$ ), becomes easily violated for atoms moving close to the trap center due to nonadiabaticity. At the trap origin, the field vanishes and there is no direction for the quantization axis. A particle that passes near the trap center would experience a (near) sudden change in quantization direction (exceeding the Larmor-frequency), likely causing it to flip the sign of  $m_F$ , its total angular momentum z-projection, which in turn transforms a trapped into an anti-trapped particle (Majorana loss). These losses scale as  $\Gamma_M \propto (b/T)^2$  [146], and prohibit lowering the temperature below 100  $\mu\text{K}$  (for typical trap parameters). There are several strategies to circumvent this problem, for example Ioffe-Pritchard traps [147, 148] with a non-zero field minimum, plugging the hole with a repulsive laser beam [17, 149, 150] as well as time orbiting the field zero faster than the atoms can follow (TOP-trap) [146]. This latter strategy is the approach taken by our group.

A time-orbiting-potential trap (TOP-trap) is created by starting with a quadrupole field as described above, and adding a rotating bias field of the form

$$\vec{B}_{\text{rot}} = B_0 \times \begin{pmatrix} \sin(\omega t) \\ \cos(\omega t) \\ 0 \end{pmatrix}.$$

The time-averaged trapping-potential created in a TOP is then [132, 146]

$$V(\rho, z)_{\text{TOP}} \approx \mu B_0 + \frac{m\omega_{\text{TOP}}^2 \rho^2}{16} + \frac{m\omega_{\text{TOP}}^2 z^2}{2}$$

where  $\mu = \mu_B m_F g_F$  and  $\omega_{\text{TOP}} = \sqrt{\mu \times b^2 / m B_0}$ . The field zero moves rapidly around the center of the trap, and its trajectory is typically called ‘circle of death’ due to atoms undergoing Majorana loss there. The radius of the circle of death is  $r_{\text{CoD}} = 2B_0/b$ . Majorana losses can hence be suppressed if  $\omega \gg \omega_{\text{TOP}}$  and  $k_B T \ll \mu B_0$ .

### 2.1.3 Optical Trapping

An important requirement for the experiments discussed in this dissertation is that we need to trap atoms independent of their internal state at very low temperatures and at a constant magnetic field. In order to achieve this, we employ another means of trapping the atoms, namely the optical dipole force created by far-off resonant beams of light. A trap formed using this effect is usually called FORT (far-off resonant trap) or ODT (optical dipole trap) [151].

An atom interacting with a static electric field will have an induced electric dipole moment (polarization) proportional to the field strength.

$$\vec{d} = \alpha \vec{E},$$

with  $\alpha$  the complex polarizability and hence its energy will be [151]

$$U = -\frac{1}{2} \text{Re}(\vec{d}) \cdot \vec{E} = -\frac{1}{2} \text{Re}(\alpha) |\vec{E}|^2.$$

This result still holds for oscillating electric fields, at least as long as resonant effects can be neglected. Resonant effects include the absorption of light if the frequency of light is close to the transition frequency between two energy levels of the atom, at which point dissipative forces, as described for the case of the MOT and the molasses become significant.

Below the atomic resonance, one can reasonably assume that the polarization follows the applied electric field instantaneously (red detuning  $\delta < 0$ , lowers energy,  $\text{Re}(\alpha) > 0$ ) while above resonance the polarization has a  $\pi$  phase angle with respect to the incoming electric field (blue detuning  $\delta > 0$ , increases energy,  $\text{Re}(\alpha) < 0$ ). We can write

$$U(t) = -\frac{1}{2} \text{Re}(\alpha) |E_0|^2 \sin^2(\omega_L t),$$

with  $\omega_L$  the frequency of the light. Taking the time-average yields

$$U_{\text{dipole}} = -\frac{1}{4} \text{Re}(\alpha) |E_0|^2 = -\text{Re}(\alpha) \frac{I}{\epsilon_0 c},$$

so that we get a potential landscape that is proportional to the intensity of the light at that point in space. This is the most basic form for describing the optical dipole force of light on atoms. While it usually remains true that the dipole potential will be directly proportional to the intensity of the light, the polarizability will generally depend on frequency and the internal state of an atom, as well as the polarization of the light used, which will be discussed

in more detail in section 2.2.5. While we assumed that we are far away from resonance, the equation above also holds closer to resonance ( $U \propto 1/\delta$ ), with the added caveat that spontaneous scattering processes occur more frequently ( $\propto 1/\delta^2$ ), thus heating the atoms more quickly.

A configuration of two Gaussian red-detuned laser beams crossing at a right angle yields an optical potential of the form

$$U(\vec{r}) \approx U_y \times \exp\left[-\frac{2x^2}{w_x^2} - \frac{2z^2}{w_z^2}\right] + U_x \times \exp\left[-\frac{2y^2}{w_y^2} - \frac{2z^2}{w_z^2}\right],$$

with  $w_x$  and  $w_y$  and  $w_z$  being the beam radii in the  $x$  and  $y$  and  $z$  directions respectively, thus creating an approximately harmonic trap around the minimum. Notice that the (usually very weak) change in potential of each beam along the propagation direction was neglected in the above expression, which breaks down in the case of very tightly focused beams ( $w \sim \lambda$ ) which quickly diverge.

### 2.1.4 Evaporative Cooling

Unlike magneto-optical traps, magnetic and optical traps with their conservative potential can by themselves not provide an increase of the phase-space density. In our magneto-optical trap, we achieve a PSD of  $\sim 5 \times 10^{-7}$  [132]. To achieve the necessary increase by six to seven orders of magnitude, we employ the technique of evaporative cooling [130, 152]. For evaporative cooling one first removes the hottest fraction of atoms from the trap, and then allows subsequent rethermalization and repeats this process many times. If one removes a low enough percentage of the atoms in the trap, the PSD increases. Therefore, at least in principle, slower evaporation is better, where the limit is set by inelastic collisions and collisions with the background gas.

Evaporation in the quadrupole/TOP trap is achieved using a ‘RF-knife’. An ‘RF-knife’ uses oscillating magnetic fields (1 MHz to 100 MHz) to resonantly change the internal state of an atom from a trappable (low field seeking) to an untrappable (high field seeking) state, similar to the circle of death in the TOP-trap but at finite field magnitude (for a more detailed description see also the later section 2.2.4). The transition frequency in this case depends on the magnitude of the magnetic field and is the difference of energies  $E_B = m_F g_F \mu_B B_z = m_F g_F \mu_B |B|$ :

$$\omega_{RF} = |B(\vec{r})| \mu_B |g_F(m_F - m'_F)| / \hbar.$$

The field grows away from the trap minimum, and hence one can choose an oscillating field only resonant with magnetic fields corresponding to the highest potential energies of the atoms. This establishes evaporation by expelling only the most energetic atoms, with a new effective trap depth set by the expulsion energy. One can slowly reduce the frequency of the radiation to gradually lower the effective depth of the trap, thus lowering the temperature (and number) of the atoms in the trap, with a dramatic increase in the density and the PSD.

Optical traps naturally have a much lower total depth than magnetic traps (of order  $1 - 10\mu\text{K}$ ), such that one can simply lower the laser power of the individual trapping beams, and thus gradually lower the trap depth and again evaporate off the hottest atoms [153]. A drawback of this procedure is that it also lowers the confinement and rethermalization rate, but for the crossed-beam configuration this effect does not compromise feasibility of achieving BEC [154].

### 2.1.5 Achieving BEC

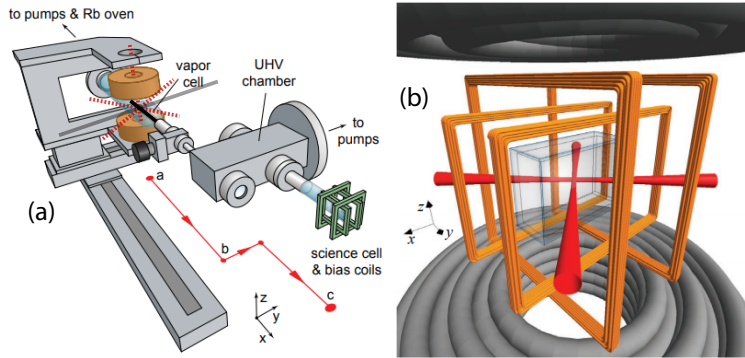


Figure 2.1: (a) Schematic of the apparatus, with the full-glass vapor cell (at high pressure  $p \sim 10^{-9}\text{mbar}$ ), the transporter coils and science cell at ultra high vacuum (UHV,  $p \sim 10^{-12}\text{mbar}$ ). MOT-beams (solid dashed, red), repump beam (translucent) and pumping beam (solid black, see section 3.3) added to the MOT region. All MOT beams are retro-reflected. (b) Close-up of the science cell (translucent) with the TOP coils (orange) and the ODT beams (red) in between the large coils used for MOT and magnetic trapping (gray). Both graphics (a) and (b) reproduced from [134] with kind permission from D. Pertot and with reproduction permission kindly granted by IOP Publishing. © IOP Publishing. All rights reserved. The red and black beams in (a) (at the position of the MOT) were added by the author.

We finally have all the ingredients necessary for creating an ultracold gas. We will now outline a typical sample preparation for the specific case of our experiment.

We use the atomic species Rubidium-87 ( $^{87}\text{Rb}$ ) which has the ground state  $5^2S_{1/2}$  with possible hyperfine states  $|F = \{1, 2\}, m_F\rangle$ , and a first excited state  $5^2P_{1/2}$  ( $F = \{1, 2\}$ , D<sub>1</sub>-transition) and a second excited state  $5^2P_{3/2}$  ( $F = \{0, 1, 2, 3\}$ , D<sub>2</sub>-transition), where our experiment uses D<sub>2</sub>-light exclusively. The resonant wavelength and natural linewidth of the D<sub>2</sub>-transition are  $\lambda_0 = 780.2$  nm and  $\Gamma = 2\pi \times 6.065$  MHz respectively [144] (see also Fig. 2.2).

Figure 2.1 shows a schematic of our apparatus [89,134]. Rubidium is loaded from a low background vapor pressure ( $p_{s7\text{Rb}} \sim 10^{-9}$  mbar,  $p_0 < 10^{-10}$  mbar) into a MOT, consisting of three pairs of counter-propagating beams, red detuned from the D<sub>2</sub>,  $F = 2 \rightarrow F' = 3$ -transition (cycling light) by  $3.5 \times \Gamma = 18.7$  MHz. An additional laser beam resonant with the D<sub>2</sub>,  $F = 1 \rightarrow F' = 2$  transition (repump light) illuminates the atoms from one direction to avoid buildup in the inactive  $F = 1$  states, which are accessible in the rare event of absorbing cycling light and transitioning to  $F' = 2$  instead of  $F' = 3$ . The vanishingly low probability of this occurrence on an event by event basis is dwarfed by the large number of cycling light absorption events, causing all the atoms to be optically pumped into  $F = 1$  on a timescale of  $< 1$  ms (the scattering rate into the off-resonant  $F' = 2$  state is still on the order of  $10^4 - 10^5$  per second).

After loading approximately  $10^{10}$  atoms into the magneto-optical trap of size  $\sim 0.5$  cm at approximately 1 mK ( $PSD \approx 10^{-7} \dots 10^{-8}$ ), we turn off the magnetic gradient field and hold the cloud for a short while at zero magnetic field gradient (and zero field) while detuning the cycling light progressively more, utilizing sub-Doppler cooling to lower the temperature of the atoms to  $< 50$   $\mu\text{K}$  ( $PSD \approx 10^{-5} \dots 10^{-6}$ ). We subsequently optically pump the atoms into the  $F = 1$  state by turning off the repump-light and additionally illuminating the light with ‘depump’ light (D<sub>2</sub>,  $F = 2 \rightarrow F' = 2$ ). We then turn on the quadrupole magnetic trap ( $b = 350$  G/cm, gradient in the axial direction) to trap about 1/3 of the initially loaded atoms ( $N \approx 10^9$ ,  $T \approx 0.5$  mK,  $PSD \approx 10^{-8}$ ), and transport the magnetically trapped atoms out of the vapor cell ( $p \sim 10^{-9}$  mbar, lifetime  $\tau \sim 1$  s) into a low pressure region ( $p < 10^{-11}$  mbar, lifetime  $\tau > 100$  s), where we can evaporate slowly enough to allow an increase in phase-space density, losing about 30% to 50% of the trapped atoms on the way out of the chamber (transport takes about 0.5 s to leave the chamber).

We then first evaporate in the quadrupole magnetic trap using a the aforementioned RF-knife technique. We use a frequency sweep from 80 MHz to

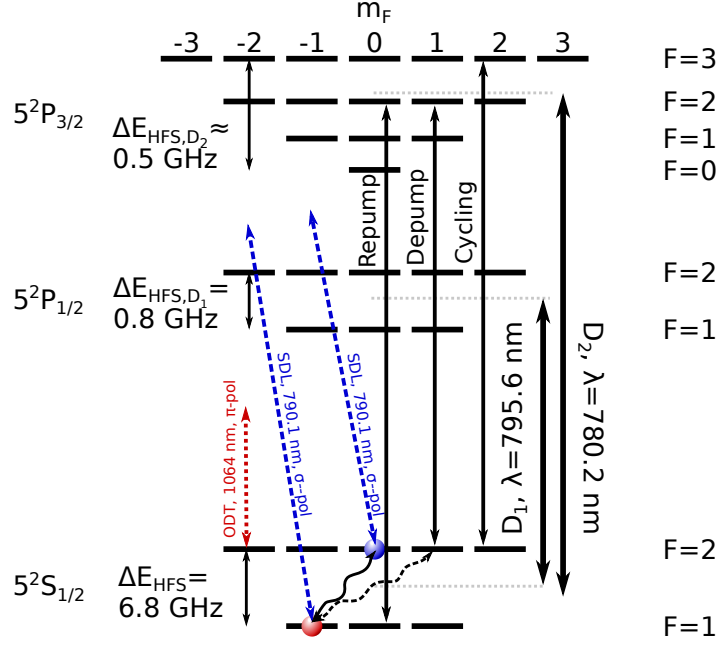


Figure 2.2: Level Scheme of Rubidium-87, with the ground state  $5^2S_{1/2}$  and the two first excited states  $5^2P_{1/2}$  and  $5^2P_{3/2}$  (split by spin-orbit coupling). The remaining degeneracies are broken first by the hyperfine-coupling (interaction with nuclear magnetic moment) and then by magnetic fields/Zee-man shifts if present. The main spectroscopic lines of Rubidium are the transitions from its ground state into either excited state, which are called the  $D_1$  and  $D_2$  lines respectively. The main transitions used in the MOT and molasses phase (not including information about the  $m_F$  levels and polarizations involved) are drawn in solid (repumper, depumper and cycling light). Far off resonant optical trapping is done red detuned from the  $D_1$ -line, several tens of THz at  $\lambda = 1064 \text{ nm}$  (short dashed line). The state-selective potential is created using  $\sigma^-$  polarization at  $790 \text{ nm}$  (long dashed lines), which yields no potential for  $|2, 0\rangle$ -atoms and an effectively blue detuned (or repulsive) potential for the  $|1, -1\rangle$ -atoms. The wavy solid arrow indicates a magnetic dipole allowed transition and the wavy dashed arrow indicates a magnetic dipole forbidden transition.

10 MHz in approximately 10 s, after which Majorana-losses stop the efficient evaporation from the quadrupole magnetic trap ( $T \approx 50 \mu\text{K}$ ,  $N \approx 10^8$ ,  $PSD \approx 10^{-4}$ ). Finally we add the aforementioned rotating magnetic field to create the TOP-trap ( $B_{\text{TOP}} = 18G$ , trapping frequencies  $\omega_r \approx 2\pi \times 25 \text{ Hz} = \omega_{\text{ax}}/\sqrt{8}$ ),

and continue evaporating (either in the TOP magnetic trap or in the ODT) to finally reach BEC at a temperature of  $T_c = \hbar\bar{\omega}N^{1/3}/k_B \sim 300$  nK, where  $N \sim 10^6$  is the remaining atom number at the transition and  $\bar{\omega} \sim 2\pi \times 60$  Hz is the geometric mean of the trapping frequencies [135].

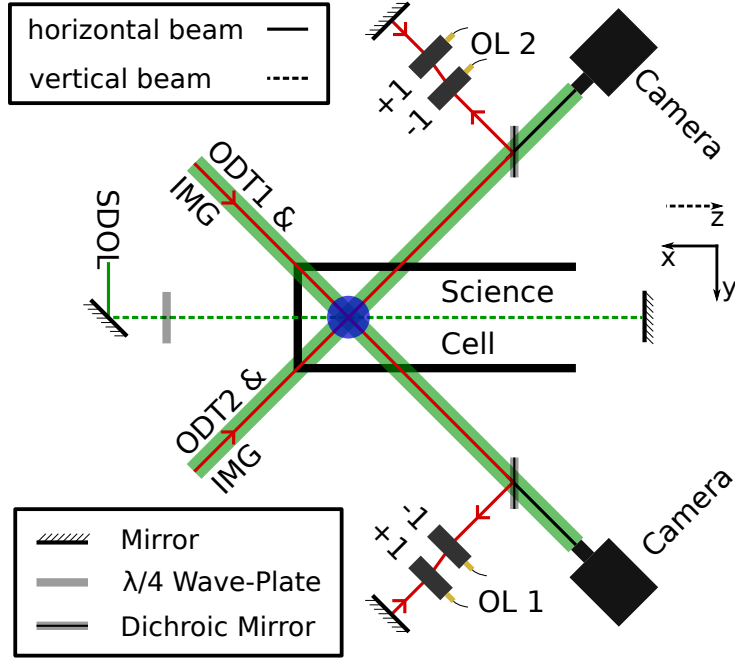


Figure 2.3: Sketch of the optical schematic. Atoms (disk) are in a crossed beam optical dipole trap and (solid lines with arrows) inside the UHV science cell (glass cuvette). Imaging (large translucent beam) is done along either ODT-direction and is separated from the ODT beams using a dichroic mirror. When atoms are in an image, they cast a shadow in the illumination onto the camera. Atoms are then recorded as absorption signals on a PIXIS CCD camera. Optical lattices along the ODT1/ODT2 directions are created by varying the amount that is retro-reflected using a pair of acousto-optical modulators [134]. Along the vertical direction (dashed green line) we use a near-resonant laser beam ( $\sim 790$  nm) and a  $\lambda/4$ -wave retarder to create state-selective optical lattices (SDOL). The lattice depth is controlled only by the forward beam since the beam is fully retro-reflected. Coordinate system is the same as in Fig. 2.1

## 2.2 Condensates in Optical Lattices

In this section we will discuss the basic techniques that we use after preparing an optically trapped ultracold atomic cloud, including optical lattices, hyperfine state manipulation and optical imaging.

### 2.2.1 Optical BEC, Detection and Optical Schematic

From a BEC (or thermal cloud) in the magnetic trap we now typically transfer into the optical trap, where we are in a convenient position to conduct the experiments discussed later in this dissertation. The optical schematic of the main apparatus is shown in Figs. 2.1 and 2.3. We trap the atoms in the intersection of two perpendicular, horizontal beams (at wavelength  $\lambda = 1064$  nm) creating a crossed optical dipole trap in which the final evaporation usually happens (beam waist  $w = 135$   $\mu\text{m}$ , beam power  $P \sim 3$  W (trapping and transfer from TOP-trap) and  $P \sim 1$  W (after forced evaporation)).

After concluding experiments, we quickly ( $\sim 1$   $\mu\text{s}$ ) turn off all trapping potentials and let the atoms fall for  $\approx 15$  ms. The cloud is usually too small to be imaged initially ( $\sim 10$   $\mu\text{m}$ ), but by dropping the atoms, we allow them to expand in time-of-flight (TOF), with the resulting atomic distribution after time of flight representing (approximately) the momentum space distribution at the time of release. We use resonant cycling light ( $\text{D}_2$ ,  $F = 2 \rightarrow F' = 3$ ) to illuminate the atoms, which then cast a shadow onto a remote-triggered 16-bit CCD camera (Princeton PIXIS 1024B). A typical detection cycle consists of illuminating the atoms (a) (see Fig. 2.4 (a)), waiting until the atoms leave the image area, then illuminating again, which creates a reference image (b) (see Fig. 2.4 (b)) and last taking a dark image without illumination (c) (not shown in Fig. 2.4).

A standard absorption image/optical density is created following the recipe (see Figs. 2.4 and 2.5) [130]

$$OD_{\text{pix}} = -\ln \left( \frac{a_{\text{pix}} - c_{\text{pix}}}{b_{\text{pix}} - c_{\text{pix}}} \right),$$

where the number of atoms in any given pixel is given by  $N = A * OD_{\text{pix}}$  where the factor  $A$  depends on pixel size, resonant scattering cross section given polarization, bias field direction (and technically hyperfine state), and  $a_{\text{pix}}$  are the individual pixels of image (a) (and similar for (b) and (c)). In our case  $A \approx 125$ .

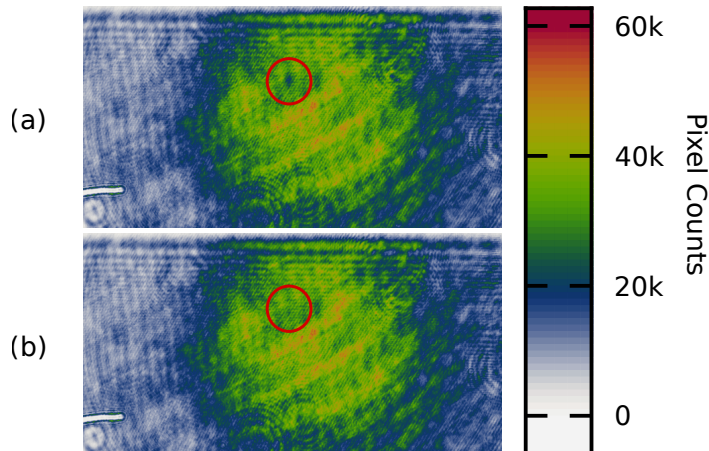


Figure 2.4: Typical raw camera images for (a) the illumination of the  $F = 2$  - atoms and (b) the reference illumination without any atoms present. Color scale gives the counts registered on each camera pixel, which is roughly comparable to the number of photons per pixel. The red circle indicates an absorption signal which signifies the presence of atoms. The dark image without illumination is not shown here.

### Stern-Gerlach separation

In order to separately image the population in the different magnetic Zeeman sublevels of  $F = 1$  and  $F = 2$  we employ a technique called Stern-Gerlach separation (as mentioned in Fig. 2.5) [130, 155]. As we have already seen in Eq. 2.2 the energy of a particle in a magnetic field depends on its internal state. If we apply a spatially dependent magnetic field (i. e. a magnetic field gradient) of the approximate form  $\vec{B}(\vec{r}) = b_0 x \vec{e}_x$  we subject the atoms to a force which is dependent on their internal state:

$$\vec{F}(m_F) = -\mu_B g_F m_F b_0 \vec{e}_x.$$

This force can be used to spatially separate different magnetic Zeeman sublevels at the beginning of time-of-flight.

In our experiment we use the same coils which also generate the quadrupole magnetic trap to Stern-Gerlach separate different magnetic sublevels. We first physically move the coils in the negative x-direction (directions are defined in Figs. 2.1 and 2.3) and slowly (over the course of 1 ms) rotate the externally applied bias-field from the z-direction into the x-direction. We then turn on the current through the coils to generate a magnetic field gradient of  $b_0 \sim$

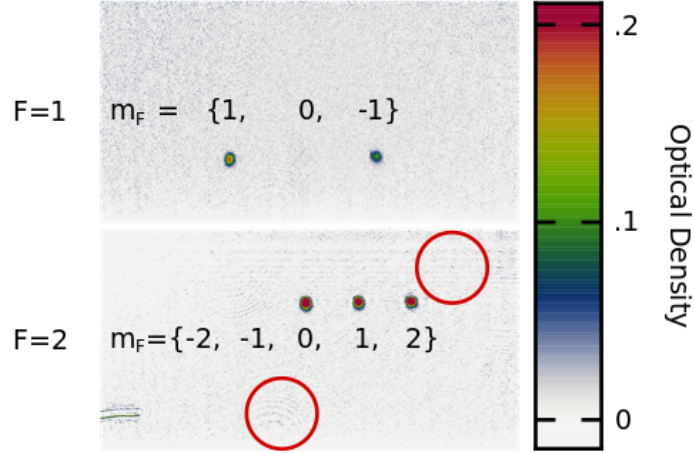


Figure 2.5: Typical absorption image generated from Fig. 2.4 by  $OD = -\ln[(a - \text{dark}) / (b - \text{dark})]$  (dark images not shown in Fig. 2.4) to generate the lower panel of this figure ( $F = 2$  atoms). The same is done for the  $F = 1$  atoms (raw image not shown in Fig. 2.4). Most of the inhomogeneities and fringes are eliminated using this method, however some residual fringing remains, which becomes important for lower atom numbers (two examples are circled). The removal of these fringes will be discussed in chapter 4. The hyperfine state is fully resolved using Stern-Gerlach separation of different magnetic moments and imaging  $F = 1$  - atoms and  $F = 2$  - atoms in different illuminations.

100 G/cm, which points approximately in the x direction (i. e. the radial direction of the coil assembly). The field gradient is applied for  $\sim 5$  ms which imparts momentum onto the atoms, which can then spatially separate during the remainder of time-of-flight ( $\sim 10$  ms). This separates magnetic species of different magnetic moments. In the case of  $^{87}\text{Rb}$  the Landé g-factor is of equal magnitude for  $F = 1$  and  $F = 2$  but of opposite sign. We can separate all states by first imaging  $F = 2$  and then imaging  $F = 1$  as described earlier in this section.

### 2.2.2 Optical Lattices and Lattice Calibration Using Talbot Kicking

In experiments with ultracold atomic gases, one of the most important tools is the optical lattice, a potential landscape created by retro-reflection of a single frequency (linewidth less than 1 MHz) laser beam, typically with a TEM-00

Gaussian spatial mode, onto itself. Around the center of a Gaussian laser beam, the electromagnetic field is well approximated by plane electromagnetic waves of amplitude  $\mathcal{E}_0$  (here the laser beam is propagating in the x-direction):

$$\begin{aligned}\vec{\mathcal{E}}(x, t) &= \text{Re} \left( \vec{\varepsilon} \mathcal{E}_0 e^{i(k_r x - \omega t)} \right) \\ \vec{\mathcal{E}}_r(x, t) &= \sqrt{R} \times \text{Re} \left( \vec{\varepsilon} \mathcal{E}_0 e^{i(-k_r x - \omega t)} \right),\end{aligned}$$

where  $k_r = 2\pi/\lambda = \omega/c$  is the wave-vector of the light,  $R$  is the reflectivity of the mirror reflecting the laser beam/plane wave,  $\omega$  the frequency of the light and  $\vec{\varepsilon}$  the polarization of the electromagnetic wave. We have seen before that the

$$I_0 = \frac{\varepsilon_0 c}{2} |\mathcal{E}_0|^2,$$

which is constant in space for a (time-averaged) plane wave.

The intensity, and thus the optical potential, of the interfering plane waves  $\vec{\mathcal{E}}(x, t)$  and  $\vec{\mathcal{E}}_r(x, t)$  (assuming that  $R < 1$ ) is then

$$U \propto I_0 \left( 1 + R + 2\sqrt{R} \cos(2k_r x) \right),$$

so that the maximum depth of the interference pattern (i. e. for  $R = 1$ ) is then  $4 \times I_0$ .

We have now created a perfectly periodic, perfectly sinusoidal potential for our ultracold atoms. The sinusoid spatial shape is especially nice, since one can easily calculate the band-structure (dispersion relation) of such a potential.

In our experiment we have three pairs of counter-propagating beams. In the two horizontal directions, we take the optical trapping beams and double-pass (i. e. ‘there and back’) them through a pair of acousto-optical modulators, enabling us to independently turn on and off (with  $R \approx 0.15$ ) the retro-reflected beam and control its intensity see Fig. 2.3 and [89, 134]. The third direction is a ‘state-selective’ optical lattice. Only the forward propagating beam is controlled and the backward propagating beam is created by full retro-reflection using a mirror. Details will be described in section 2.2.5.

The determination of the exact depth of this lattice potential is of major experimental importance. Thus far, we only know it up to a proportionality constant determined by reflectivity and polarizability of the atoms at a certain wavelength and polarization, each of which can be difficult to know precisely in a given setup (at least at the precise position of the atoms). We will now discuss a method to circumvent needing to know these parameters precisely by directly inferring the lattice depth seen by the atoms using a method called Kapitza-Dirac diffraction [57, 156, 157].

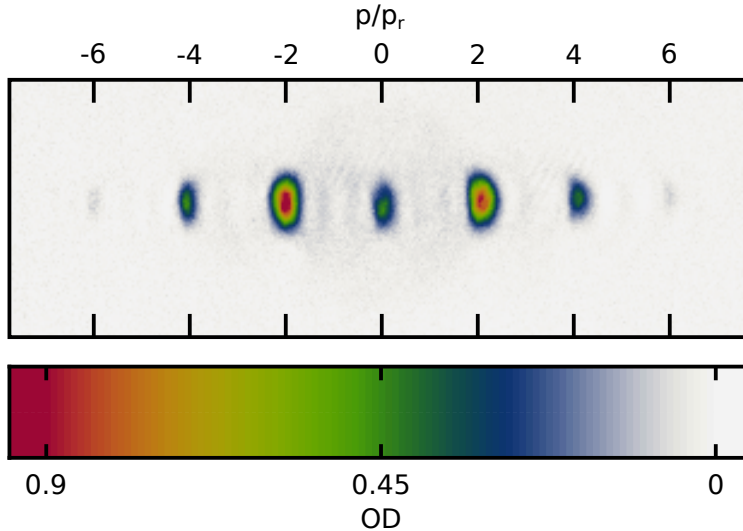


Figure 2.6: Typical absorption image resulting from a Kapitza-Dirac diffraction (KDD) pulse from a lattice of depth  $V_0 = 30(1) E_r$ . Pulse length is  $10 \mu\text{s}$  and the time of flight was  $17.4 \text{ ms}$ .

Starting with a BEC, we pulse on the lattice potential for a short time ( $\tau \sim 10 \mu\text{s}$ ,  $< 1 \mu\text{s}$  rise time) and then immediately turn off all trapping potentials, initiating time of flight, and then finally detect the momentum distribution of the atoms. The atoms diffract from the optical potential, creating a regular diffraction pattern with wave-packets centered at momenta  $n \times 2 \times \hbar k_r$  ( $k_r = 2\pi/\lambda$ ,  $n \in \mathbb{Z}$ ).

We show the result of a typical experimental run in Fig. 2.6, where we see clearly separated momentum orders at integer multiples of  $2 p_r$  ( $p_r = \hbar k_r$ ), with the lattice depth encoded in the relative populations of the individual momentum orders.

The Hamiltonian which governs this system is (neglecting interactions)  $\hat{H} = \hat{p}^2/2m + V_0 \sin^2(k_r x)$ . Since a BEC is a wavefunction which is essentially a purely zero-momentum matter wave, the dynamics significantly simplify to a discrete set of coupled equations between the amplitudes  $c_n(t)$  of the  $n$ -th momentum order ( $n = \{0, \pm 1, \pm 2, \dots\}$  corresponding to  $p/2\hbar k_r = \{0, \pm 2, \pm 4, \dots\}$ ). The resulting differential equations are [157, 158]:

$$i\dot{c}_n = \frac{4E_r n^2}{\hbar} c_n + \frac{V_0}{4\hbar} (c_{n-1} + 2c_n + c_{n+1}) ,$$

where  $E_r = \hbar^2 k_r^2 / 2m$  is the recoil energy.

In the limit of short pulses (much shorter than either the inverse recoil frequency  $E_r/\hbar = \hbar k_r^2/2m$  or the inverse of the total potential depth  $V_0$ ), there exists an analytical solution for the population of the  $n$ th diffracted peak as a function of the potential depth of the lattice as  $P_n = J_n^2(V_0 t_{\text{pulse}}/\hbar)$  [157, 158]; however this eventually breaks down once the potential becomes too shallow and longer pulse times are needed.

We can find numerical solutions of the differential equations [157] for a given finite pulse time and a range of potential depths to find the best match between simulated population and observed population extracted from absorption images.

We have now described a way to reliably calibrate intermediate and deep lattice depths ( $V_0 > 1E_r$ ) using short ( $t < 1 \mu\text{s}$ ) and intermediate length ( $t \sim 10 \mu\text{s}$ ) pulses, but the population in the non-zero orders becomes very small for small lattice depths. For a lattice depth of  $V_0 = 0.1E_r$ , the relative population in the nonzero orders is on the order of  $10^{-4}$ , which is beyond the detection limit of our apparatus. It will later be necessary to quantify lattice depths at this level.

Thus far we have only applied one lattice pulse to the atoms. We can try to amplify the population in the diffracted orders by pulsing more than once. As is discussed in [159], this situation generally results in essentially localizing in discretized momentum-space, if the time between KD-pulses is not carefully chosen. However, we can employ a technique called Talbot-resonant kicking [160, 161], where the pulses are spaced by the inverse of the two-photon recoil frequency  $t_{2k_r} = \hbar/4E_r = 68 \mu\text{s}$ . For small lattice depths, the population diffracted in the first diffracted order oscillates sinusoidally with a small amplitude when applying a single pulse of variable length. Using pulses shorter than the oscillation frequency ( $t_{2k_r}$ ) results in, (initially quadratical) growth in the diffracted population (see Fig. 2.7). The population grows beyond the amplitude of the oscillations, allowing for a much more accurate determination of small lattice depth.

We again can directly simulate the equations governing the time evolution

$$i\dot{c}_n = \frac{4E_r n^2}{\hbar} c_n + \sum_j \text{Box}\left(\frac{t-t_j}{t_w}\right) \frac{V_0}{4\hbar} (c_{n-1} + 2c_n + c_{n+1}),$$

now with the Box-functions of width  $t_w = 10 \mu\text{s}$  and spaced by  $t_j - t_{j+1} = 68 \mu\text{s}$  turning the lattice potential on and off.

In Fig. 2.7 we show a numerical computation of this for two different small lattice depths. We see that using a long pulse does not indefinitely increase the diffracted population, but rather results in the aforementioned oscillations

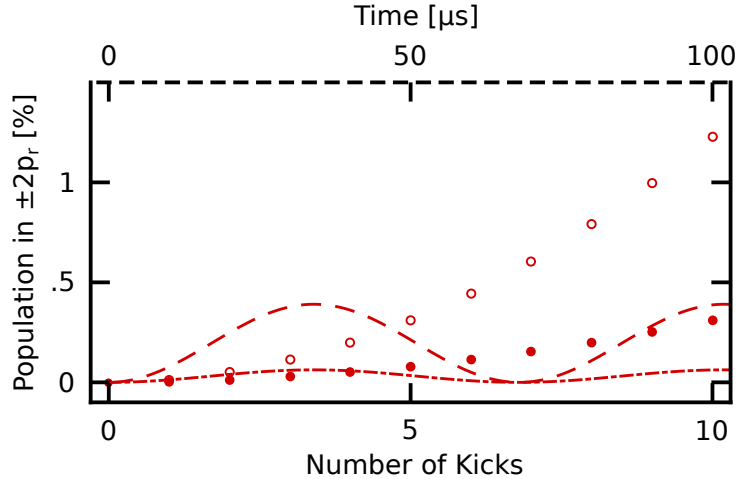


Figure 2.7: Simulated relative population of the first diffracted order for Talbot resonant lattice pulses on  $^{87}\text{Rb}$  for  $V_0 = 0.1 E_r$  (disks) and  $V_0 = 0.2 E_r$  (circles) for a pulse time of  $\tau = 10 \mu\text{s}$  and a pulse spacing of  $T = 68 \mu\text{s}$ . The dashed (dashed-dotted) line, labeled by the upper axis, is the population in the diffracted orders when a single pulse of varying length is used at potential depth of  $0.1 E_r$  ( $0.2 E_r$ ). The dashed line only is magnified five-fold for visibility. Oscillations continue at the level indicated in the figure.

of the population. In contrast the resonantly pulsed lattice diffraction grows quadratically, greatly amplifying the diffracted orders for more accurate gauging of lattice suppression for state-selective lattices.

This effect is limited by the eventual real-space separation of momentum space-orders after about 10 kicks for the  $\pm 2p_r$  and  $0p_r$  orders. Using this method we can reliably set an upper bound of lattice depth of  $V_0 = 0.2 E_r$ .

### 2.2.3 Hyperfine-State Rabi Oscillations

Among the most important abilities in our laboratory is the arbitrary manipulation of the internal hyperfine-ground state. As was already mentioned, we use  $^{87}\text{Rb}$  in its ground state, which has  $F = 1$  and  $F = 2$  possible hyperfine ground states, with the initially prepared hyperfine state  $|F = 1, m_F = -1\rangle$ . We have seen in section 2.1.4 that the hyperfine state can be changed using oscillatory magnetic fields that couple the magnetic dipole transition between ground-states. We will elaborate further on this experimental technique here.

We first consider a magnetic two-level system in an external bias magnetic field  $B_z$  (along a field quantization axis, here  $z$ ) with states  $|\uparrow\rangle$  and  $|\downarrow\rangle$ . The

system will later be subject to another, oscillating magnetic field  $B_{\text{rot}}\sin(\omega_{\text{rot}}t)$ . A magnetic two-level system is governed by the dipole Hamiltonian (we apply a rotating field):

$$\hat{H} = \vec{\mu} \cdot \vec{B}(t) = \vec{\mu} \cdot (B_z \vec{e}_z + \vec{e}_{\text{rot}}(t) B_{\text{rot}}).$$

After transforming into a co-rotating frame (rotating wave transformation) we obtain the typical Rabi-Hamiltonian [2, 162]:

$$\hat{H}_{\text{Rabi}} = \frac{\hbar}{2} (\delta \sigma_z + \text{Re}(\omega_R) \sigma_x + \text{Im}(\omega_R) \sigma_y), \quad (2.3)$$

where  $\delta = (\mu B_z)/\hbar - \omega_{\text{rot}}$  and  $\omega_R = \mu B_{\text{rot}}/\hbar$ . From here on out we will assume that  $\omega_R$  is real, an assumption which can typically be made if only one field of unchanging strength is used. Assuming that the initial state is  $|\downarrow\rangle$  the resulting time-evolution of the population in the  $|\uparrow\rangle$  state is:

$$P_{\uparrow}(t) = \frac{\omega_R^2}{\omega_R^2 + \delta^2} \sin^2 \left( \sqrt{\omega_R^2 + \delta^2} t / 2 \right). \quad (2.4)$$

This equation is visualized in Fig. 2.8 as a function of detuning  $\delta$ . In Fig. 2.8 we can see that for short pulses (compared to the Rabi-frequency  $\omega_R$ ) the width of the spectrum (vary detuning and keep pulse time fixed) is limited by the pulse time, while the width for large detunings is limited by the Rabi-frequency  $\omega_R$ . On the other hand, for constant detuning and varying time evolution we get the well known Rabi-oscillation. On resonance ( $\delta = 0$ ) we get full population transfer to the  $|\uparrow\rangle$  state with periodicity  $\omega_R$ , while off resonance we get partial transfer with shorter periodicity  $\sqrt{\omega_R^2 + \delta^2}$ .

This treatment for  $|\downarrow\rangle$  and  $|\uparrow\rangle$  generalizes for any magnetic-dipole allowed pair of states in the (weak-field) rubidium ground state (e. g.  $|1, -1\rangle \leftrightarrow |1, 0\rangle$  and  $|2, 0\rangle \leftrightarrow |1, \pm 1\rangle$  are allowed, while  $|1, -1\rangle \leftrightarrow |2, 1\rangle$  is dipole forbidden, see also Fig. 2.2).

Experimentally the oscillatory field is realized using either a single loop of copper wire mounted directly beneath the science-glass cell (for transitions within the  $F = 1$  and  $F = 2$  states,  $f \sim 10$  MHz) or using a microwave-waveguide antenna (for transitions between  $F = 1$  and  $F = 2$ ) which irradiates the atoms with radiofrequency radiation at 6.8 GHz (see also Fig. 5.1 (a)).

Transitions between these states can be detected by separating atoms in different hyperfine states by their magnetic moment by using Stern-Gerlach separation (see section 2.2.1). This horizontally separates the internal states with different magnetic moments, which means that the states  $|1, -1\rangle \leftrightarrow |2, 1\rangle$ ,  $|1, 0\rangle \leftrightarrow |2, 0\rangle$  and  $|1, 1\rangle \leftrightarrow |2, -1\rangle$  are still overlapped, see Fig. 2.5, where

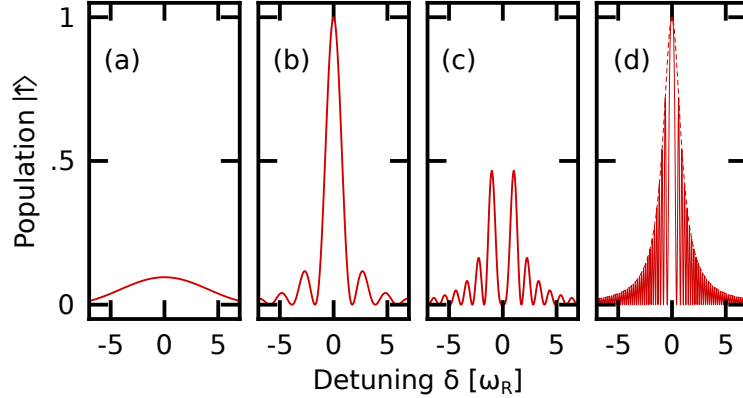


Figure 2.8: Rabi Spectra: Population transfer to the  $|\uparrow\rangle$  state when starting in the  $|\downarrow\rangle$  state as a function of detuning from resonance. Pulse areas are  $t \times \omega_R = \pi \times \{0.1, 0.5, 1, 10.5\}$  for (a), (b), (c), and (d), respectively. Dashed line in (d) is the Lorentzian envelope function  $\omega_R^2 / (\omega_R^2 + \delta^2)$ .

for example  $|2,0\rangle$  and  $|1,0\rangle$  show up in the same position horizontally and are only separated vertically. We circumvent this by first imaging only the  $F = 2$  atoms (which disperses them and pushes them out of the imaging region) using resonant cycling light ( $D_2$ ,  $F = 2 \rightarrow F' = 3$ , cycling light). Then we utilize the ability of our camera to shift illuminated pixels of the imaging region into a dark (unused) region of the chip (light to this region is blocked by a razor blade), and image the  $F = 1$  atoms by optically pumping them ( $D_2$ ,  $F = 1 \rightarrow F' = 2$ , repumping light) into  $F = 2$  and then imaging them the same way approximately 3 ms later. Then both illuminations are shifted up again further into the blocked off region of the chip, and create the reference image (illumination without atoms) another 3 ms later. We repeat this procedure without illumination of the camera to get the ‘dark’ picture for the three images created before, thus creating absorption images which allow a full reconstruction of the hyperfine ground state distribution.

These techniques can be combined to measure a Rabi-resonance curve. If we start with a fully polarized sample (all atoms in one hyperfine state (say  $|\downarrow\rangle$ )), the resulting time evolution of the Hamiltonian Eq. 2.3 is a Rabi oscillation of the form given in Eq. 2.4, which, for constant detuning  $\delta$ , is just a sinusoidal oscillation of the population between  $|\downarrow\rangle$  and  $|\uparrow\rangle$ , while for constant pulse time and varying detuning we get a sinc-squared response, typically referred to as Rabi spectrum. Figure 2.9 shows such a Rabi spectrum at low field (approximately 5 G) obtained by irradiating  $|1, -1\rangle$  atoms with

microwave radiation to transition to  $|2, 0\rangle$ . The extremely narrow line-width shows the good control of magnetic field. A more in depth discussion follows in chapter 5.

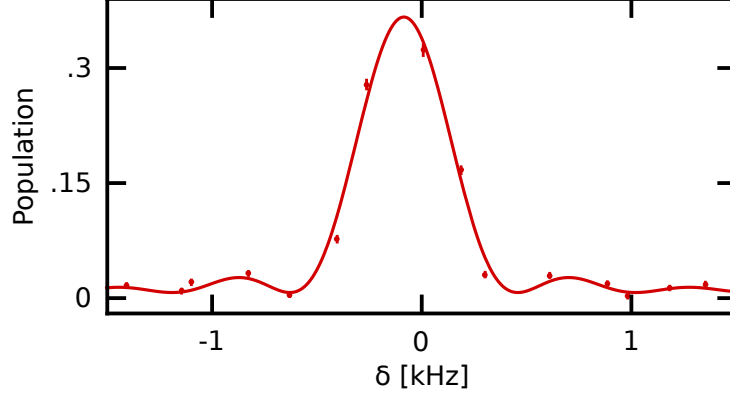


Figure 2.9: Rabi-resonance spectrum data for a Rabi-oscillation between  $|2, 0\rangle$  (initial state) and  $|1, -1\rangle$ . The pulse time here is 1.8 ms and the solid curve is a fit to the data with a Rabi-frequency of 114(2) Hz. The offset from zero frequency is due to a slight shift of the levels due to the optical trap shifting  $|2, 0\rangle$  and  $|1, -1\rangle$  very slightly differently.

## 2.2.4 Hyperfine Structure in Magnetic Fields

In the above section we mention the resonance condition. For alkali-metals in their ground state, we can find the resonant oscillation frequency of the individual allowed hyperfine pairs at finite magnetic field by calculating the magnetic field dependent energy of the involved hyperfine states. The eigenenergies of the respective hyperfine states only depends on one externally determined variable: the magnitude of the magnetic field  $B = |\vec{B}|$ . We will assume for simplicity that field is only applied in the z-direction ( $B \equiv B_z$ ). The eigenenergies of the hyperfine-ground states of an alkali atom can then be found using the Breit-Rabi formula [144, 163]:

$$E(J = 1/2, I, m_J, m_I, B) = -\frac{\Delta E_{\text{HFS}}}{4I + 2} + g_I \mu_B (m_I + m_J) B \pm \frac{\Delta E_{\text{HFS}}}{2} \sqrt{1 + \frac{4(m_I + m_J)x}{2I + 1} + x^2}, \quad (2.5)$$

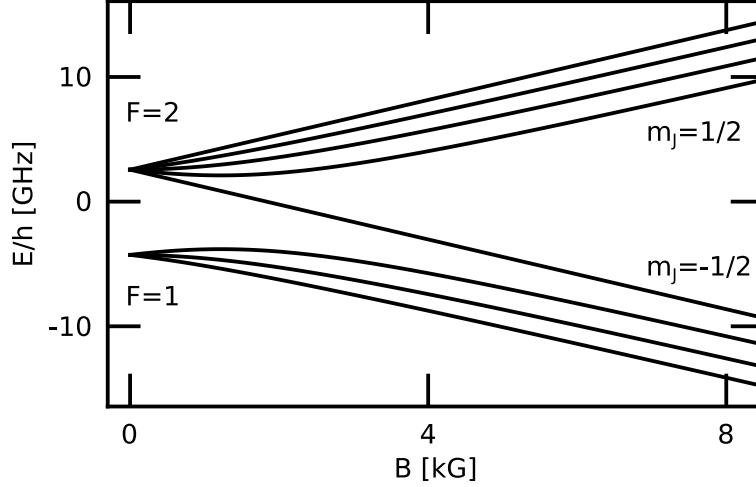


Figure 2.10: Breit-Rabi diagram for the  $^{87}\text{Rb } 5^2\text{S}_{1/2}$  ground state showing the energy dependence of the eigenstates of the Hamiltonian Eq. 2.5 on the external applied magnetic field. In the low field regime the  $F$  quantum number is a good quantum number (eigenstate of the Hamiltonian), while in the high field regime the  $z$ -projection of  $m_J$  (and  $m_I$ ) are good quantum numbers.

with  $x = \mu_B B (g_J - g_I) / \Delta E_{\text{HFS}}$  and  $\Delta E_{\text{HFS}}$  the hyperfine splitting between the ground states ( $F = 1$  and  $F = 2$  with projection quantum number  $m_F$  arbitrary) at zero external field. This formula assumes, that the magnetic fields involved are much smaller than the effective magnetic fields associated with spin-orbit coupling, i. e. that fine-structure splitting (for rubidium this is the energy difference between  $5^2P_{3/2}$  and  $5^2P_{1/2}$ ) is small compared to the Zeeman energies of the levels in a magnetic field (fulfilled for DC magnetic fields accessible in a laboratory). This ensures, that spin-orbit coupling ( $\vec{L}$  and  $\vec{S}$  to the total angular momentum  $\vec{J}$ ) is not influenced by the magnetic field, and thus  $|\vec{J}|^2$  and  $J_z$  are good quantum numbers. Note that this formula is only valid for the ground states of alkali atoms. In the case of excited states (e. g.  $5^2P_{3/2}$  or  $5^2P_{1/2}$ ) the full Hamiltonian for the hyperfine energies has to be solved numerically [144, 164].

## 2.2.5 State-Selective Trapping Potential

A core requirement in our laboratory and especially for the experiments described in chapter 7 is the ability to create a state-selective optical lattice, i. e. a lattice that depends on the hyperfine state which the atoms are in.

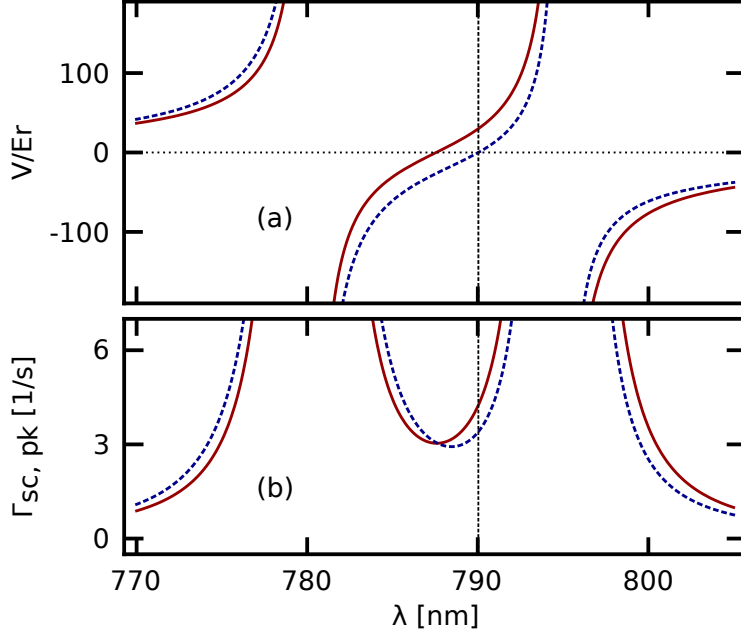


Figure 2.11: (a) State selective optical potential depth and (b) peak spontaneous scattering rates (b) as a function of wavelength calculated for the states  $|2, 0\rangle$  (dashed) and  $|1, -1\rangle$  (solid), with the tune-out wavelength ( $\lambda \sim 790.1$  nm) marked by the vertical dashed line for an intensity of  $0.38$  kW/cm<sup>2</sup>. The lattice potential depth here is  $V_{|1, -1\rangle} = 30E_r$  and the scattering rate is  $\Gamma_{sc, pk} = 4.3$  sec<sup>-1</sup> for  $|1, -1\rangle$  and  $\Gamma_{sc, pk} = 3.4$  sec<sup>-1</sup> for  $|2, 0\rangle$ . This is the configuration and state-pair used in chapter 7.

State-selective optical lattices have seen a lot of experimental efforts, including our group [92–96, 165–172]. A detailed description of state-selective optical potentials can be found in [88, 89, 173].

The basic idea behind a state selective optical lattice is that red-detuned light (light-frequency below the closest resonance) attracts atoms into higher intensity, while blue-detuned light (light-frequency above the closest resonance) repels atoms from regions of high intensity. When one now considers light of a frequency in the middle between two resonances, there must be a crossover point, where the atoms experience no potential (tune-out point). In general of course the tune out point will depend on the details of the excited states (i. e. how strong the coupling to the respective states is), but more interestingly, the tune out point also has to depend on internal state of the atom and polarization of the light (see also Fig. 2.2). We can imagine a pair

of states where selection rules would allow for one state to couple to both the blue-detuned and the red-detuned excited state, while the other state is only allowed to couple to the blue-detuned excited state, thus creating a situation where one of the states is ‘tuned out’, while the other state experiences effectively a blue-detuned optical potential.

For an atom with arbitrary excited state structure the optical potential from the AC-stark shift of a given ground state  $|i\rangle$  can be calculated using second order perturbation theory (the first order vanishes due to the absence of an electric dipole moment in neutral atoms), where the interaction-Hamiltonian of the light is given by the dipole operator [151]  $H_I = \vec{r} \cdot \vec{\mathcal{E}}$ :

$$\Delta E_i = \sum_{l \neq i} \frac{|\langle l | \vec{d} \cdot \vec{E} | i \rangle|^2}{E_i - E_l}.$$

We will now consider a situation as for  $^{87}\text{Rb}$  at near infrared wavelengths (approximately  $\lambda = 700$  nm to  $\lambda = 1400$  nm) where only the  $D_1$  ( $\lambda \sim 795$  nm) and  $D_2$  ( $\lambda \sim 780$  nm) lines are close by, and contributions from other states become negligible since they are so far off-resonant. The optical potential due to the laser induced coupling of the  $5^2S_{1/2}$  state to the  $5^2P_{1/2}$  and  $5^2P_{3/2}$  states then becomes [89] (neglecting counter-rotating terms):

$$U(\vec{r}, i, q) = \frac{3\pi c^2}{2} \left[ \frac{\Gamma_{D_1}}{\omega_{D_1}^3} \sum_{l \in P_{1/2}} \frac{|c_q^{li}|^2}{\omega - \omega_{li}} + \frac{2\Gamma_{D_2}}{\omega_{D_2}^3} \sum_{l \in P_{3/2}} \frac{|c_q^{li}|^2}{\omega - \omega_{li}} \right] I(\vec{r}),$$

where  $\Gamma_{D_{1,2}}$  is the scattering rate of the  $D_{1,2}$  transition,  $q$  denotes the polarization of the light (which can be  $\{\sigma^-, \pi, \sigma^+\}$ ),  $c_q^{li}$  are the Clebsch-Gordon coefficients which encode the coupling strength between two states at a given polarization and the transition frequencies  $\omega_{D_{1,2}} \approx \omega_{li}$ .

One of the great drawbacks of state-selective potentials is that they typically are still close enough to resonance that residual scattering is an issue. The scattering rate can be calculated by knowing  $\Gamma_{\text{sc}} = \Gamma_0 U / \hbar \Delta$  and applying it term-wise to the above equation, which yields [89]:

$$\Gamma_{\text{sc}}(\vec{r}, i, q) = \frac{3\pi c^2}{2} \left[ \frac{\Gamma_{D_1}^2}{\omega_{D_1}^3} \sum_{l \in P_{1/2}} \frac{|c_q^{li}|^2}{(\omega - \omega_{li})^2} + \frac{2\Gamma_{D_2}^2}{\omega_{D_2}^3} \sum_{l \in P_{3/2}} \frac{|c_q^{li}|^2}{(\omega - \omega_{li})^2} \right] I(\vec{r}).$$

In Fig.2.11 we show the resulting potential for the state-pair  $|1, -1\rangle \leftrightarrow |2, 0\rangle$  which will be used in chapter 7 at an intensity of  $380 \text{ W/cm}^2$

## 2.2.6 Bose-Hubbard Model and Interacting Bosons

As discussed in chapter 7, we start our experiments with an atomic crystal, which is generated by ramping an optical lattice into the strongly interacting regime. To better understand this, we first discuss the Hamiltonian for a single atom in an optical lattice:

$$\hat{H} = -\frac{\hbar^2 \nabla^2}{2m} + V_0 (\sin^2(k_r x) + \sin^2(k_r y) + \sin^2(k_r z)),$$

where  $k_r = 2\pi/\lambda$  is the recoil wavevector of the lattice potential and  $\lambda$  is the wavelength of the lattice light. We can solve this Hamiltonian by invoking the Bloch theorem [174, 175] for particles in periodic media which states that the eigen-wave-functions of a single particle in a periodic potential landscape has the property:

$$\phi_q(\vec{r}) = e^{i\vec{q}\cdot\vec{r}} u(\vec{r}),$$

where  $\vec{q}$  is the quasi-momentum (or crystal-momentum) and  $u(\vec{r})$  has the periodicity of the lattice (with  $\{a, b, c\} \in \mathbb{Z}$  and  $\{j, l, m\} \in \mathbb{Z}$  and  $\vec{r} = (x, y, z)$ ):

$$\begin{aligned} u(\vec{r}) &= u\left(\vec{r} + a\frac{\lambda}{2}\vec{e}_x + b\frac{\lambda}{2}\vec{e}_y + c\frac{\lambda}{2}\vec{e}_z\right) \\ &= \sum_{j,l,m} \alpha_{j,l,m} \exp[2ik_r(jx + ly + mz)] \end{aligned}$$

The eigenfunctions  $\phi_q(\vec{r})$  to the above Hamiltonian are called Bloch-waves, and because of the above equation, the quasi-momentum is periodic with period  $2k_r$ . All solutions for the above Hamiltonian are thus contained in the interval  $\{-k_r, +k_r\}$ , this interval is called the first Brillouin-zone. The eigenvalues form quasi-continuous ‘bands’ called Bloch bands, as is illustrated in the equations above and in Fig. 2.12 (for clarity only in one dimension).

The Bloch-wave-basis is fully delocalized in real space, but for the following discussion it is usually helpful to define a complementary, maximally localized basis called the Wannier states. The Wannier-states are restricted to a single Bloch-band  $B$ , and can be computed as follows:

$$w_B(\vec{r}) = N \sum_{\vec{q} \in \{BZ_1\}} \alpha(\vec{q}) \phi_{q,B},$$

where the summation is restricted to the first Brillouin-zone and the coefficients  $\alpha(\vec{q})$  have magnitude one and are chosen such that  $x^2$  expectation

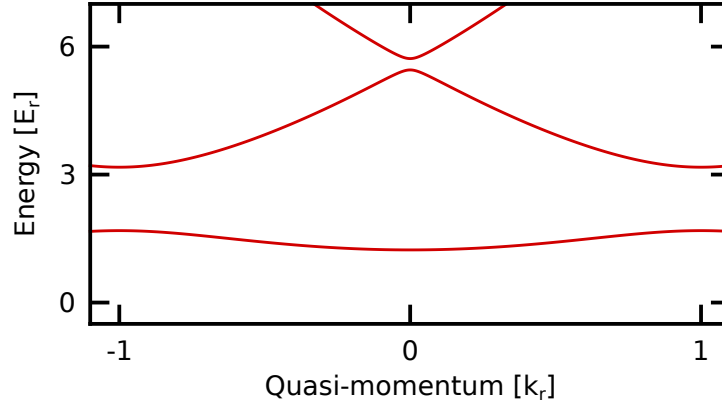


Figure 2.12: Lowest two Bloch-bands for a one-dimensional lattice of depth  $V_0 = 3E_r$  plotted as a function of quasi-momentum. Energy is in units of  $E_r = \hbar^2 k_r^2 / 2m$ .

value of  $|w_B(\vec{r})|^2$  is minimized (i. e. such that the Wannier-state is maximally localized), and  $N$  normalizes the Wannier-state. For very deep lattices, the Wannier-states become approximately harmonic-oscillator ground states, with harmonic oscillator frequency given by the harmonic approximation at the bottom of a lattice well:  $\omega_0 = 2\sqrt{V_0/E_r}E_r$  where  $E_r = \hbar^2 k_r^2 / 2m$ .

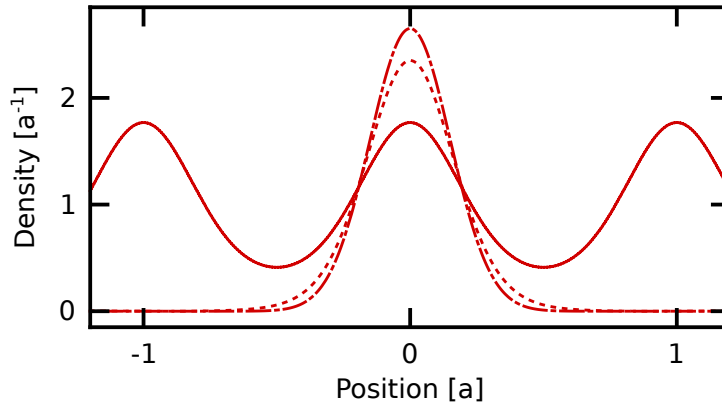


Figure 2.13: Comparison of the probability-density of Wannier-functions (short dashed), Bloch-functions (solid, normalized to one atom per unit cell), and the harmonic oscillator ground state for the harmonic approximation of the bottom of a lattice well (dash-dotted). Density is given in units of inverse lattice spacing.

For more than one atom (we are starting with a BEC), the full many-body Hamiltonian of contact-interacting atoms in a external potential  $V(\vec{r})$  is [6, 135]:

$$\begin{aligned} \hat{H} = & \int d^3\vec{r} \hat{\Psi}^\dagger(\vec{r}) \left( -\frac{\hbar^2 \nabla^2}{2m} + V(\vec{r}) \right) \hat{\Psi}(\vec{r}) \\ & + \frac{1}{2} \frac{4\pi \hbar^2 a_{\text{sc}}}{m} \iint d^3\vec{r} d^3\vec{r}' \hat{\Psi}^\dagger(\vec{r}) \hat{\Psi}^\dagger(\vec{r}') \delta(\vec{r} - \vec{r}') \hat{\Psi}(\vec{r}) \hat{\Psi}(\vec{r}'), \end{aligned} \quad (2.6)$$

where  $\Psi(\vec{r})$  and  $\Psi^\dagger(\vec{r})$  are the bosonic field annihilation and creation operators at position  $\vec{r}$ ,  $a_{\text{sc}}$  is the scattering-length which defines the strength of the contact interaction. The second term of Eq. 2.6 interactions come from the Born-approximation for atom-atom scattering, when we assume the low energy or s-wave limit [135]. We hence get a delta-shaped pseudopotential,  $4\pi \hbar^2 a_{\text{sc}} \delta(\vec{r}) / m$ , for the inter-particle interactions (contact interactions). We will assume that the atoms reside in a simple cubic lattice landscape of the form:

$$V(\vec{r}) = V_{\text{ex}}(\vec{r}) + V_l(\vec{r}) = V_{\text{ex}}(\vec{r}) + V_0 (\sin^2(k_r x) + \sin^2(k_r y) + \sin^2(k_r z)) .$$

Here,  $V_{\text{ex}}$  is a weak external trapping potential which localizes the sample to a finite region in space, as is typical in experiments.

If the lattice is deeper than all other energy-scales, such as temperature and interactions (typically already fulfilled for potentials deeper than  $3E_r$ ), then we can make a tight-binding approximation in the lowest Bloch-band, where we assume that particles in the Wannier states are mostly contained within single lattice sites (harmonic approximation) with the Wannier-states corresponding to the lowest Bloch-band  $w_0$ . We can then expand the bosonic field operators in the Wannier-basis:

$$\hat{\Psi}(\vec{r}) = \sum_j \hat{a}_j w_0(\vec{r} - \vec{r}_j) ,$$

where  $\vec{r}_i$  is the minimum of the  $i^{\text{th}}$  lattice site and summation  $i$  runs over all lattice sites (one two or three-dimensional). The operators  $\hat{a}_j$  and  $\hat{a}_j^\dagger$  are the bosonic annihilation and creation operators which annihilate or create an atom on site  $j$  (in the Wannier-state).

Inserting this expansion into the main Hamiltonian, allows us to carry out the integrations, and we arrive at:

$$\hat{H}_{BH} = J \sum_{\langle i, j \rangle} \hat{a}_i^\dagger \hat{a}_j + \frac{U}{2} \sum_i \hat{n}_i (\hat{n}_i - 1) + \sum_i \hat{n}_i (\varepsilon_i - \mu) .$$

This is the famous Bose-Hubbard Hamiltonian [60], with the tunneling strength  $J$  and the interaction parameter  $U$ . The last term is the mean-field of the model, with the site-dependent energy-offset arising from the weak external confinement  $\varepsilon_i \approx V_{\text{ex}}(\vec{r}_i)$ . The summation  $\langle i, j \rangle$  is over nearest neighbors only, with next-nearest neighbor tunnelings and higher order tunnelings neglected.

The tunneling strength  $J$  is calculated as follows:

$$J := J_i = \int d^3\vec{r} w_0^*(\vec{r} - \vec{r}_i) \left[ -\frac{\hbar^2 \nabla^2}{2m} + V_i(\vec{r}) \right] w_0(\vec{r} - \vec{r}_{i+1}) ,$$

where  $i + 1$  simply denotes any nearest neighboring site to  $\vec{r}_i$ . The onsite interaction parameter  $U$  is given by:

$$U = \frac{4\pi a_{\text{sc}} \hbar^2}{m} \int d^3\vec{r} |w_0(\vec{r})|^4 .$$

We will restrict the discussion to the repulsive case of  $a_{\text{sc}} > 0$ . The Bose-Hubbard model has two competing terms, where the first term is a tunneling term, which tends to delocalize the atoms, and the second term is an interaction term which penalizes two atoms sitting on the same site. The interactions tend to localize atoms on a site, since motion or tunneling often requires atoms to move onto already occupied sites.

For temperatures  $k_B T \ll \hbar J$  this competition causes a quantum phase transition [59]. The superfluid to Mott-insulator transition, where in the superfluid phase particles are completely delocalized and are coherent with respect to each other (i. e. phase stable so that they can interfere), while in the Mott-insulator phase atoms are localized on a site and are completely phase-incoherent (particles are in a product state). The transition happens when  $zJ \approx U$  where  $z$  is the coordination number or number of nearest neighbors (six for the simple cubic lattice). In our system, the temperature after ramp-up of the lattice is around 4 nK [93] giving  $k_B T / \hbar U \approx 0.1$ .

In the superfluid limit, the state of the system is:

$$|\Psi\rangle_{\text{SF}} \propto \sum_j \left( \hat{a}_j^\dagger \right)^N |0\rangle ,$$

where  $|0\rangle$  is the vacuum-state or the empty lattice, while in the Mott-insulator limit, the state is (for simplicity written here at exactly one particle per site) a product state of the form:

$$|\Psi\rangle_{\text{MI}} \propto \prod_j \hat{a}_j^\dagger |0\rangle ,$$

where as was already mentioned we have one particle per site which is phase-incoherent with the neighboring site.

The coherence manifests itself in the 3D Bose-Hubbard model in time-of-flight in ultracold atomic gases as sharp peaks in momentum space at momenta  $\{a2k_r, b2k_r, c2k_r\}$  (where  $\{a, b, c\} \in \mathbb{Z}$ ). A beautiful representation of this effect can be seen e. g. in Fig. 5 of reference [134], which is also an example for the superfluid-to-Mott-insulator transition of the Bose-Hubbard model for a cubic 3D optical lattice in our apparatus. The phase in which the atoms are predominantly in is however a function of mean field (or average number of particles per site), where particles are more likely to be localized if exactly one particle per site is in the lattice. Phase diagrams can be found for example in Figs. 1 and 2 of reference [176] and a mean-field phase diagram can be found for example in Fig. 6.2 of [90]. If a weak harmonic confinement is present at fixed  $J$  and  $U$ , the particles experience differing local densities and hence trace out a vertical line (a line along varying mean field and constant  $J/U$ ) in the phase diagram (and hence experience differing occupation numbers per site). This is studied directly for example in [177] and also in appendix B.2. In our experiment we typically load between  $3 \times 10^4$  and  $2 \times 10^5$  atoms into lattices of depths up to  $40 E_r$  depth (periodicity is either 532 nm or 395 nm). This results in interaction parameters of  $\sim 1$  kHz and tunneling strengths  $J/h$  between 1 Hz and 200 Hz (depending on lattice depth), which are occupied by up to 7 atoms per lattice site in the center for lattice periodicities of 532 nm and approximately  $2 \times 10^5$  atoms (see appendix B.2).

# Chapter 3

## Experimental Upgrades

Since I started in the group of Prof. Schneble we were able to implement several upgrades to the apparatus and the sequences for generating BECs (as discussed in chapter 2). As a result of these changes, we are now able to operate more stably, more reliably, and faster on a daily basis. These improvements turned out to be crucial for the measurements presented in chapter 7. The results depend on rapid data-taking to avoid the detrimental effects of drifts. We will present the changes and improvements in the following chapter.

### 3.1 Laser Cooling and Trapping

Creating the cycling light for the MOT/Molasses stage of the experiment requires a large amount of D<sub>2</sub>-cycling light, on the order of 100-500 mW, the larger the better typically. The light is generated using a Toptica DL-pro-780 master laser generating  $\sim 30$  mW of 780 nm light with linewidth  $< 500$  kHz. This light is amplified using a Toptica BoostTA laser amplifier which originally output  $\sim 900$  mW. Frequency-shifting using an AOM-double pass arrangement ( $\sim 50\%$  efficiency) and fiber coupling ( $\sim 50\%$  efficiency) left about 150 mW to 200 mW available for use in the MOT/molasses phase of the experiment.

We exchanged the amplifier chip with a 2 W chip (#TA -0780-2000-5), which can be driven at up to 1.5 W output given the BoostTA's control electronics and laser head. This increased the output to 350 – 400 mW of light available for the MOT, thereby significantly increasing the number of laser-cooled atoms (fluorescence as measured in section 3.3 increases by 50% for a 200 mW baseline and by 100% for a 150 mW baseline) while not greatly influencing the temperature at this (density-limited) stage. After transfer into the magnetic trap, the higher atom number allows for faster evaporation since

greater density increases the rethermalization rate (details below).

Finally we mention that the locking signal for the repump laser (for frequency stabilization of the laser to the  $D_2 F = 1 \rightarrow F' = 2$  transition), which used to be generated using polarization spectroscopy in a Rubidium vapor cell, is now generated by standard saturation-absorption spectroscopy (SAS) using a lock-in technique. The lock-point specific to the repumper transition drifts for polarization spectroscopy, but is much more stable for SAS, thus improving the stability of the laser locking, which now typically stays locked to the transition for the entire day (as opposed to several hours in the past).

## 3.2 Rubidium Source

The rubidium in our chamber originates from sublimation of a 1 g sample of a natural isotope mixture of bare rubidium metal inside the vacuum chamber. The rubidium was introduced into the vacuum chamber (in 2005/6 when the apparatus was first built) in a sealed glass vial behind an angle gate valve. The vial was broken after the vacuum chamber was evacuated. The vapor pressure of rubidium at room temperature is  $\approx 3 \times 10^{-7}$  mbar, which would mean that an atomic cloud would have a lifetime of less than a hundredth of a second, which is too short to transport it into the ultra-high vacuum part of our apparatus after transfer from the MOT into the magnetic trap. To control the rubidium vapor pressure, we have the rubidium valved off in a separate part of our vacuum chamber. Daily operation then traditionally consists of opening this valve for several hours (1-2 hours) a day until the pressure becomes too high (i. e. lifetime in the vapor cell too short), and then closing the gate-valve until the next day. Since the initial/final atom number strongly depends on the pressure in the cell (size of the MOT depends on pressure and transport loss depends exponentially on pressure), this means that the initial BEC size tends to drift over the course of a day. We were able to alleviate this problem considerably, with a full solution planned in the future.

The strategy is to simply cool the part of the chamber containing the vial with the rubidium metal, in order to lower the vapor pressure enough to have stable operation with the angle valve open permanently. When locally cooling the chamber, we will assume that the cool part emits a certain flow of rubidium which, in a flow equilibrium with the ion-pump, leads to a stable pressure below the room-temperature vapor pressure.

For a better understanding of the situation, we will develop a simple model to motivate how vapor pressure at the Rb-source corresponds to the pressure seen by the atoms in the MOT (for more details about vacuum, cf. [178]).

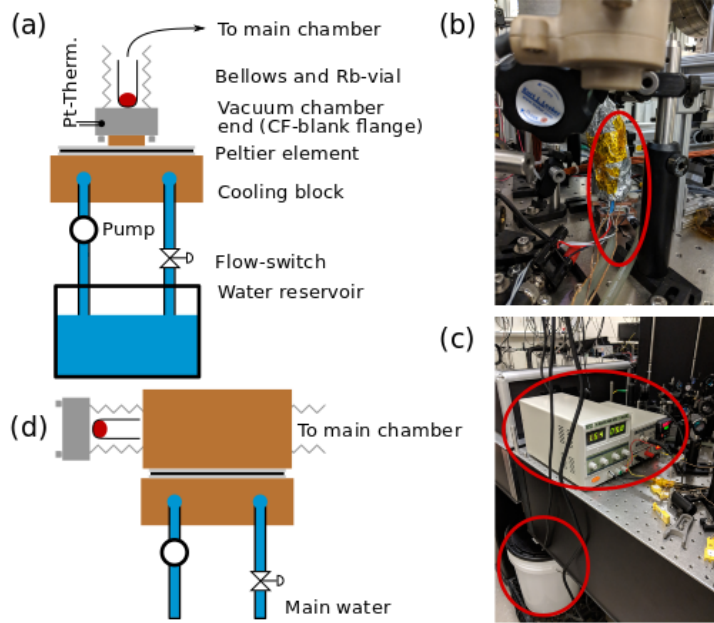


Figure 3.1: (a) Schematic of the temperature control described in the main text. The Rb-source in our experiment is rubidium metal in a glass vial (vial broken in the vacuum). The vial sits on top of a CF-blank flange inside of an approximately 10 cm long bellows. Temperature readings are taken using a platinum resistance thermometer glued to the CF-blank flange. The bottom of the flange is cooled using a cold finger contacted to a thermoelectric cooler. The waste-heat of the cooler on the hot side is carried away to a large reservoir (bucket) using water pumped by a standard aquarium pump. A flow meter switches off the power to the cooler in case of no or too little water flow. (b) Photograph of the setup in (a). (c) Photograph of the current source for the cooler, the Watlow PID controller, and the water reservoir, which contains the flow switch and the pump. (d) Planned future upgrade to the temperature regulation of the Rb-source for directly cooling elongated bellows.

A schematic which visualizes the parts used in the calculation and their connections is shown in 3.2. We start by approximating our vacuum chamber as consisting of two pipes in the molecular flow regime which are connected to each other while the ‘free’ end of each pipe is held at a constant pressure. The first pipe,  $IP_1$  (rubidium source), has a diameter  $d = 2$  cm and length  $l = 25$  cm and the second pipe,  $IP_2$  (MOT-chamber), has diameter  $d = 7$  cm and length  $l = 70$  cm. The pipes are connected to each other and the ‘free’ end of the  $IP_1$  is connected to a volume at rubidium vapor pressure  $p_{Rb}$  at varying

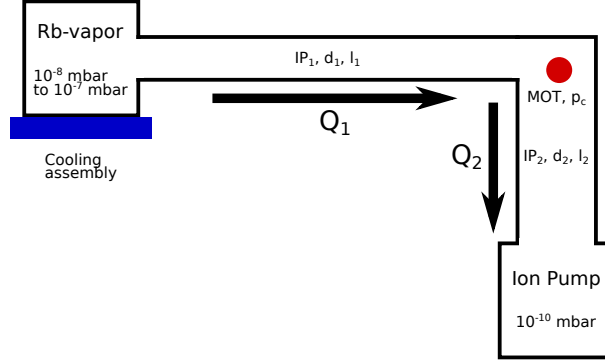


Figure 3.2: Schematic to visualize connections between vacuum parts which need to be considered to estimate flow-equilibrium. The source for the Rb-vapor is cooled, which adjusts the Rb-vapor pressure originating from the Rb-source. Two connected pipes link the Rb-source to the ion-pump, with the MOT approximately at the mating point of the pipes.

temperature  $T$  while the ‘free’ end of  $IP_2$  is connected to a pump, which we assume to be held at a pressure of  $p_p = 10^{-10}$  mbar. We can simply demand that the throughput  $Q = C * \Delta p$  (where  $C$  is the conductance) of each pipe is identical to get the pressure at key positions in the system. The conductance of a pipe in the molecular flow regime (i. e. pressures below  $10^{-3}$  mbar, which is always fulfilled for our system) is given by

$$C_{\text{mol}} = \frac{v_{\text{rms}} \pi d^3}{l},$$

where  $v_{\text{rms}}$  is the thermal rms velocity (of rubidium) at a given temperature and atomic weight,  $d$  is the pipe diameter and  $l$  is the pipe length. The conductances are then  $C_{1,2} = \{2.5, 37.7\}$  l/s (liters per second, where we neglect any variation in conductance due to temperature). We equate the throughputs and solve for the pressure at the connection  $p_c$  (which is the approximate location of the atoms in the MOT-loading position)

$$p_c = \frac{C_2 p_p + C_1 p_{\text{Rb}}}{C_1 + C_2}.$$

For rubidium at room temperature ( $p_{\text{Rb}} = 3 \times 10^{-7}$  mbar), the pressure at the connection point is  $p_c \approx 2 \times 10^{-8}$  mbar, which is about a factor of 10 to 20 too high compared to the desired pressure of approximately  $10^{-9}$  mbar.

Lowering the temperature by 5 K, 10 K and 20 K respectively, the pressure

at the connection becomes

$$p_c = \{8, 5, 1\} \times 10^{-9} \text{ mbar.}$$

Lengthening the first pipe to 50 cm results in

$$p_c = \{4, 3, 0.7\} \times 10^{-9} \text{ mbar,}$$

and lengthening the first pipe to 100 cm lowers the pressure to

$$p_c = \{2, 1, 0.4\} \times 10^{-9} \text{ mbar.}$$

A thermo-electric cooler (Peltier element) can easily achieve this temperature change and is compact enough to be added onto the current, very constrained setup, when using a compact water cooling block for removal of the waste-heat. The setup is shown in Fig. 3.1 (a) and (b). We use a standard TEC-127-06 Peltier cooler with a switchable current of  $\sim 2$  A, controlled by a Watlow temperature controller (PM6C1CA-AAAABAA) via an IXIS CPC1709J solid state relay. The waste-heat is carried away from the thermo-electric cooler using a copper block [179] cooled by flowing water. The water is supplied from a large bucket ( $\sim 20$  l) via a standard aquarium pump. A flow meter switches off the main power supply in case the water flow is impeded. Photographs and schematics of the setup are provided in Fig. 3.1.

After opening the gate valve when using a cooled Rb-source, we observe a decrease of lifetime of magnetically trapped atoms (which indicates an increase in pressure) in the region of the main vapor cell vacuum chamber (see Fig. 3.3 and Fig. 2.1). The increase crosses the critical value of lifetime ( $\sim 1$  s) after roughly 100 days (or three months). The slow increase is a function of the main chamber slowly equilibrating to the presence of an additional gas load (Rb-vapor) which slowly coats the walls of the MOT-chamber. For a more fine-grained observation time, the pressure can drop/rise on days where the laboratory temperature is slightly cooler or warmer, due to the walls of the vacuum vessel pumping a little more or less efficiently. The slow decrease of the pump performance also factors into the exact time evolution of this system. The revised schematic already gives a marked improvement over the situation before, where the valve to the Rb-source had to be opened and closed daily; now instead the valve has to be adjusted once every two to three months. The drift in background pressure can easily be compensated by e. g. changing the MOT-loading time slightly, changing one or two evaporation parameters or changing the power of light provided during MOT loading.

In the following we will discuss a straightforward adjustment that can be made in the future, where one would have to adjust the rubidium-source on

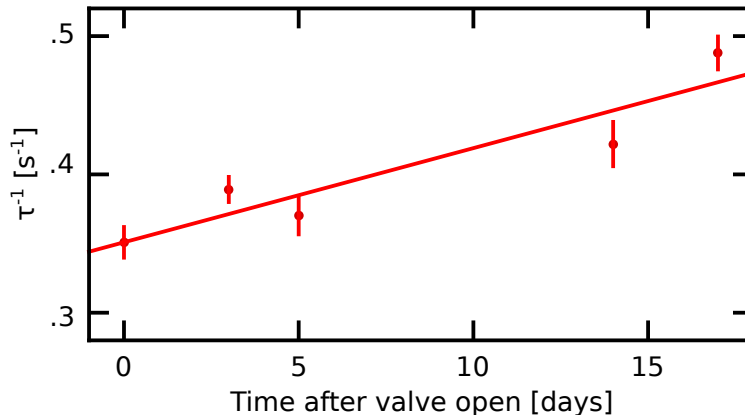


Figure 3.3: Measured (inverse) lifetime  $\tau^{-1}$  of magnetically trapped Rb-atoms after laser cooling. Time measured after the gate-valve was opened. The slow linear increase exceeds the maximum inverse lifetime ( $\sim 1 \text{ s}^{-1}$ ) after roughly 100 days, with no saturation visible in the finite observation time shown. Temperature of the Cf-blank-flange (see Fig. 3.1) was stabilized to  $\sim 0^\circ\text{C}$ .

the order of only once a year (see Fig. 3.1 (d)). The current cooling setup has several problems. First, the cooling element freezes over at the temperatures needed to maintain a low enough pressure, which eventually (over a timespan of several weeks) causes the control loop to be unable to reach the setpoint because the accumulating ice lowers the effective cooling power. Second, the device is essentially at the limit of what the cooler can feasibly do even without ice buildup. As seen in Fig. 3.3, the pressure at the MOT-cloud slowly creeps higher, and eventually reaches a point where its lifetime becomes too low. This is due to the pressure slowly equilibrating after the valve is opened, with no saturation observable in the finite time we measured. The final pressure is a function of temperature and differential pumping between Rb-source and the ion pump. Additionally, the water reservoir is not quite large enough to dissipate all the heat easily, so it heats up from approximately room temperature to approximately  $10 - 15^\circ \text{C}$  above it, which further reduces the cooling capacity. Finally cooling the CF-blank flange underneath the Rb-vial is not efficient, since most of the sample sits at a much higher temperature. It would hence be much more effective to cool the vacuum bellows directly.

A suggestion for an update is shown in Fig. 3.1 (d) where instead of cooling the bottom of the CF-blank flange, one could in principle use a much longer tube of approximately 50-100 cm length, which houses the Rb-vial at its end,

giving more flexibility and spatial access. One would now cool the bellows directly using a copper clamp, with minimal clamping force to cool a large part of the vacuum bellows. The cooling capacity can also easily be increased further by attaching the water to filtered tap water from the main water line, which is typically about 5 to 10 degrees colder than room temperature, as opposed to 10 degrees warmer than room temperature. The resulting decrease of the overall sample temperature along with the increased differential pumping due to the longer spatial separation between sample and main chamber would allow for much easier and therefore much more reliable control over the background pressure inside the main chamber. Since the vacuum system will need to be opened up in the future because of a slowly dying ion-pump, we can easily realize the aforementioned changes.

Finally, upon opening the vacuum chamber, one can use enriched  $^{87}\text{Rb}$  instead of natural abundance Rb (natural abundance of  $^{87}\text{Rb}$  in rubidium metal is roughly 28% [180]), which immediately would lower any unwanted background pressure significantly, thus lowering transport losses and increasing MOT size.

### 3.3 Optical Pumping

It is noted in section 2.1.5 that after the finishing the MOT/molasses phase, we optically pump the atoms from  $F = 2$  to  $F = 1$  and then capture only the  $|1, -1\rangle$  state in the magnetic trap. This lowers the atom number to essentially 30% of that in the initial MOT. It turns out that in our apparatus we can easily implement a more selective optical pumping into the  $|1, -1\rangle$  state (see Fig. 3.4). We now describe this improved scheme.

The level-structure and transitions involved are shown in Fig. 3.5. In the region of the MOT, the ambient field (Earth's magnetic field and stray fields in the laboratory) is zeroed for sub-Doppler cooling in the optical molasses using three single coils along the x, y and z directions. By switching off one of these coils during the optical pumping step, we provide a clear quantization axis/direction. If we send the pumping beam along this direction with a polarization of  $\sigma^-$  we preferentially (ideally even fully) pump into the  $|1, -1\rangle$  state, while the overall performance is unaffected. For this purpose, we simply rerouted the laser-beam to a new direction, and built an electronic switch for the coil current.

To determine the atom-number reliably, we first load the MOT, capture the atoms in the magnetic trap and then record the fluorescence signal which is observed after turning off the magnetic trap and turning the MOT back on

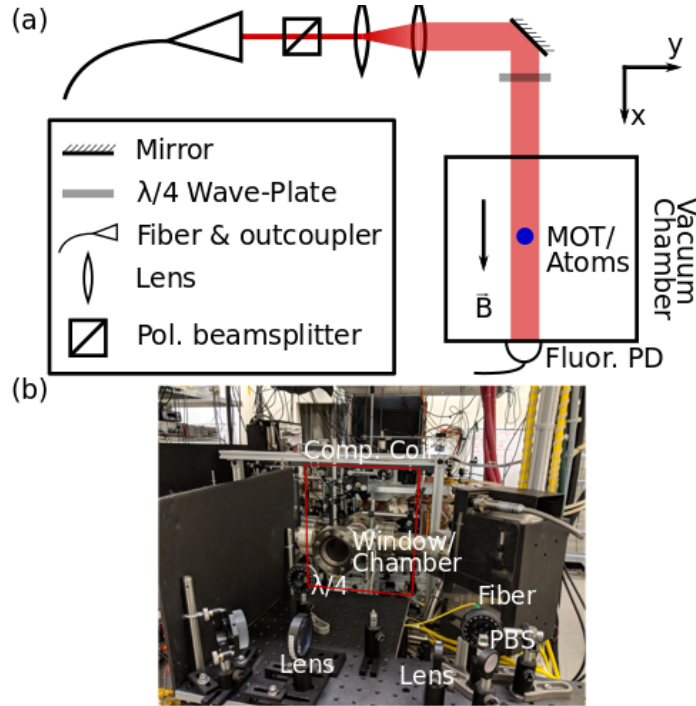


Figure 3.4: (a) Optical schematic for pumping the molasses-cooled atoms from the MOT. Light from a fiber is first linearly polarized by a polarizing beam splitter cube, expanded using a pair of lenses and finally circularly polarized using a  $\lambda/4$  waveplate before illuminating the atoms. External magnetic field (earth's magnetic field and stray fields in the laboratory) is provided by turning off the ambient magnetic field compensation coil in the propagation direction of the beam. (b) Photograph of the experiment with the individual parts labeled, showing directly the spatial position and size of the ambient field compensation coil.

(observation time  $\sim 100$  ms). The short observation time ensures that the MOT is not loaded during the observation. A direct comparison between the new and old performance is thwarted by the fact that the path of the light had to be permanently changed, and that the absolute atom number in the MOT (as detected via fluorescence with a photodiode) drifts throughout the day. However, we can compare the performance of the new optical pumping scheme to a scheme similar to the old one where we have no dedicated pumping beam, but simply turn off the repumping beam after molasses for 10 ms before catching the atoms in the magnetic trap. This repumps the atoms into  $F=1$  due to spurious absorption events into  $F' = 2$ , which is the baseline we will

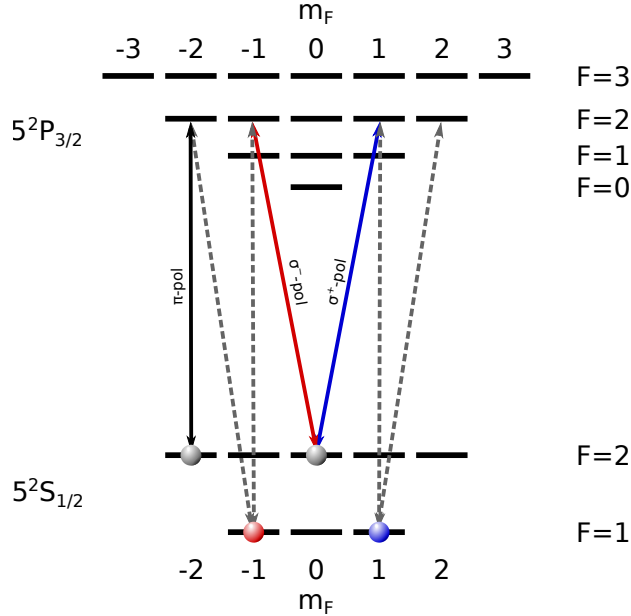


Figure 3.5: Level diagram for optical pumping.  $\sigma^+$ -polarized light (blue, solid) distributes population into more positive Zeeman-sublevels, which can then spontaneously decay (gray dashed) into  $F = 1$  (on average  $m_F$  does not change for spontaneous decay).  $\sigma^-$ -polarized light (red, solid), distributes population into more negative Zeeman-sublevels. Spurious  $\pi$  and  $\sigma^+$  polarization ensures that most of the population ends up in  $F = 1$ .

compare to. We then vary the waveplate angle and compare the fluorescence to the baseline measurement of regular optical pumping without a bias field to get the relative increase in captured atoms.

Assuming perfect conditions, we would expect the atom number to drop virtually to zero at a certain angle, indicating that we have perfect  $\sigma^+$  - polarization with all population ending up in the  $|1, 1\rangle$  state (henceforth this waveplate angle is  $\pi/2$ ). At  $\pi/4$  and  $3\pi/4$  waveplate angle, we then get linear polarization, which in this coordinate frame is an equal superposition of  $\sigma^+$  and  $\sigma^-$  polarization, so all  $F = 1$  hyperfine states are thus similarly likely to be occupied, and the fluorescence increase is close to unity. At zero and  $\pi$  waveplate angle we expect near perfect  $\sigma^-$  polarization. Therefore we expect essentially all atoms to end up in  $|1, -1\rangle$  (the state which we want to trap), resulting in an enhancement factor of about three.

Realistically, we cannot get a perfectly polarized sample after just one step of optical pumping, because our initial state after the molasses phase is a

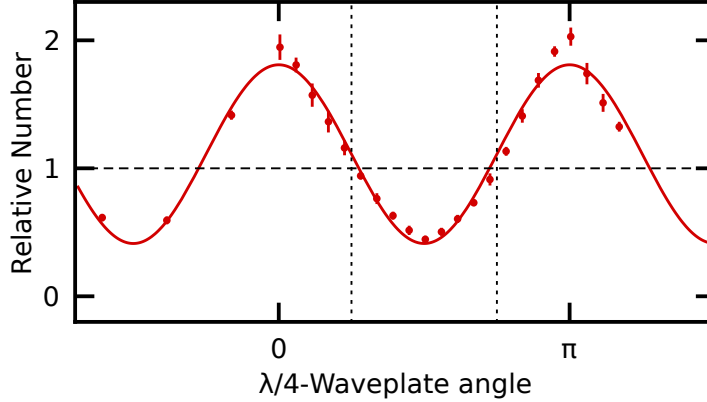


Figure 3.6: Fluorescence signal for the new optical pumping scheme divided by fluorescence for the old scheme (using optical pumping of molasses only by turning off repumping light). The fluorescence is proportional to atom number captured and is plotted as a function of the angle of the  $\lambda/4$ -waveplate immediately before the beam enters the chamber (see Fig. 3.4). Solid line is a sine function fitted to the data as a guide to the eye. Horizontal dashed line is at unity and vertical dashed lines are at  $\pi/4$  and  $3\pi/4$ .

perfect mix of all hyperfine states of  $F = 1$  and  $F = 2$ . Let us consider again a perfectly  $\sigma^-$  polarized beam. Starting with a finite fraction of atoms residing in the  $|2, 2\rangle$  state, these atoms can absorb a photon from the optical pumping beam and will transition to the excited hyperfine state  $|2', 1\rangle$ , which can decay to the states  $|1, \{0, 1\}\rangle$  and to the states  $|2, \{0, 1, 2\}\rangle$ . Since the atom cannot absorb if it is in any  $|1, m_F\rangle$  state, a decay to  $F = 1$  means that this atom is lost for magnetic trapping.

Figure 3.4 shows the result of conducting this experiment, where we change the waveplate angle and compare to a scenario where we pump by turning off the repump beam. The above reasoning explains why the fluorescence increase does not drop to zero for a waveplate angle of  $\pi/2$  and why the fluorescence increase is only roughly two and not three: a significant portion of the atoms (presumably about one third) ends up in the  $|1, \{0, 1\}\rangle$  states for  $\sigma^-$  polarization of the light, which results in an increase to two-thirds of all atoms which can be optically-trapped (from initially one third). Similarly about one sixth of all atoms land in the  $|1, -1\rangle$  state if we use  $\sigma^+$  polarization, which results in an enhancement factor of roughly one half.

The heating due to this process is negligible, since the atoms scatter on average less than 3 photons before ending up in an  $F = 1$  and therefore becom-

ing dark. The temperature imparted by a photon recoil is only about 200 nK where the temperature after molasses is on the order of  $\sim 10 \mu\text{K}$ . While the pumping efficiency is not 100%, the number of atoms has still approximately doubled at negligible additional heating, thus increasing evaporation speed later in the sequence.

In the future, one could imagine a second step of optical pumping, where after the first step of optical pumping is finished, one uses a new  $\sigma^-$  polarized repumping beam which counter-propagates with the pumping beam to put the atoms back to  $F = 2$ , and then adds a second identical optical pumping step to increase the number of optically-trappable atoms even further. A counter propagating beam is likely required to not impart too much linear momentum and displacement during the pumping phase. While this procedure should, in principle, increase the number of atoms even further, it cannot be easily realized in our current apparatus due to geometric constraints. It should be noted too that only a smaller marginal number gain would result at the cost of a much higher complexity.

A caveat of the optical pumping method described in this section is that for the case of perfect  $\sigma^-$  - polarization, a small fraction of the population will get trapped in the state  $|2, -2\rangle$  due to not being able to absorb any light (off-resonant absorption to the  $|3, -3\rangle$ -state is irrelevant since it can only decay back to  $|2, -2\rangle$ , see also Fig. 3.5). Any population left in this state will be quickly expelled when turning on the magnetic trap due to  $|2, -2\rangle$  being magnetically anti-trapped, resulting in a loss on the order of 20% to 30% of the MOT loaded atom number. In a realistic experimental setup the polarization will not be perfectly  $\sigma^-$  due to small relative misalignments of the direction of the beam and the magnetic field or due to the initial polarization of the beam being not perfectly linear (extinction ratio for the unwanted polarization of typical polarizing beam splitters is on the order of  $10^{-3}$  [181]). At a scattering rate of  $> 10^6$  per second for the main polarization, even a fraction  $10^{-3}$  in a different polarization will empty the  $|2, -2\rangle$  - state in less than 1 ms.

### 3.4 Quadrupole Magnetic Coils

The re-design and exchange of our quadrupole-trap magnetic coils, which now also allow accessing a Feshbach resonance at  $\sim 1 \text{ kG}$  [35, 182] when used in Helmholtz-configuration, will be detailed in a dissertation written by our colleague A. Pazmiño. The maximum axial field gradient changed from  $b \approx 350 \text{ G/cm}$  to  $b \approx 480 \text{ G/cm}$ .

### 3.5 Evaporation Speed Increase

Because we start with a denser and hotter cloud (adiabaticity of compression from 350 G/cm to 480 G/cm is assumed), the evaporation can be sped up. As is discussed in [131] for the case of quadrupole potential, an increase of the trap gradient by  $\eta$  results in an increase of the trap density by  $\eta$  and an increase in the temperature of  $\eta^{2/3}$ . In the case of the TOP trap, an increase in gradient by  $\eta$  results in an increase in the trap frequencies by  $\eta$  (all else unchanged). Then the density increases by  $\eta^{3/2}$  and the temperature increases by  $\eta$ . In [132] it is shown that elastic scattering is proportional to density times square root of temperature ( $\Gamma_{\text{el}} \propto n\sqrt{T}$ ). Since in our case  $\eta \approx 1.4$ , the evaporation speed can then be increased by a factor of  $\eta^{4/3} \approx 1.5$  in the quadrupole trap and by a factor of  $\eta^2 \approx 1.9$  in case of the TOP trap. Furthermore, due to optical pumping and more power in the cycling beam, we now have approximately 3 to 4 times as many atoms as initially in the magnetic trap, which correspondingly allows the evaporation to be sped up by approximately that same factor.

We note that once the atoms are cool enough to be loaded into the optical dipole trap ( $\sim 2 \mu\text{K}$ ), the trapping frequencies of the optical dipole trap are  $\omega_i \approx 2\pi \times 80 \text{ Hz}$ , and their geometric mean does not go lower than  $\bar{\omega} \approx 2\pi \times 60 \text{ Hz}$  for typical evaporation, while the geometric mean of the TOP-trap frequencies is, even with the new coils, only  $\bar{\omega} \approx 2\pi \times 50 \text{ Hz}$  (changed from  $\bar{\omega} \approx 2\pi \times 35 \text{ Hz}$ ). Therefore, our long-established strategy of loading the ODT as early as possible (limited by its  $\sim 5 \mu\text{K}$  depth) remains unchanged.

In historical sequences, the TOP evaporation was continued essentially to the point of BEC in the TOP trap, with evaporation in the optical trap essentially only compensating for the heating which results from the transfer process between TOP and ODT, including three full stages of evaporation in the TOP, all taking on the order of 10 s. With the changes outlined above, we transfer from the quadrupole trap to the TOP-trap at roughly 50  $\mu\text{K}$  and we need only one stage of evaporative cooling in the TOP (now only taking  $\sim 5 \text{ s}$ ) before we can transfer into the ODT, where evaporation is concluded in  $\approx 2 \text{ s}$ . Overall, the changes to the trap loading and evaporation sequence result in a very significant overall reduction of the cycle time for BEC production from 90 s to 20 s.

### 3.6 Summary and Current Performance

Another result of the above upgrades is the increased stability of daily operation. In Fig. 3.7 we show the current atom number stability during a typical

	MOT load	MT load & move	MT evap. (QP & TOP)	ODT load & evap.	image & move & misc.
old	14 s	(0.5+4.5) s	(15+37) s	(1+3.5) s	(3+5+1) s
new	3.5 s	(0.3+2.2) s	(4+4) s	(1+2) s	(1+1+1)s

Table 3.1: Comparison of old and new sequences, detailing the duration for production of a BEC. Old sequences achieve BEC in approximately 85 seconds while new sequences achieve BEC in approximately 20 seconds. Miscellaneous (Misc.) is the time between sequences, the second move step returns the transporter to its original position.

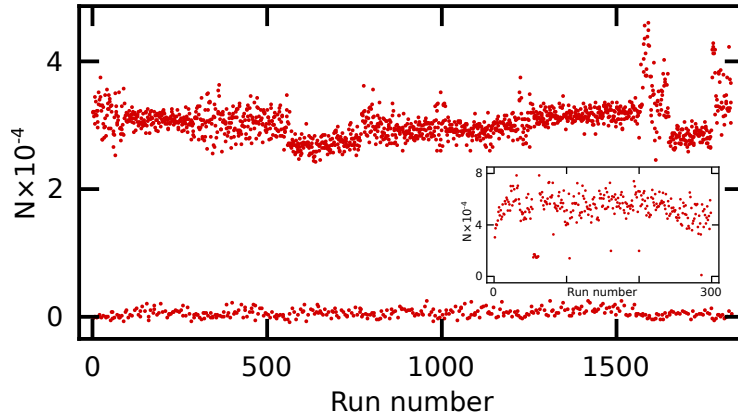


Figure 3.7: Typical BEC number stability. Data taken on two separate days, the second day starts at run number 1595. Total number drifts slowly throughout the day; small adjustments are made using MOT-loading time. Zero atom runs are the reference images described in chapter 4. Inset: Typical number-stability in 2011, before the changes were made to stabilize number. Total atom-count drifts quickly, with higher variance than in the main figure.

day of taking data for a publication, compared to a typical day of taking data for a publication in the past. We see that the stability of produced BEC sizes is much improved, and drifts are also decreased and easily compensated for. Finalizing the changes suggested in 3.2 should get rid of drifts experienced during a typical day, with only minor adjustments needed in e. g. MOT loading time, MOT beam powers or evaporation time to set atom-number to the desired (or previous day's) value.

# Chapter 4

## Image Analysis

### 4.1 Backgrounds and Fringes

As is outlined in section 2.2.1, we use coherent (spatial and temporal), resonant light to image the shadow cast by the atoms in the science cell onto a CCD chip. In a raw image, any sort of imperfection, such as a speck of dust, can cause circular fringes in the image plane. Also close-to-plane-parallel surfaces in the beam path will cause ‘etaloning’, resulting in linear fringes. Typically most of these fringes are easily taken care of in standard absorption imaging [130] by taking three total images: (a) illuminate the CCD with atoms present, (b) illuminate the CCD without atoms present and (c) take a dark image without illumination. Then the absorption of light by the cloud of atoms can easily be calculated as  $(a-c)/(b-c)$  (see also section 2.2.1).

This, of course, assumes that the fringes are stable in time. To the best of any experimenter’s ability, this can be nearly achieved by building optical systems which are maximally stable and not prone to any sort of vibration (use optical benches, short posts, non-adjustable optics, water-cooled CCD camera without fan) and which are unaffected by air currents and accumulating dust. One can further reduce the impact of time-dependence by taking signal and reference images as close in time as possible. However, regardless of the care taken to eliminate any problems, the combination of temporal separation, acoustic noise and air currents (to some small residual degree) will cause a slight movement of the fringes. The actual relative movement of the fringes is hard to predict a priori, and one could in principle have many fringes moving (seemingly) arbitrarily and independently of each other, with the maximum complexity of the problem (i. e. parameters which need to be monitored) limited only by the number of pixels on the camera ( $10^6$ ).

As we will see in this chapter, the situation is fortunately often not quite so dire, and only a limited set of ‘typical’ fringe motions is actually relevant. We will pick out the set of typical fringes using the technique of principal component analysis.

## 4.2 Reference Fringes

The technique described here is based on work conducted in Hamburg, Amsterdam and Shanghai [183–186]. We start with a set of empty absorption images ( $\{\mathbf{R}_j\} = (a - c)/(b - c)$ ) called reference images, obtained by simply not loading the MOT before running the sequence as normal. As stated previously, slow accumulation of dust over the course of the experiments has to be factored in, so the optimal set of fringes may be time dependent. In our case this was done by gathering these reference images interleaved with data taking (typically every fifth image) instead of before/after data taking. This allows the basis of reference images to include any changes that happen over the course of taking the data.

## 4.3 Principal Component Analysis

The tool to analyze the large amount of images and find or filter out the fringes that occur is principal component analysis (PCA) [187]. PCA is typically conducted on a data set  $\{\mathbf{D}_j\}$  where each data point  $\mathbf{D}_j \in \mathbb{R}^n$  is a real  $n$ -vector and the dataset has zero mean  $\sum_j \mathbf{D}_j = 0$ . PCA then finds the eigenvectors of the covariance matrix of the full data set  $\underline{A} = [\mathbf{D}_1, \mathbf{D}_2, \mathbf{D}_3, \dots]$  [187]:

$$\underline{C} = \underline{A} \cdot \underline{A}^T,$$

ordered by magnitude of the corresponding eigenvalue (the largest eigenvalue giving the first principal component). Each principal component  $\mathbf{P}_i$  (in our case representing a fringe pattern) lives in the same vector space  $\mathbb{R}^n$  as each data point  $\mathbf{D}_j$  (a typical image containing fringes and the absorption signal from the atoms). The first principal component  $\mathbf{P}_1$  is the direction in this space that has the greatest variance, i. e.  $\sum_j (\mathbf{P}_1 \cdot \mathbf{D}_j)^2$  is maximized, so that there is no other vector  $\mathbf{P}'$  along which greater scatter is observed. The second principal component is the direction orthogonal to the first principal component along which the biggest scatter occurs. The third principal component is the direction orthogonal to the first and second principal component along which the biggest scatter occurs. In other words, PCA yields an orthogonal

(and, if normalized an orthonormal) basis, which is only complete when the dataset has more (linearly independent) entries than the dimensionality of the vector space of  $\mathbf{D}_j$ .

Similar to the use of PCA in reconstructing faces in the ‘eigenface’ method [188], here it is used to identify the most important (read: most variance) features from a data set (read: BEC-absorption images with fringes). PCA thus allows for the reconstruction of a given data point (new or present in the current set of data) using only the few most important principal components. In our case we can easily cast the two-dimensional reference images  $\mathbf{R}_j$  with pixels  $R_{x,y}^j$  into vector form  $R_k^j$  where, e. g.  $k = x + \dim_x \times y$ , and  $\dim_x$  is the number of pixels in the x coordinate. We then subtract the mean image  $\mathbf{R} = \sum_j \mathbf{R}_j / N$  ( $N$  is the total number of images) from each  $\mathbf{R}_j$  to generate the data set  $\{\mathbf{r}_j\} = \{\mathbf{R}_j - \mathbf{R}\}$  on which we can perform PCA yielding the normalized principal components  $\mathbf{p}_i$ .

A new image with atoms,  $\mathbf{R}_{\text{Atom}}$ , will be processed by first subtracting the mean image,  $\mathbf{R}$ , to give  $\mathbf{r}_{\text{Atom}} = \mathbf{R}_{\text{Atom}} - \mathbf{R}$ , and by then calculating the overlap of that subtracted image with the first few (typically  $n = 5 - 20$ ) normalized principal components. The processed image is then

$$\mathbf{R}_{\text{Atom, proc}} = \mathbf{r}_{\text{Atom}} - \sum_{i=1}^n (\mathbf{p}_i \cdot \mathbf{r}_{\text{Atom}}) \times \mathbf{p}_i.$$

We take reference images ( $\mathbf{R}_j$ ) throughout typical data-taking (‘training set’ of images). For the final analysis, we compute the principal components and mean from all reference images, and we then analyze (process) all atom images with the mean and principal components computed from these reference images. One should note that each image is also shifted to have zero mean individually, i. e. the set which is used to create the principal components is actually

$$\{\mathbf{r}'_j\} = \{\mathbf{r}_j - \mathbf{1} \langle \mathbf{r}_j \rangle\},$$

which means that for the data matrix each column-vector and each row-vector have zero mean. Consequently, an image inside the ‘training set’ of reference images can be recreated as follows:

$$\mathbf{R}_j = \mathbf{R} + \mathbf{1} \langle \mathbf{r}_j \rangle + \sum_i \mathbf{p}_i (\mathbf{p}_i \cdot \mathbf{r}'_j).$$

On the other hand, new images that are not part of the ‘training set’ can only be recreated approximately, unless the number of training-images (and hence the number of non-vanishing principal components) exceeds the number of pixels, which is a prohibitively large set of images ( $\approx 10^5$ ).

For new images to be processed, we will typically only subtract the mean of the reference fringes ( $\mathbf{R}$ ) and the overlap with the principal components multiplied by the respective principal component. While one should technically still zero the mean of the new image which we want to process (i. e. subtract  $\mathbf{1}\langle\mathbf{r}_{\text{Atom}}\rangle$ ) this is complicated by presence of actual atoms, which shift the expectation value of the mean ( $\langle\mathbf{r}_{\text{Atom}}\rangle$ ) of the new image away from zero. A better approach is to zero the optical density in an empty region close to or surrounding the atoms.

## 4.4 Discussion of Errors

With the implementation thus far, we make an (albeit very minimal) error introduced by the small residual overlap between the principal components and the actual atom signal. To understand this, we can imagine an image as created as follows:

$$\mathbf{R}_{\text{Atom}} = \mathbf{0} + \mathbf{SN} + \mathbf{FR} + \mathbf{A}.$$

An ideal image would have optical density 0 everywhere. A real image on top of that would then have shot noise,  $\mathbf{SN}$ , (from the shot noise from photons counted per pixel) as well as the aforementioned fringes,  $\mathbf{FR}$ , and finally the signal of the atoms we are actually looking for:  $\mathbf{A}$ .

The effective dimensionality of the shot-noise images is the number of imaged pixels, but it does not induce any systematic shift. The shot noise on each pixel is (approximately) proportional to the inverse square root of the counts at the pixel ( $\sqrt{N_{\text{pix}}}^{-1}$ ), which for our 16-bit camera is on the order of  $\approx 0.01/\text{pix} \hat{=} \pm 1 \dots 10 \text{ atoms/pix}$ . With enough images to average over ( $> 100$ ), the  $\mathbf{SN}$  part contributes mostly to late principal components (i. e. beyond the 20th principal component). The overlap of new realizations of  $\mathbf{SN}$  with the used principal components is non-zero but very small, with an expectation value of zero, so that this contributes no net systematic error.

The  $\mathbf{A}$  signal, on the other hand, can have a systematic nonzero overlap with the principal components. We should expect the overlap to be extremely small, simply because the vector space associated with a typical image is so extremely large (approximately  $10^5$  basis vectors) compared to the few principal components  $\sim 10$  used, so we expect overlap by coincidence to be limited to  $10^{-4}$  (in other words, it is unlikely that the atomic distribution looks like a fringe). Furthermore the principal components typically have non-zero components all over the image, while the atom signal is typically localized.

In practice, the overlap is on the order of  $< 0.1 \text{ atoms/pix}$  for  $10^4$  atoms and  $< 1 \text{ atom/pix}$  for  $10^5$  atoms, most of which is a shift of the mean, which

can be easily subtracted off in later image processing of the region immediately neighboring the atoms (for comparison, the residual fringing on the other hand is on the order of 2 atoms/pix or larger). If large atom numbers ( $N > 5 \times 10^4$ ) are used, one however needs to worry about this residual overlap, which will be briefly discussed in the next section.

## Masking the Atomic Signal

In this section we discuss how the removal of fringes can be achieved with high fidelity even if large atomic clouds are in the image by masking out the atomic signal. This is not used for the analysis in chapter 7, so the reader may wish to initially skip to section 4.5.

If large atom numbers are required, one should ‘mask-off’ the region/regions which contains or will contain the atoms (with the masked area being rather a little too small than too large, i. e. just the size of the cloud rather than twice the size of the cloud). An example of a mask is shown in Fig. 4.2 (b). An implementation of the masking is as follows. The mask  $\mathbf{m}$  is an image-sized array with 0 in the ‘mask region’ and 1 everywhere else, and is simply multiplied pixel by pixel onto the mean subtracted image  $\mathbf{r}_{\text{Atom}}^m = \mathbf{m} \times \mathbf{r}_{\text{Atom}}$ . However, when the same is done with the principal components  $\mathbf{p}_i^m = \mathbf{m} \times \mathbf{p}_i$ , this introduces an error since the masked principal components  $\mathbf{p}_i^m$  are now neither normalized nor orthogonal to each other. Luckily we can mitigate this fact by following a procedure similar to the one outlined in [185], and least-squares-fit the masked principal components to the masked mean subtracted image:

$$\text{Min} \left[ \left( \mathbf{r}_{\text{Atom}}^m - \frac{c_0^m}{\sqrt{N_{\text{pix}}}} \mathbf{1}^m - \sum_i c_i^m \mathbf{p}_i^m \right) \cdot \left( \mathbf{r}_{\text{Atom}}^m - \frac{c_0^m}{\sqrt{N_{\text{pix}}}} \mathbf{1}^m - \sum_i c_i^m \mathbf{p}_i^m \right) \right],$$

The constant component  $c_0/\sqrt{N_{\text{pix}}}\mathbf{1}^m$  allows for mean-centering the image, which needs to be included now since it would otherwise interfere with the optimization.

We will consider the constant offset as the ‘zeroth’ principal component ( $\mathbf{p}_0 := \mathbf{1}^m/\sqrt{N_{\text{pix}}}$ ). We can then write:

$$\text{Min} \left[ \left| \mathbf{r}_{\text{Atom}}^m - \sum_{i=0} c_i^m \mathbf{p}_i^m \right|^2 \right].$$

We can easily calculate an analytic solution to this problem given a finite set of principal components rather than numerically optimizing each time a

new picture comes in. To do this we first take the partial derivative of the above equation for a single coefficient  $c_l$  (Latin summation is over principal components and Greek summation is over pixels):

$$\begin{aligned} \frac{\partial}{\partial c_l^m} \sum_{\alpha} (r_{\alpha}^m - \sum_{i=0} p_{\alpha,i}^m c_i^m)^2 &= 0 \\ \frac{\partial}{\partial c_l^m} \sum_{\alpha} (r_{\alpha}^m - 2 \sum_i r_{\alpha}^m c_i^m p_{\alpha,i}^m + \sum_{i,i'} c_i^m c_{i'}^m p_{\alpha,i}^m p_{\alpha,i'}^m) &= 0 \end{aligned}$$

which yields:

$$\begin{aligned} \sum_{\alpha,i} p_{\alpha,i}^m p_{\alpha,i}^m c_i^m &= \sum_{\alpha} r_{\alpha}^m p_{\alpha,l}^m \\ \sum_i B_{l,i} c_i^m &= \sum_{\alpha} r_{\alpha}^m p_{\alpha,l}^m. \end{aligned}$$

The matrix  $\underline{B}$  is the product of the matrices  $\underline{PC}^T \cdot \underline{PC}$ , and  $\underline{PC}$  has columns  $\mathbf{p}_i^m$  which are the principal components and the number of columns is the number of principal components used.  $\underline{B}$  is a square, symmetric matrix whose number of columns is equal to the number of principal components used. The component weights for reconstruction are then simply

$$c_l^m = \sum_{n,\alpha} B_{l,n}^{-1} p_{\alpha,n}^m r_{\alpha}^m.$$

This can be written in vectorial form also, as

$$\vec{c}^m = (\underline{PC}^T \cdot \underline{PC})^{-1} \cdot \underline{PC}^T \cdot \mathbf{r}^m.$$

This makes it a little easier to understand what the final result of the optimization is: If we assume that we have started out with unmasked principal components  $\mathbf{p}_i$ , we predicted that the result for the weights of the individual principal components should be  $c_i = \mathbf{p}_i \cdot \mathbf{r}$ . Now if we consider that the principal components before masking were orthonormal, then the  $\underline{B}$  matrix is simply the identity  $\underline{B} = \mathbb{1}$ , so our initial heuristic of simply computing component vector overlap is confirmed here independently. The picture of least squares optimization generalizes this to a basis which is not orthonormal. In cases where the components are not normalized, the matrix  $\underline{B}$  is still diagonal with entries that are the square of the normalization for each principal component, and if the components are neither orthogonal nor normal, the matrix  $\underline{B}$  becomes off-diagonal, thus compensating for the non-orthogonality.

The processed image is then found using the new principal component weights  $c_i^m$  along with the unmasked principal components:

$$\mathbf{R}_{\text{Atom, proc}} = \mathbf{r}_{\text{Atom}} - \sum_{i=0} c_i^m \mathbf{p}_i,$$

as opposed to the original principal component weights  $c_i = \mathbf{p}_i \cdot \mathbf{r}$ .

For the analysis done in chapter 7 we will proceed without masking, since the involved atom numbers are suitably small (less than  $2 \times 10^4$  atoms per picture) so that the error introduced by the atoms is negligible. In the future the masking strategy can be very easily adapted as described here.

## 4.5 Results

In this section we show the results of implementing the method above on a set of  $\sim 300$  empty images. Figure 4.1 (a) shows a replica of Fig. 2.5 (on an expanded scale), with the most severe artifacts (i. e. dead pixels at the bottom left and low illumination at the top and left margins) masked off. All images (and all empty images) will be masked like this before any further analysis, in order to prevent any skew from the large deviations in these regions.

We can clearly see that both  $F = 1$  and  $F = 2$  images still have artifacts in them, on the order of  $\text{OD} \sim \pm 0.05$  (where the shot noise floor should be of order  $\Delta_{SN} \text{OD} \sim \pm 0.01$ ). The main portion of these artifacts is relatively constant from illumination to illumination, and is due to very small residual drift of the imaging power during an imaging sequence and also due to some imaging light bleeding over into the ‘dark’ section of the camera chip (masking of the CCD chip described in section 2.2.1).

It is clearly seen that the main portion of these artifacts is easily subtracted out in our case by just subtracting the mean ( $\mathbf{R} = \sum_j \mathbf{R}_j / N$ ) of the empty images (see Fig. 4.1 (b)). It is important to interleave the empty images with the actual data and to have the sequence for taking an empty image deviate only minimally from the sequence of generating actual data. An example for this would be shuttering off the MOT (cycling) laser or turning off the gradient field during the MOT loading phase and then proceeding with the sequence as one would normally. This ensures that any drifts that may happen between images or during/before images remain constant for the empty images. In other words, it would be a bad idea to quickly take many several hundred images before and after data taking, since the resulting set of empty images might not have the same characteristic features as the actual data-images. The minimum number of images needed is on the order of  $\sim 100$ , which

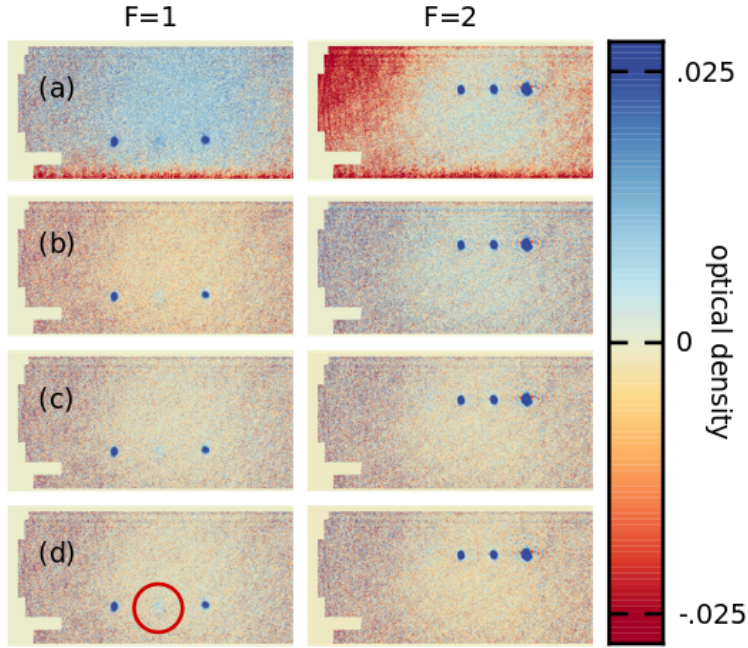


Figure 4.1: The image shown in (a) is a recreated version of Fig. 2.5 in chapter 2, with all other images being a processed version of (a). (a) Optical density images for a typical iteration of the experiment showing both  $F = 1$  and  $F = 2$  images ( $\sim 3 \times 10^4$  atoms in total). The temporal distance between reference and  $F = 2$  illumination is double compared to  $F = 1$ , hence the deviations are bigger for  $F = 2$ . (b) Optical density image after subtracting the mean empty image removing most of the artifacts. (c,d) Optical density image after subtracting the mean image and the first ten principal components where the overlaps calculated with masking (c) and without masking (d) the atom signal. The very faint signal at  $|1, 0\rangle$  (circled in (d)) corresponds to about 500 atoms.

suppresses the per pixel shot noise enough to not dominate until later principal components (30 or later).

In Fig. 4.1 (b) (especially for  $F = 2$  atoms) we can still see artifacts that are not constant due to the relatively long time interval (6 ms) between illumination and reference illumination.  $F = 1$  also still has artifacts, but they are comparable to the shot-noise level. In Figs. 4.1 (c) and (d) we see the result of subtracting the first 10 principal components with and without the atom-masking procedure described in section 4.4. In both cases, the artifacts still present in (b) are mostly removed, at least to a level well below the shot noise. The remaining artifacts seen in Fig. 4.1 (c) and (d)  $F = 2$  are probably

due to imaging the atoms either slightly out-of-focus or slightly off resonance creating the tiny ripples seen between the atom-clouds.

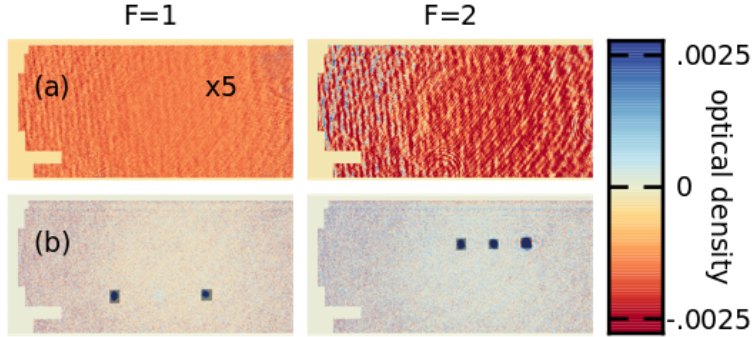


Figure 4.2: (a) Difference between the images Fig. 4.1 (c) and (d) at a magnified scale ( $\times 100$  for  $F = 1$  and  $\times 20$  for  $F = 2$ ), showing the error induced by not masking at small atom-numbers is typically negligible (shot noise is at the 0.01 level). (b) Masks used for the  $F = 1$  and  $F = 2$  atoms respectively laid over Fig. 4.1 (c).

The magnified difference between including the masking procedure and not including the masking procedure is shown in 4.2 (a), indicating that for small enough atom numbers, masking is not needed. The masks used to block the atomic signal are displayed in Fig. 4.2 (b).

The first two principal components (not the mean empty image and not the constant image, which might be considered  $-1^{\text{st}}$  and  $0^{\text{th}}$  principal component) for  $F = 1$  and  $F = 2$  are displayed in Fig. 4.3 (a) and (b), showing fringe patterns of different shapes, generally distributed over most of the image. Some fringe patterns, for example  $F = 1$  top right corner, repeat in a similar fashion, which means that they not only occur sometimes, but they potentially also shift in time slightly. Figure 4.3 (c) and (d) shows the real part of the Fourier-transform of those two principal components, showing a clear structure. Higher principal components (20 and higher) show no structure either in real space or in Fourier space, which indicates that most of the later principal components serve to emulate certain realizations of shot-noise, which is of course impossible to predict. Therefore higher principal components should in fact be excluded, since otherwise the data is ‘over-fitted’. In the case that even smaller signals need to be detected, but shot noise is a problem, averaging over different realizations of the shot noise by averaging images can lower the shot noise of the averaged image further.

Figure 4.4 illustrates the above point by displaying the average absolute

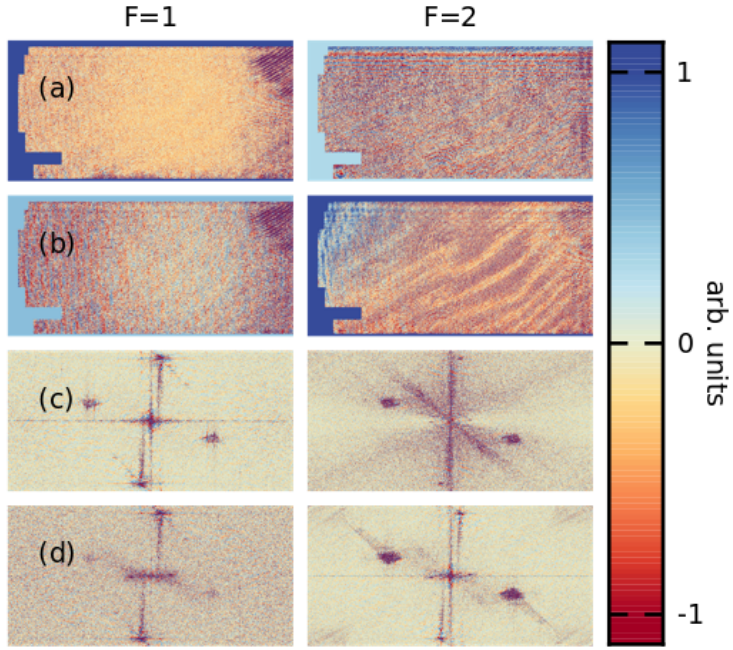


Figure 4.3: First two principal components ((a) and (b)) and the real part of their Fourier transform ((c) and (d)).

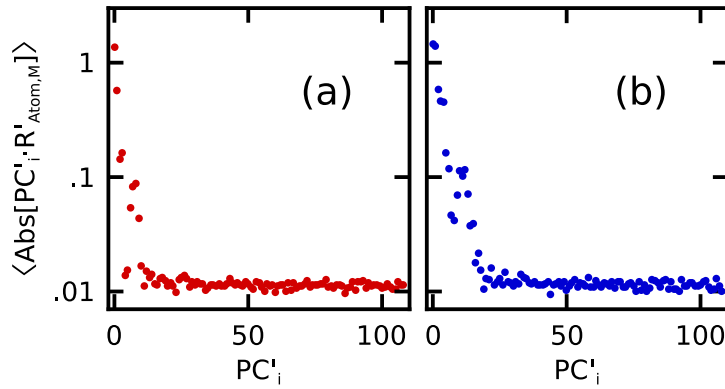


Figure 4.4: Mean absolute value of the corrected overlap between masked principal component  $i$  and image  $\mathbf{R}_{\text{Atom}, \mathbf{M}}$ , averaged over  $\sim 200$  images for  $F = 1$  (a) and  $F = 2$  (b) atoms. Overlap eventually drops off into a constant noise floor, indicating that principal components after the 20<sup>th</sup> are simply recreating shot-noise patterns, and should hence be disregarded. The zeroth principal component is the constant offset.

value of the principal component weight for each principal component up to 100, when averaged over  $\sim 200$  different absorption images with atoms. The component weights quickly decay to a level of 0.01. A conservative approach then would take only the first 5 principal components, and a more aggressive approach would use all the way up to  $\sim 20$  principal components; any more than this is only fitting to shot noise. The number of principal components that need to be used will of course depend on the specific imaging system and the environment it is placed in, but can in general be evaluated by repeating the analysis done in Fig. 4.4.

The finite average value of 0.01 to which the overlap decays to for high principal components, can be explained as follows. We want to calculate the overlap of an arbitrary principal component with shot noise. We know the first and second moments of the shot noise (i. e. the mean and variance) to be ( $N$  is the number of pixels)

$$\begin{aligned}\langle \mathbf{SN} \rangle &= \frac{1}{N} \sum_{\alpha} SN_{\alpha} = 0 \\ \langle \mathbf{SN}^2 \rangle &= \frac{1}{N} \sum_{\alpha} SN_{\alpha}^2 := \sigma_{\mathbf{SN}}^2 \approx 10^{-4}.\end{aligned}$$

We want to know the result of  $\mathbf{p}_i \cdot \mathbf{SN}$ , and since the principal components are normalized and mean centered, we also know their first and second moments:

$$\begin{aligned}\langle \mathbf{p}_i \rangle &= \frac{1}{N} \sum_{\alpha} p_{\alpha,i} = 0 \\ \langle \mathbf{p}_i^2 \rangle &= \frac{1}{N} \sum_{\alpha} p_{\alpha,i}^2 = \frac{1}{N} := \sigma_{\mathbf{p}_i}^2 \approx 5 \times 10^{-6}.\end{aligned}$$

An estimate for the overlap can be made when assuming that late principal components are also realizations of shot-noise with that are merely differently normalized:

$$\begin{aligned}\mathbf{p}_i \cdot \mathbf{SN} &= \sum_{\alpha} p_{\alpha,i} SN_{\alpha} \\ &\approx \frac{\sigma_{\mathbf{p}_i}}{\sigma_{\mathbf{SN}}} \sum_{\alpha} SN_{\alpha} SN'_{\alpha}.\end{aligned}$$

The last line calculates the correlation of two independent realizations of shot noise, which is zero on average. The expectation value of its variance

can be calculated as [189] (assuming the shot-noise is approximately Gaussian with zero mean)

$$\begin{aligned} \text{var} \left( \frac{1}{N} \sum_{\alpha} \text{SN}_{\alpha} \text{SN}_{\alpha+\beta} \right) &= \frac{\sigma_{\mathbf{SN}}^4}{N} - \frac{\sigma_{\mathbf{SN}}^4}{N^2} \approx 5 \times 10^{-14} \\ \sigma_{\text{corr}} &:= \sigma \left( \sum_{\alpha} \text{SN}_{\alpha} \text{SN}_{\alpha+\beta} \right) = \sqrt{N \sigma_{\mathbf{SN}}^4 - \sigma_{\mathbf{SN}}^4} \approx 5 \times 10^{-2}. \end{aligned}$$

The overlap can finally be estimated to be

$$\mathbf{p}_i \cdot \mathbf{SN} \approx \frac{\sigma_{\mathbf{p}_i}}{\sigma_{\mathbf{SN}}} \sigma_{\text{corr}} \approx 0.01,$$

as is also seen in Fig. 4.4.

# Chapter 5

## In-Situ Magnetometry

For our experiments with spontaneous emission discussed in chapter 7, a fine control over the magnetic field, down to the level of  $100 \mu\text{G}$ , is important. However, magnetic fields can be hard to control in the usually congested apparatus used to create a degenerate quantum gas. Here we address this issue by showing that the atomic cloud used in experiments can itself serve as a probe to determine the magnetic field. This chapter is an extended version of our publication *In situ magnetometry for experiments with atomic quantum gases*, Review of Scientific Instruments **89**, 013108 (2018) [129], with co-authors M. Stewart, A. Pazmiño, and D. Schneble. Most passages and figures are quoted verbatim from the publication, and the author of the dissertation gratefully acknowledges the contributions from his co-authors. The author of this dissertation and D. Schneble conceived of the experiment. The author took and analyzed the data with contributions from M. Stewart and A. Pazmiño. The author made the numerical simulations for Fig. 5.4. The author and D. Schneble wrote the manuscript with help from M. Stewart and A. Pazmiño.

### 5.1 Introduction

Experiments with ultracold atomic quantum gases [135] often call for the manipulation and control of the atoms' spin degree-of-freedom, including work with spinor condensates [190] or homonuclear atomic mixtures in state-selective optical potentials [92–96, 165–167] where a control of Zeeman energies to a fraction of the chemical potential (typically on the order of one kilohertz or one milligauss), may be required. With fluctuations and slow drifts of ambient laboratory magnetic fields on the order of several to tens of milligauss, achieving such a degree of control over an extended amount of time requires

dedicated field-stabilization techniques. However, in a multi-purpose BEC machine, this may be challenging given geometric constraints that can interfere with shielding or with placing magnetic-field probes sufficiently close to the atomic cloud, which is often subject to short-range, drifting stray fields from nearby vacuum hardware or optomechanical mounts. To address this problem, we have developed a simple method for direct monitoring of the magnetic field at the exact position of the atomic cloud, by employing the cloud as its own field probe, in a way that does not interfere with its originally intended use. The idea is that hyperfine ground-state Zeeman sublevels that are not used in an experimental run can be employed for a rapid, concurrent sampling of Rabi resonances, in the same run, thus making it possible to record and ‘tag on’ field information to standard absorption images, which can be used both for slow feedback control or for stable-field postselection. We emphasize that our pulsed, single-shot method, which features an accuracy of tens of microgauss and has an effective bandwidth of one kilohertz, is not meant to compete with state-of-the-art atomic magnetometers [191–196]; rather, its distinguishing feature is that it can be implemented without additional hardware and independently of geometric constraints, while featuring a performance that is competitive with that of advanced techniques for field stabilization in a dedicated apparatus [197, 198]. It can, at least in principle, be used over a wide range of magnetic fields, starting in the tens of milligauss range.

This chapter is structured as follows. Section 5.2 presents the principle and implementation of our method. Section 5.3 discusses the expected measurement accuracy as well as an experimental test based on a tagged measurement of slow Rabi oscillations on a magnetic-field sensitive transition. Section 5.4 describes an application featuring the precise characterization of a state-selective optical lattice potential via microwave spectroscopy [96].

## 5.2 Method and Implementation

### 5.2.1 Principle of Operation

The principle of the method is illustrated in Fig. 5.1 for the  $S_{1/2}(F = 1, 2)$  hyperfine ground states of  $^{87}\text{Rb}$ , which are split by 6.8 GHz. The atomic sample is located in an externally applied bias field  $B_0$  along  $z$  leading to a differential Zeeman shift  $\delta_z/2\pi = 0.7 \text{ MHz/G} \times B_0$  between neighboring  $|F, m_F\rangle$  states. Starting with all atoms in the state  $|a\rangle \equiv |F = 1, m_F = -1\rangle$ , a sequence of microwave pulses  $i$  distributes population to  $|2, 0\rangle, |2, -1\rangle, |2, -2\rangle$  ( $i=1,2,3$ ), and then via  $|2, 0\rangle$  to  $|1, 1\rangle$  ( $i = 4$ ) and further to  $|2, 1\rangle$  and  $|2, 2\rangle$

( $i = 5, 6$ ). To ensure isolated addressing of each transition, the detunings  $\delta_i$  and Rabi couplings  $\Omega_i$  are chosen to be small compared to  $\delta_z$  (by three orders of magnitude in the example discussed below), and the ordering of the individual pulses is chosen to avoid spurious addressing of near degenerate single photon transitions:  $|2, -1\rangle \leftrightarrow |1, 0\rangle \approx |2, 0\rangle \leftrightarrow |1, -1\rangle$  and  $|2, 1\rangle \leftrightarrow |1, 0\rangle \approx |2, 0\rangle \leftrightarrow |1, 1\rangle$ . Other transitions are near degenerate but magnetic dipole forbidden,  $|\Delta m_F| > 1$ .

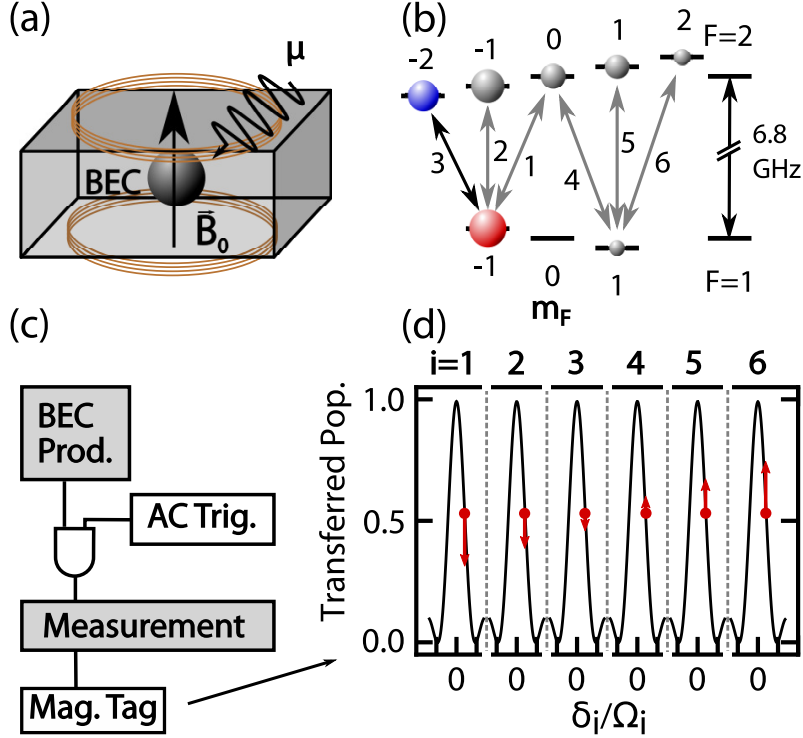


Figure 5.1: In situ magnetometry scheme. (a) A Bose-Einstein condensate of  $^{87}\text{Rb}$  atoms in a bias field  $B_0$  is subjected to a series of microwave pulses that distribute population over the  $|F, m_F\rangle$  ground state manifold, depending on the exact value of the field. (b) Relevant states for the 6-pulse sequence, the  $|1, -1\rangle$  (red) and  $|2, -2\rangle$  (blue) states are used for the measurement of Fig. 5.3. (c) Outline of a typical experimental run (gray) with the magnetic field tagging added in (white). (d) Rabi resonance for  $\Omega_i \tau_i = 0.94\pi$ , choice of detunings  $\delta_i = 0.82\Omega_i$  (at  $B_0$ ), and effects of magnetic-field changes on the transfer probabilities  $p_i$  (for identical  $\Omega_i$ ) from which the field is then reconstructed.

The pulse parameters are adjusted such that the final populations  $P_{F=2, m_F}$  expected at  $B_0$  are comparable, and that their sensitivity to small deviations

<sup>1</sup>  $\delta B$  from  $B_0$  is maximal, cf. Fig. 5.1 (d). Assuming all  $\delta_i > 0$  at  $B_0$ , the populations change away from the nominal field  $B_0$  is negative for  $i = 1, 2, 3$  and positive for  $i = 4, 5, 6$ , with each transition shifted by a different amount. The change in the set of final populations then allows for an unequivocal and precise reconstruction of  $B = B_0 + \delta B$ . In quantitative terms, the transition probabilities  $p_i$  for the individual pulses can be calculated from the relative final-state populations  $P_{F,m_F} = N(F, m_F)/N$  as

$$\begin{aligned}
p_1 &= P_{1,1} + P_{2,0} + P_{2,1} + P_{2,2} \\
p_2 &= P_{2,-1}/(P_{1,-1} + P_{2,-1} + P_{2,-2}) \\
p_3 &= P_{2,-2}/(P_{1,-1} + P_{2,-2}) \\
p_4 &= (P_{1,1} + P_{2,1} + P_{2,2})/(P_{1,1} + P_{2,0} + P_{2,1} + P_{2,2}) \\
p_5 &= P_{2,1}/(P_{1,1} + P_{2,1} + P_{2,2}) \\
p_6 &= P_{2,2}/(P_{1,1} + P_{2,2})
\end{aligned}$$

Each  $p_i$  is related to the magnitude of the magnetic field  $B$  via (see also chapter 2 section 2.2.3)

$$p_i = \left( \frac{\Omega_i}{\tilde{\Omega}_i} \right)^2 \sin^2(\tilde{\Omega}_i \frac{\tau_i}{2}), \quad (5.1)$$

where  $\tilde{\Omega}_i = (\Omega_i^2 + \delta_i^2)^{1/2}$  and  $\delta_i = \delta_i(B)$  is the modified detuning of the  $i$ th pulse from the  $i$ th addressed resonance. Assuming that the Rabi couplings  $\Omega_i$  are known from an independent calibration, the magnetic field  $B$  can then be extracted by fitting  $\hbar(\delta_i + \omega_i) = E(F_i, m_{F_i}; B) - E(F'_i, m_{F'_i}; B)$ , where  $\omega_i$  is the microwave frequency for the  $i$ th pulse, and where

$$E(F, m_F; B) = -\frac{\hbar\Delta}{8} \pm \frac{\hbar\Delta}{2} \sqrt{1 + m_F x + x^2 + g_I \mu_B m_F B} \quad (5.2)$$

is the Breit-Rabi [163] energy of the levels involved in the transition (see also chapter 2 section 2.2.4), where the  $+(-)$  sign holds for  $F=2(1)$ ,  $x = (g_I - g_s)\mu_B B/\Delta$ , with  $g_s$  the g-factor of the electron,  $\Delta = 2\pi \times 6.834\dots$  GHz and  $g_I = -9.951\dots \times 10^{-4}$  for  $^{87}\text{Rb}$  [144].

## 5.2.2 Experimental Implementation

Our experiments are performed in a magnetic transporter apparatus [134] (see also chapter 2 section 2.1.5), with an optically trapped condensate of  $N \sim$

---

<sup>1</sup>For  $\delta B \ll B_0$ , fluctuations perpendicular to  $z$  can be neglected, since they are quadratically suppressed.

$1 \times 10^5$  atoms in the  $|a\rangle \equiv |1, -1\rangle$  ground state. At the end of an experimental run (which usually contains steps for the manipulation of the motional and/or internal state of the atoms), the atoms are released, given about 1 ms to expand (to avoid interaction effects), then subjected to the magnetometry pulse sequence described above, and subsequently detected using absorption imaging. For the determination of the state populations  $P_{F,m_F}$  we use Stern-Gerlach separation (see chapter 2 section 2.2.1). In addition, to distinguish the  $F = 1, 2$  states with  $|m_F| = 1$  (note that the  $g_F$  factors in  $^{87}\text{Rb}$  have the same magnitude), absorption imaging of the  $F = 2$  states is first performed using resonant  $F = 2 \rightarrow F' = 3$  light, which disperses the  $F=2$  atoms while the  $F = 1$  atoms continue their free fall. After optical pumping of the  $F = 1$  atoms to  $F = 2$  (using  $F = 1 \rightarrow F' = 2$  light) these atoms are then imaged as well.

Several considerations determine the optimum choice of parameters for the magnetometry pulse sequence. Maximizing the magnetic-field sensitivity of the  $p_i$  (see Eq. 5.1) for a fixed coupling  $\Omega_i$  yields optimum detunings  $\delta_i \approx 0.58\Omega_i$  (at  $B_0$ ) and pulse durations  $\tau_i \approx 1.24\pi\Omega_i^{-1}$  (the pulse area should be kept below  $3\pi/2$  in order to avoid sidelobes as high as the main lobe in the Rabi spectrum). Additional minimization of the sensitivity to possible fluctuations of  $\Omega_i$  (with microwave amplifiers typically specified only to within 1 dB) modifies these conditions to  $\delta_i \approx 0.82\Omega_i$  and  $\tau_i \approx 0.94\pi\Omega_i^{-1}$ , respectively. Ideally, the chosen coupling strength  $\Omega_i$  of each transition should be proportional to the differential magnetic moment  $\Delta\mu_i = \partial_B E(F_i, m_{F_i}; B) - \partial_B E(F'_i, m_{F'_i}; B)$  of the two states involved in the transition. Furthermore, the expected range  $\delta B$  of fluctuations around  $B_0$  sets the optimum choice of  $\Omega_i$  through  $\delta B \sim \hbar\Omega_i/\mu_B$ , and, in turn, the accuracy of the measurement goes down with increasing  $\Omega_i$ . In our experiment, we can comfortably realize kHz-range microwave couplings on all transitions (which are independently calibrated from sampling single Rabi resonances).

To demonstrate our method, we applied a bias field of 5.9 G using a pair of Helmholtz coils with 10 ppm current stabilization. Figure 5.2 shows the results of a typical short-time measurement of the magnetic field along the bias field direction, using an AC-line trigger to start the pulse sequence (see appendix C.1). The dominant contribution to field fluctuations around  $B_0$  is seen to be ambient AC-line noise with an amplitude around 1 mG, containing the first few harmonics of 60 Hz. From here on, we compensate for this by feeding forward the sign-reversed fit function onto an identical secondary coil of a single winding. The subtraction of the fit results in residual fluctuations up to  $\pm 0.4$  mG, without apparent phase relationship with the AC-line.

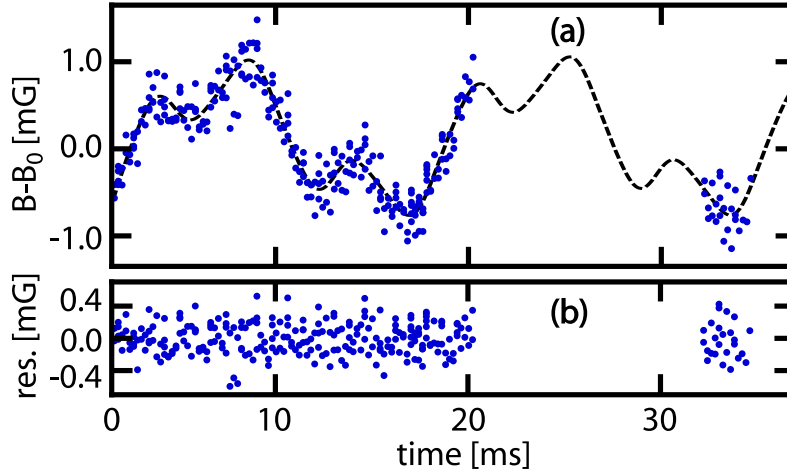


Figure 5.2: Measurement of magnetic-field fluctuations (at  $B_0 = 5.9$  G), referenced to an AC-line trigger with a variable delay. (a) Reconstructed field noise, as a function of time after an AC-line trigger. The solid line is a fit function  $a \cos(\omega_{AC}t + \phi_1) + b \cos(3\omega_{AC}t + \phi_3) + c \cos(5\omega_{AC}t + \phi_5)t$ , with  $\omega_{AC} = 2\pi \times 60$  Hz. (b) Residual field variation after subtracting the fit function.

## 5.3 Characterization of Performance

### 5.3.1 Slow Rabi Cycling

We characterize the remaining fluctuations further, and in particular determine whether they represent the actual magnetic field in a time interval close to the measurement. For this purpose we implement slow Rabi cycling (at  $B_0 = 9.045$  G) on the maximally magnetic-field sensitive transition  $|a\rangle \equiv |1, -1\rangle \leftrightarrow |b\rangle \equiv |2, -2\rangle$ , with a differential magnetic moment of  $\Delta\mu_3 = 2\pi \times 2.1$  kHz/mG. This measurement is performed by varying the coupling time of the oscillation and then recording the number of atoms in  $|b\rangle$ . To accommodate the Rabi cycling measurement, we choose a truncated pulse sequence in which the population in  $|a\rangle$  is subsequently distributed over five transitions instead of six. We note that this experiment is an example for the mode of operation depicted in Fig. 5.1(a), in which a ‘measurement’ (of the Rabi cycling) is followed by a magnetic field ‘tag’. Magnetic-field fluctuations will lead to a rapid dephasing of the Rabi oscillation. However, using the field tag, the effect of (slow) magnetic-field fluctuations on the oscillation can be eliminated.

For a well-resolved, single-cycle oscillation, the instability of the detuning

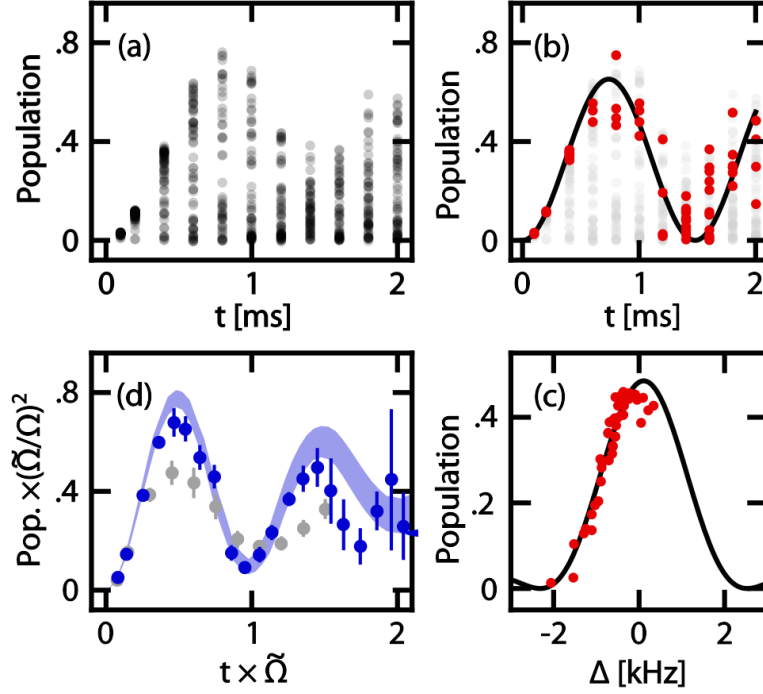


Figure 5.3: Slow Rabi cycling between  $|a\rangle = |1, -1\rangle$  and  $|b\rangle = |2, -2\rangle$ , with magnetic-field reconstruction based on a 5-pulse sequence. (a) Observed time-dependence of the transferred population after eliminating AC-line fluctuations as demonstrated in Fig. 5.2. The large shot-to-shot scatter is due to residual field fluctuations. (b) Data points post-selected to be within a  $100 \mu\text{G}$ -window. A clear oscillation is recovered, that only dephases after the first cycle. The line is the expected oscillation. (c) Population at a constant time of  $400 \mu\text{s}$  vs. the measured field tag. The solid line is a Rabi resonance fit with the pulse time and Rabi frequency fixed to expectation. (d) Scaled population vs. scaled time. Gray points are original data scaled by average detuning. The shaded line is a simulation, with  $B_0$  known to within  $55 \mu\text{G}$ , and  $\Omega$  known to within 1 dB (see text).

should not exceed about one tenth of the Rabi frequency. Here we choose  $\Omega = 2\pi \times 0.61(3) \text{ kHz}$ , at an average detuning of  $\delta = 2\pi \times 0.44(3) \text{ kHz}$ .

We see that the raw data resulting from multiple repetitions of the Rabi oscillation experiment has large associated scatter due to the long term drifts and shot-to-shot jitter of the magnetic field. To demonstrate the effect of the field tag, we plot the oscillation both as a function of inferred detuning (at a fixed duration) and time (at a fixed detuning). The results are shown in

Fig. 5.3 (b,c). In addition, we also plot all data, as scaled population  $p\tilde{\Omega}^2/\Omega^2$  vs. scaled time  $t\tilde{\Omega}$ . Clearly, the field tagging leads to a marked improvement of the oscillation contrast.

The next section, 5.3.2, will give the details of a simulation of the exact behavior of the field reconstruction. For the given example, and for the parameters of the five-pulse sequence used, we expect the reconstructed fields to scatter around the true magnetic field value with a 55  $\mu\text{G}$  standard-deviation. The simulation and data agree very well, with a slight deviation at late times, potentially due to imperfect cancellation of the AC-line or higher-frequency noise that is uncorrelated with the AC-line.

In our measurements, the high degree of correlation between the transferred population and the detected magnetic field further confirms that the residual fluctuations occur on a scale that is long compared to the duration of the Rabi cycle preceding the field measurement (cf. Fig. 5.3). We note that on long time scales, the observed magnetic field drifts are typically on the order of one to several milligauss, over the course of one hour.

### 5.3.2 Theoretical Accuracy & Operation Range

For the Rabi oscillation measurements described in section 5.3.1, the parameters of the magnetometry pulse sequence  $i = (1, 2, 4, 5, 6)$  were  $\Omega_i/2\pi = (2.3, 1.6, 2.6, 2.0, 2.7)$  kHz,  $\tau_i = (150, 150, 150, 200, 120)$   $\mu\text{s}$  and  $\delta_i/2\pi = (1.8, 2.8, 2.0, 2.1, 3.4)$  kHz, which yielded an inferred accuracy of 55  $\mu\text{G}$ . To estimate the ultimate resolution and limits of our magnetometer for optimal parameters (see section 5.2.2), we perform a Monte-Carlo simulation, using a six-transition sequence. We start with a set of fixed (true) fields  $B_{tr}$  drawn from a Gaussian distribution around  $B_0$  that are supposed to be reconstructed. The number of atoms transferred in the  $i$ th pulse at fixed  $p_i$  is drawn from a binomial distribution, while the transfer probabilities  $p_i$  themselves are subject to uniformly distributed fluctuations of  $\tau_i$  ( $\pm 2$   $\mu\text{s}$ ),  $\Omega_i$  ( $\pm 1$  dB),  $\delta_i$  ( $\pm 2\pi \times 7$  Hz) and the instantaneous magnetic field during each individual pulse due to uncanceled residual fluctuations ( $\pm 100$   $\mu\text{G}$ ). The Rabi frequencies are  $\Omega_i/2\pi = (0.9, 1.9, 3.1, 1.2, 1.9, 3.1)$  kHz and the optimized detunings and pulse areas are  $\delta_i = 0.82\Omega_i$  and  $\tau_i\Omega_i = 0.94\pi$  as mentioned earlier.

Results of the simulation are shown in Fig. 5.4. For the optimum pulse parameters, the reconstruction of  $B_{tr}$  is accurate to within a standard deviation of 25  $\mu\text{G}$ . A reconstruction is consistently possible within a  $\pm 500$   $\mu\text{G}$  window around  $B_0$ , if outliers with large fit uncertainties are removed. For larger distances from  $B_0$ , the default detunings  $\delta_i$  can be readjusted, or alternatively, larger Rabi couplings can be used, at the (inversely proportional) expense of

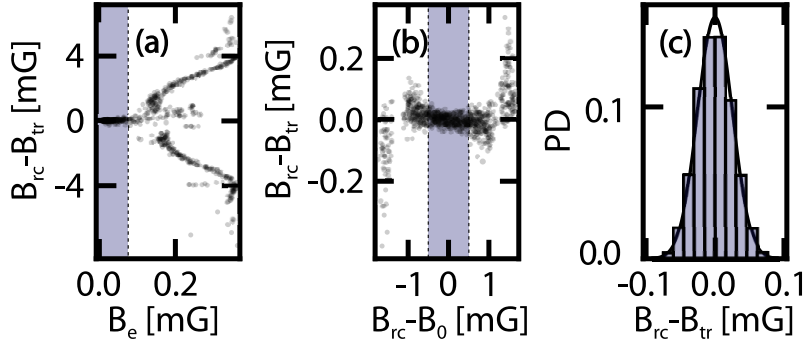


Figure 5.4: Simulated field reconstruction (over  $10^4$  runs). (a) Reconstruction error vs. fit uncertainty  $B_e$ , with convergence in the shaded area  $B_e < 80 \mu\text{G}$ . (b) Reconstruction error vs. distance of  $B_{rc}$  from  $B_0$ , after discarding fits with  $B_e > 80 \mu\text{G}$ . Proper convergence is obtained in a  $\pm 500 \mu\text{G}$  window. (c) Histogram of reconstruction errors for the data in the gray shaded areas (a,b). The solid curve is a Gaussian with a  $\sigma$  of  $25 \mu\text{G}$ .

the accuracy of the field reconstruction. The results of the simulation confirm that most of the apparent remaining fluctuations in Fig. 5.2 are actual fluctuations of the ambient magnetic field, at least to within the reconstruction uncertainty ( $\pm 100 \mu\text{G}$  for the pulse parameters chosen in that experiment).

## 5.4 Application: Spectroscopy of State - Selective Optical Lattices

A number of experimental applications involve the use of homonuclear mixtures of alkali atoms in state-selective optical lattice potentials [92–96, 165, 166, 199], which rely on the existence of a differential Zeeman shift between the states involved. In certain cases, a highly stable separation between a deeply lattice-bound state and a less deeply bound or free state may be desired, such as when the states are subject to coherent coupling [124, 200, 201], requiring precise control of both the lattice depth and the magnetic field.

Figure 5.5 (a) shows an experimental configuration in which we prepared an ‘untrapped’ ensemble of atoms in state  $|b\rangle = |2, 0\rangle$ , coupled to a state  $|r\rangle = |1, -1\rangle$  that is confined to the sites of a deep, blue-detuned lattice potential with a zero-point energy shift  $h\nu_{ho}/2 = h \times 20(1)$  kHz, generated with circularly polarized light from a titanium-sapphire laser (see section 2.2.5 for details).

To stabilize the magnetic field, we utilize post-selection down to the 100 Hz

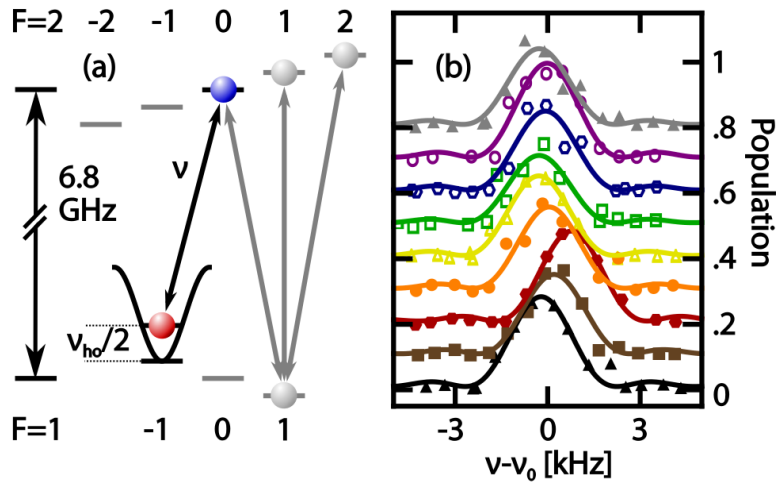


Figure 5.5: Microwave spectroscopy of a free-to-bound transition in a state-selective optical lattice potential (wavelength 790.10(2) nm,  $\sigma^-$  polarization). (a) Population is transferred from the untrapped state  $|b\rangle = |2, 0\rangle$  to the confined state  $|r\rangle = |1, -1\rangle$ . The gray lines indicate the magnetometry sequence following the transfer. (b) Bound-state population after a 400  $\mu$ s long pulse with  $\Omega = 2\pi \times 450(1)$  Hz and variable detuning, and after accounting for magnetic-field fluctuations. The sequence of spectra was taken at regular intervals over the course of one hour.

level based on the magnetic-field tagging described above, using parameters similar to those in Fig. 5.4. The optical intensity  $I$  is stabilized to  $\sim 1\%$  using a photodiode and a PID regulation circuit, yielding a transition frequency that should be stable to within about 100 Hz (since  $\omega_{ho} \propto \sqrt{I}$ ). However, this does not eliminate the possibility of slow drifts of the lattice depth (such as due to temperature induced birefringence or small wavelength changes of the laser) in the course of an experiment, as can be seen in Fig. 5.5 (b). To address these issues, the precise resonance condition can now be monitored throughout data taking, using our method. The range of the drift is several hundreds of Hz. We emphasize that the spectroscopic precision necessary for this kind of experiment would not be attainable without canceling AC-line induced magnetic field noise and compensating the shot-to-shot fluctuations using the magnetic field tag.

## 5.5 Conclusions

In conclusion, we have demonstrated a simple method for in-situ monitoring of magnetic fields in quantum gas experiments with alkali atoms, with a demonstrated accuracy of  $55 \mu\text{G}$ , an inferred accuracy of  $25 \mu\text{G}$  for optimized parameters, and a time resolution of 1 ms. This is a very notable improvement over magnetic field stability in the past which was on the order of 5 mG of drift per day and up to 10 mG due to AC-fluctuations of the magnetic field. As already seen for the examples above, the magnetometry pulse sequence can be tagged onto experiments that potentially involve several hyperfine states. In principle, the number of transitions used for magnetometry can be reduced down to two, as long as they move differently for a change of the magnetic field (this can be achieved by having two detunings of opposite sign or differential magnetic moments of opposite sign). For example, the method could work using only transitions 1 and 4 of Fig. 5.1 (b). Using a smaller number of transitions generally degrades the accuracy (here by a factor  $\sim \sqrt{3}$  when all pulse parameters are left constant, compared to using six transitions), but it increases the measurement bandwidth (here by a factor of 3), which could be an important independent consideration for certain applications.

Thus far, we have only described the use of this method as a scalar magnetometer (in order to be able to ignore fluctuations in perpendicular directions). It should also be possible to access fluctuations of the ambient field in more than one spatial direction, if the bias field is rotated during the magnetometry pulse sequence (with two transitions used per direction). This can become important if one wants to use this method for stable field post-selection at low fields.

Finally, for comparison to other magnetometry techniques, a sensitivity may be specified as [202]  $\eta = \Delta B_{min} \sqrt{T}$ , i.e. as the minimum detectable change in field  $\Delta B_{min} = 2\sqrt{\ln 2} \sigma \sim 60 \mu\text{G}$  multiplied by the square root of the cycle time. Since typical field fluctuations in laboratories usually stem from AC-mains or are very low frequency (such as fluctuations of Earth's magnetic field), synchronizing the experiment to the AC-line can yield one measurement in the effective integration time of 1 ms. In this case, an effective sensitivity  $\eta \sim 300 \text{ pT}/\sqrt{\text{Hz}}$  (in a measurement volume of  $10 \mu\text{m}^3$ ) can be reached.

In comparison, other stabilization methods typically use fluxgate magnetometers [198] and large volume Helmholtz coils ( $1 \text{ m}^3$ ). The bandwidth of the fluxgate magnetometers is on the order of 1 – 5 kHz [203].

# Chapter 6

## Review of the Weisskopf-Wigner Model

The description of spontaneous emission of photons from an excited atom, as described by Weisskopf and Wigner [100] on the basis of Dirac's radiation theory [204], is a fundamental concept in quantum electro-dynamics. In this chapter we will give a brief overview of the Weisskopf-Wigner model in order to discuss results used in chapter 7.

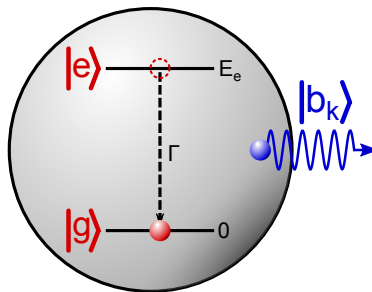


Figure 6.1: Spontaneous Emission. A two-level atom initially prepared in the excited state  $|e\rangle$  at energy  $E_e$  undergoes decay to the ground state  $|g\rangle$  at rate  $\Gamma$  under emission of a photon  $|b_k\rangle$  at wavenumber  $k$  and momentum  $\hbar k$ .

### 6.1 Electric Dipole Hamiltonian

We want to consider the interaction of a single atom with the quantized electromagnetic vacuum. To that end, we will first start with the Hamiltonian of

a particle in a classical monochromatic electromagnetic field [2]

$$\hat{H} = \frac{\left(\hat{\vec{p}} - q\vec{A}\right)^2}{2m} + V(\hat{\vec{r}})$$

where  $q$  is the charge of the particle, and  $V$  is the potential, and  $\vec{A}$  is the vector potential. Note that we have neglected the energy in the electromagnetic field in the above equation. In our case, we consider the electron in the electric field of a nucleus, so  $q = -e$ , where  $e$  is the elementary charge. Expanding the square yields

$$\hat{H} = \hat{H}_0 + \frac{e\hat{\vec{p}} \cdot \vec{A} + e\vec{A} \cdot \hat{\vec{p}} + e^2\vec{A}^2}{2m}$$

where  $\hat{H}_0 = \hat{\vec{p}}^2/2m + V(\hat{\vec{r}})$  is the Hamiltonian without field. We will neglect the last term for since it is negligible for small fields, and we will choose the Coulomb gauge ( $\nabla \cdot \vec{A} = 0$ , transverse waves) so that we can write:

$$\hat{H} = \hat{H}_0 + \frac{e}{m}\vec{A} \cdot \hat{\vec{p}}.$$

We make the following ansatz for the vector potential:

$$\begin{aligned}\vec{A} &= \vec{A}_0 \cos(\vec{k} \cdot \vec{r} - \omega t) \\ &\approx \vec{A}_0 \sin(\omega t)\end{aligned}$$

where  $\omega$  is the frequency of the electromagnetic field and we have made the dipole approximation ( $\vec{k} \cdot \vec{r} \approx 0$ , i. e. the spatial variation of the electric field is negligible over the size of the atom) in the second line of the last equation. The electric field at the place of the atom is then

$$\vec{E} = i\vec{A}_0\omega \sin(\omega t) = \vec{\varepsilon}\mathcal{E}_0 \sin(\omega t),$$

where  $\mathcal{E}_0$  is the magnitude of the electric field and  $\vec{\varepsilon}$  is its polarization. We arrive at:

$$\hat{H} = \hat{H}_0 + \frac{e}{m\omega} \left(\vec{\varepsilon} \cdot \hat{\vec{p}}\right) \mathcal{E}_0 \sin(\omega t) = \hat{H}_0 + \hat{H}'.$$

Using the relation  $\hat{\vec{p}} = m \left[\hat{\vec{r}}, \hat{H}_0\right] / i\hbar$ , we can evaluate the transition matrix elements of  $\hat{H}'$  to

$$\hat{H}'_{j,k} = -i\frac{\omega_{j,k}}{\omega} \langle j | \vec{\varepsilon} \cdot (-e)\hat{\vec{r}} | k \rangle \mathcal{E}_0 \sin(\omega t) \approx -i\langle j | \vec{\varepsilon} \cdot \hat{\vec{d}} | k \rangle \mathcal{E}_0 \sin(\omega t)$$

where  $\hat{\vec{d}} = -e\hat{\vec{r}}$  is the dipole operator, and we have assumed that the radiation used is near resonant with the energy difference between state  $|j\rangle$  and state  $|k\rangle$ .

## 6.2 Field Quantization and Weisskopf–Wigner Hamiltonian

Now we quantize the electromagnetic field [102, 205], which, in the dipole approximation, yields the following expression for the electric field at frequency  $\omega$  and with polarization  $\vec{\varepsilon}$ :

$$\hat{\mathcal{E}}_\omega = \sqrt{\frac{\hbar\omega}{2\varepsilon_0 V}} \left( \hat{b}_\omega \vec{\varepsilon} e^{i\omega t} + \hat{b}_\omega^\dagger \vec{\varepsilon} e^{-i\omega t} \right),$$

where  $V$  is the volume of space and  $\varepsilon_0$  is the vacuum permittivity and we have again used the dipole approximation in the second line. The operator  $\hat{b}_\omega^\dagger$  ( $\hat{b}_\omega$ ) creates (annihilates) a single excitation (photon) of the electromagnetic field at frequency  $\omega$  with the polarization  $\vec{\varepsilon}$ . The energy of the quantized electromagnetic field at of frequency  $\omega$  is  $\hat{H}_{\text{field}} = \hbar\omega(\hat{n} + 1/2)$  where  $\hat{n}$  is the number of excitations (i. e. photons) in the field. We can simply insert the quantized form of the electric field into the above Hamiltonian. If we assume the unperturbed Hamiltonian  $\hat{H}_0$  to be that of a two-level atom with ground state  $|g\rangle$ , excited state  $|e\rangle$ , and excited state energy  $\hbar\omega_{eg}$ , we arrive at the Hamiltonian of a two level atom in the quantized electromagnetic vacuum: [102, 205]:

$$\begin{aligned} \hat{H} \approx & \hbar\omega_{eg}|e\rangle\langle e| + \sum_{\vec{k}, s} \hbar\omega_k \left( \hat{b}_{k,s}^\dagger \hat{b}_{k,s} + \frac{1}{2} \right) \\ & + \sum_{\vec{k}, s} \left( -i\sqrt{\frac{\hbar\omega_k}{2\varepsilon_0 V}} \vec{\varepsilon}_{\vec{k}, s} \cdot \langle g|\hat{d}|e\rangle \hat{b}_{k,s}^\dagger |g\rangle\langle e| + h.c. \right), \end{aligned}$$

$\vec{\varepsilon}_{\vec{k}, s}$  is the polarization vector of the light,  $\omega_k$  is the frequency of the light and  $s$  is one of the two possible polarization states (e. g. linear horizontal and linear vertical). Since we do not externally apply a field in this case, but are rather considering the quantized zero-point fields of the quantum-electrodynamic vacuum, we have to sum over all modes which are allowed in the volume  $V$  in our physical space. The operator  $\hat{b}_{\vec{k}, s}^\dagger$  creates a photon of polarization  $s$  and wavevector  $\vec{k}$ . Note that the time-dependence of the electric fields  $e^{-i\omega t}$  was shifted into the states rather than the Hamiltonian (see also Eq. 6.1).

### 6.3 Decay Rate and Lamb Shift

To solve the dynamics of the Weisskopf-Wigner model, we first make an ansatz for the wavefunction, by assuming the system is in a superposition state of being either a not decayed atom ( $|e\rangle$ ) and no photons in the radiation field or a decayed atom ( $|g\rangle$ ) with one photon in the radiation field [206]:

$$|\Psi\rangle = A(t)e^{-i\omega_{eg}t}|e, 0\rangle + \sum_{\vec{k}, s} e^{i\omega_k t} B_{\vec{k}, s}(t)|g, 1_{\vec{k}, s}\rangle, \quad (6.1)$$

which can be inserted into the Schrödinger equation  $i\hbar\partial_t|\Psi\rangle = \hat{H}|\Psi\rangle$  to get the set of coupled equations:

$$\begin{aligned} \partial_t A(t) &= i \sum_{\vec{k}, s} g_{\vec{k}, s}^* e^{-i(\omega_k - \omega_{eg})t} B_{\vec{k}, s} \\ \partial_t B_{\vec{k}, s} &= i g_{\vec{k}, s} e^{i(\omega_k - \omega_{eg})t} A(t) \\ g_{\vec{k}, s} &= i \sqrt{\frac{\hbar\omega_k}{2\varepsilon_0 V}} \vec{\varepsilon}_{\vec{k}, s} \cdot \langle g | \vec{d} | e \rangle. \end{aligned}$$

Formal integration of the second equation can then be inserted into the first differential equation, which yields a decoupled integro-differential equation:

$$\partial_t A(t) = - \sum_{\vec{k}, s} |g_{\vec{k}, s}|^2 \int_0^t dt' e^{-i(\omega_k - \omega_{eg})(t-t')} A(t'). \quad (6.2)$$

At this point no formal/closed solution can be found; however, with certain assumptions, one can arrive at good approximate expression for  $A(t)$ . The most famous is the Markovian or Weisskopf-Wigner approximation, for which we identify two timescales for dynamics in the system: (1) phase evolution ( $\partial_t \arg(A(t))$ ), and (2) amplitude evolution ( $\partial_t |A(t)|$ ). If the amplitude evolution is much slower than the phase evolution, which in this case implies  $\omega_0 \gg |g_k|^2$ , then we can approximately evaluate the integral in the integro-differential equation as ( $A(t) \approx A(t')$ ):

$$\int_0^t dt' e^{-i(\omega_k - \omega_{eg})(t-t')} A(t') \approx A(t) \int_0^\infty dt' e^{-i(\omega_k - \omega_{eg})(t-t')}$$

With the above approximation Eq. 6.2 is now reduced to an ordinary first order differential equation, with the only challenge being the evaluation of the

following integral (we have taken the continuum limit, which transforms the summation over momentum states to an integration over momentum states):

$$\sum_s \int d^3\vec{k} \left| g_{\vec{k},s} \right|^2 \int_0^\infty dt' e^{-i(\omega_k - \omega_{eg})(t-t')} := \frac{\Gamma}{2} - i\delta_L.$$

A detailed version of how to evaluate this integral is shown for 3D in [102] or [206]. We thus arrive at the differential equation:

$$\partial_t A(t) \approx -A(t) \left( \frac{\Gamma}{2} - i\delta_L \right)$$

where the real part of the integral represents the spontaneous decay rate and the imaginary part of the integral represents the Lamb shift. The Lamb shift, i. e. the change of the resonance frequency of the atom induced by the zero point electromagnetic field oscillations, is similar to the shift in resonance frequency of a classical pendulum when introducing a damping term. The spontaneous emission rate  $\Gamma$  evaluates to [102, 205]:

$$\Gamma = \frac{\omega_{eg}^3}{3\pi\epsilon_0\hbar c^3} \left| \langle g | \vec{d} | e \rangle \right|^2,$$

and the Lamb shift evaluates to [206]

$$\delta_L = \frac{\Gamma}{2\pi\omega_{eg}^3} \mathcal{P} \left( \int_0^\infty d\omega_k \frac{\omega_k^3}{\omega_k - \omega_{eg}} \right).$$

Here  $\mathcal{P}$  denotes the Cauchy principal value of an integral, and  $m_e$  is the electron mass. The integral diverges, a problem which can be solved e. g. by mass-renormalization of the electron, as done by Bethe [207].

The Markovian approximation breaks down whenever the excited state energy is not much larger than the inverse lifetime (linewidth  $\Gamma$ ). However, for a typical atomic optical decay, the linewidth is many orders of magnitude smaller than the transition frequency ( $\Gamma \sim 2\pi \times 10^7$  Hz vs.  $\omega_{eg} \sim 2\pi \times 10^{15}$  Hz), so that the Markovian approximation is well satisfied. As we will see, this is not the case for decay in photonic bandgap materials.

# Chapter 7

## Spontaneous Emission of Matter Waves from a Tunable Open Quantum System

This chapter is an extended version of our publication *Spontaneous Emission in a Matter-Wave Open Quantum System*, arXiv:1712.07791 (2017) [208], and its revision *Spontaneous emission of matter waves from a tunable open quantum system*, Nature **559**, 589 (2018) [209], with co-authors M. Stewart, A. Pazmiño, J. Kwon, and D. Schneble. Most passages and figures are quoted verbatim from the publication, and the author of this dissertation gratefully acknowledges the contributions from his co-authors. Additional sections and figures will be marked with an asterisk (\*) above the section heading or figure caption respectively. D. Schneble, the author of this dissertation, and M. Stewart conceived the experiment. The author took the measurements with assistance from A. Pazmiño and J. Kwon. The author analyzed the data with contributions from M. Stewart. Numerical simulations were performed by the author. D. Schneble supervised the project. The results were discussed and interpreted by all co-authors. The manuscript was written by the author and D. Schneble with contributions from A. Pazmiño, J. Kwon and M. Stewart.

### 7.1 Introduction

The decay of an excited atom undergoing spontaneous photon emission into the fluctuating quantum-electrodynamic vacuum provides an emblematic example for the dynamics of an open quantum system. Recent experiments have demonstrated that the gapped photon dispersion in periodic structures

can give rise to novel spontaneous decay behavior including the formation of bound states [116, 121, 122]. So far, these effects have been restricted to the optical domain. Here, we experimentally demonstrate similar behavior in a system of elementary emitters, realized with ultracold atoms in an optical lattice, that decay by emitting matter-wave, rather than optical, radiation into free space. By controlling vacuum coupling and excitation energy, we directly observe exponential and partly reversible, non-Markovian dynamics and detect a tunable bound state containing evanescent matter waves for emission at negative excitation energies. Our system provides a flexible platform for the emulation of open-system quantum-electrodynamics and studies of dissipative many-body physics with ultracold atoms [124–126].

The Weisskopf-Wigner model of spontaneous emission [100, 205] is a central concept in quantum optics [102], describing how an excited atom can decay to its ground state due to coupling to zero-point oscillations of the electromagnetic vacuum. It simultaneously represents one of the first open quantum systems discussed in the literature, and it is an area of research that has recently seen a resurgence of intense theoretical effort [99, 127, 210, 211]. In its usual Markovian formulation, the model makes the assumption that the decay proceeds on a much slower time scale than the optical period, which leads to a memoryless, exponential decay of the excited-state amplitude and to an associated Lamb-shift of the transition frequency. For free-space photon emission, the Markovian approximation is generally fulfilled to high accuracy.

On the other hand, modifications to the mode density of the vacuum can change the features of spontaneous decay. This was first recognized in the 1940s [101] and again decades later [106] in the development of cavity quantum electrodynamics [212–214], where the decay can be altered to the extreme point of coherent vacuum Rabi oscillations when the spectrum is restricted to a single mode. Between these two limits lies the regime of a vacuum with a bounded continuous spectrum, in which a strong modification of spontaneous decay behavior occurs close to the boundary. An example is given by photonic crystals (also called photonic bandgap materials) [104, 105], where a periodic spatial modulation of the refractive index gives rise to a gapped dispersion relation. For emission close to a bandgap, the Markovian approximation can no longer be made, and novel features appear including oscillatory decay dynamics for energies above the band edge and the formation of atom-photon bound states below [215]. Over the past two decades, experiments on spontaneous emission in photonic bandgap materials, including the microwave domain, have observed some of these effects, specifically, modified spontaneous emission rates [109, 113] and Lamb shifts [117], as well as spectral signatures for non-exponential decay [116]. Very recently, experiments have probed the

long-predicted bound state [103, 216], using both transmon qubits coupled to corrugated microwave guides [122], and atoms in photonic-crystal waveguides [121] with the prospect of engineering systems with optical long-range interactions [217].

Here, we realize an atom-optical analog [124–126] of emission in a one-dimensional photonic bandgap material, where the singularity in the mode density near the edge of the continuum leads to particularly strong deviations from Markovian behavior. In our system of matter-wave emitters, the free tunability of the excitation energy and decay strength allows for a systematic exploration of the emergence of non-Markovian dynamics, including partial reversibility and the formation of a matter-wave bound state which can be directly detected. Importantly, the close spacing of emitters gives rise to collectively enhanced dynamics beyond the Weisskopf-Wigner model.

## 7.2 Introduction to the System

The experimental configuration is shown in Fig. 7.1(a). Using a deep three-dimensional optical lattice with state-selectivity along one axis, we prepare a sparse array of atoms confined to sites that are embedded in a system of isolated tubes acting as one-dimensional waveguides (see section 7.6 for details). An atom’s internal state ( $|r\rangle$ , red) is coherently coupled to a second, unconfined internal state ( $|b\rangle$ , blue) using an oscillatory magnetic field. Each site thus acts as a two-level matter-wave emitter, with harmonic-oscillator ground state occupational levels  $|g\rangle$  (empty) and  $|e\rangle$  (full), supporting both the emission (for  $|e\rangle \rightarrow |g\rangle$ ) or absorption (for  $|g\rangle \rightarrow |e\rangle$ ) of a  $|b\rangle$  atom. The excitation energy of the emitter, which is given by the detuning  $\Delta$  of the coherent coupling from the atomic resonance, is converted into kinetic energy for atomic motion along the axis of the waveguide.

One of the main features of each matter-wave emitter is its ability to undergo spontaneous decay as understood by Weisskopf and Wigner. Assuming no lattice potential, the driven atom performs simple Rabi oscillations between two internal states  $|r\rangle$  and  $|b\rangle$  described by the Hamiltonian

$$\hat{H} = (\hbar\Omega/2)e^{i\delta t}\hat{r}\hat{b}^\dagger + \text{H.c.}, \quad (7.1)$$

where  $\Omega$  denotes the strength and  $\delta$  the detuning of the coupling from the transition. The tight confinement of just one of the states (say  $|r\rangle$ ) strongly couples the atom’s internal and motional degrees of freedom, producing a zero-point energy shift  $\bar{\varepsilon}_0 = \hbar\omega_0/2 \gg \hbar\Omega$  in the potential, as well as a kinetic-energy shift  $\varepsilon_k = \hbar^2k^2/2m$  for motion of the free  $|b\rangle$  state at  $\hbar k$  momentum.

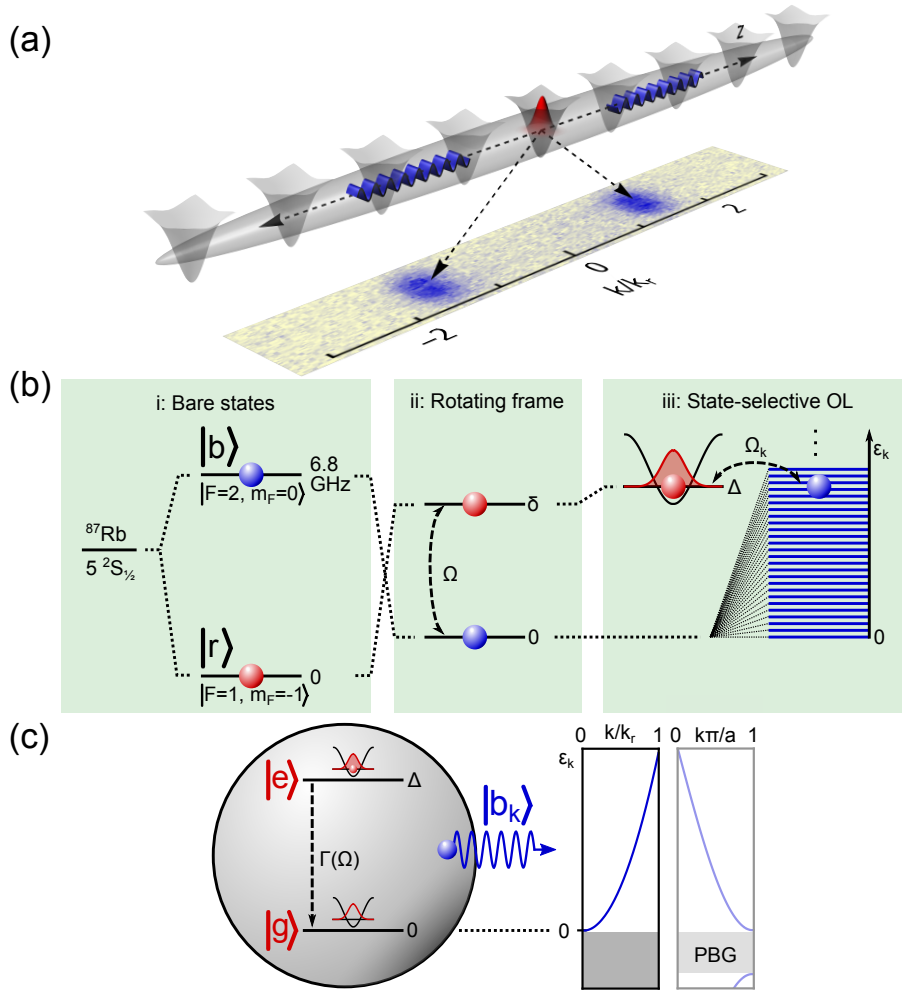


Figure 7.1: Realization of matter-wave emitters. (a) Experimental configuration: An occupied site of an optical lattice embedded in a single-mode matter waveguide acts as an elementary emitter of a single atom; adjacent empty lattice sites act as absorbers. The bottom panel shows a momentum distribution in the waveguide, observed after release and free expansion, where  $\hbar k_r = \hbar 2\pi/\lambda_z$  (with  $\lambda_z = 790.1$  nm) is the recoil momentum. (b) Emission mechanism: (i) Bare internal-state pair  $|r\rangle$  and  $|b\rangle$  in  $^{87}\text{Rb}$ ; (ii) state pair in a frame co-rotating with a 6.8 GHz microwave field (variable detuning  $\delta$  and coupling strength  $\Omega$ ), and (iii) in the co-rotating frame after applying the state-selective potential of the lattice (detuning shifted to  $\Delta = \delta + \epsilon_0/2$ , where  $\epsilon_0 = \hbar \times 40$  kHz). The microwave couples (with  $\Omega_k = \Omega \gamma_k$ ) the trapped  $|r\rangle$  state to free  $|b_k\rangle$  states with momentum  $k$  and kinetic energy  $\epsilon_k$ . (c) The filled (empty) potential well can be viewed as the excited (ground) state  $|e\rangle$  ( $|g\rangle$ ) of a matter-wave emitter. The emission of atoms in this scenario bears close similarity to the emission of photons in photonic bandgap (PBG) materials, both featuring quadratic dispersions and energetically forbidden regions.

As a consequence, the detuning and strength of the coupling are shifted to  $\Delta_k = \delta + (\bar{\varepsilon}_0 - \varepsilon_k)/\hbar$  and  $\Omega_k = \Omega\gamma_k$ , respectively, with  $\gamma_k = \langle k|\psi_e\rangle$  denoting the overlap of the external wavefunctions. Integration over all possible momenta  $k$  then yields [126]

$$\hat{H} = \sum_k \hbar g_k e^{i\Delta_k t} |g\rangle \langle e| \hat{b}_k^\dagger + \text{H.c.}, \quad (7.2)$$

with  $g_k = \Omega_k/2$  i.e. the standard Weisskopf-Wigner Hamiltonian describing spontaneous emission into a vacuum of modes  $(k, \varepsilon_k)$  (see Fig. 7.1(b)). In contrast to optical emission in free space, the dispersion relation  $\varepsilon_k$  is quadratic as in a photonic crystal, cf. Fig. 7.1(c). In such crystals, the emission energy relative to the edge of the continuum may be adjusted through the crystal's band structure; in our system, the excitation energy  $\hbar\Delta \equiv \hbar\Delta_{k=0}$  itself is tunable including the case  $\Delta < 0$ . Importantly, the tunability also includes the vacuum coupling  $g_k$ , which is set by  $\Omega$ .

### 7.3 Sample Preparation

In the experiment we use  $^{87}\text{Rb}$  atoms in the hyperfine ground states  $|r\rangle = |F=1, m_F=-1\rangle$  and  $|b\rangle = |2, 0\rangle$  (the fact that  $|r\rangle$  lies below  $|b\rangle$  is inconsequential in the rotating frame). The atoms are confined to a two-dimensional array of  $\sim 10^3$  isolated lattice tubes spaced at 532 nm, each with a radial confinement of  $\omega_\perp = 2\pi \times 26$  kHz and a residual axial confinement of  $\omega_z = 2\pi \times 97$  Hz that quantizes the mode spectrum for released  $|b\rangle$  atoms in the  $z$  direction (see Fig. 7.1), but is inconsequential for times much shorter than  $\tau_z = 2\pi/\omega_z \sim 10$  ms. A state-selective lattice with period  $\lambda_z/2 = 395$  nm and harmonic-oscillator frequency  $\omega_0 = 2\pi \times 40(1)$  kHz strongly confines the  $|r\rangle$  atoms along the tube axis (the harmonic oscillator frequency is the approximate harmonic potential at the minimum of each potential well  $\omega_0 = 2\sqrt{s}E_{r,790.1 \text{ nm}}$ , with  $s$  the lattice depth in recoil energies  $E_{r,790.1 \text{ nm}}$ ).

Starting with an optically-trapped Bose-Einstein condensate [134], we first create an atomic Mott insulator of  $|r\rangle$  atoms by simultaneously ramping up all three optical lattices, over a time of 90 ms, to depths of  $\{40E_{r,1064 \text{ nm}}, 40E_{r,1064 \text{ nm}}, 30E_{r,790.1 \text{ nm}}\}$  in the  $\{x, y, z\}$  directions, where  $E_{r,\lambda} = \hbar^2/2m\lambda^2$  is the respective recoil energy. This procedure results in a deeply-confined, Mott-insulating sample, while also shifting the minimum of the tube potentials by  $\sim 10 \mu\text{m}$  with respect to the sample. The shift (which is comparable to the sample size and corresponds to the change of the gravitational sag during the ramp [134] after the atoms are effectively pinned by the  $z$ -lattice) leaves the

resonance condition for individual atoms unaffected since  $|r\rangle$  and  $|b\rangle$  experience the same tube potential.

After loading the atoms into the lattice, we transfer a fraction of  $\sim 0.82$  to an intermediate state  $|2, 1\rangle$ , using a two-photon RF-pulse (microwave radiation at 6.8 GHz and radiofrequency radiation at  $\sim 3$  MHz) of 0.95 ms duration. These atoms are finally removed using resonant light on the  $D_2$  cycling transition ( $F = 2 \rightarrow F' = 3$ ). Using the  $|2, 1\rangle$  state has the advantage that there is no first order shift in the energy difference between  $|1, -1\rangle$  and  $|2, 1\rangle$  due to either the magnetic field or the state selective optical potential. Also, collisional shifts [177] of doubly (triply) occupied sites are  $\sim 50(100)$  Hz for our lattice parameters, much less than the spectral width of the pulse. This yields a sample of  $2.8(2) \times 10^4$   $|r\rangle$  atoms with an average site occupation  $\langle n_i \rangle \lesssim 0.5$  in the tubes. Having thus created an initial state of matter-wave emitters, we then switch on a 6.8 GHz microwave field of variable coupling strength  $\Omega$  and detuning  $\Delta$ .

## 7.4 Markovian Dynamics

A common scenario considered in the Wigner-Weisskopf model is emission deep into the continuum, such that the decay dynamics are much slower than the time scale set by the excited-state energy (or the elevation above the band edge in the case of a photonic crystal). This allows for a Markovian treatment and results in exponential decay of the excited state. Following Fermi's Golden Rule, the decay width  $\Gamma$  is the product of the mode density  $\rho$  and the square of a matrix element  $H_{ge}$  which, for optical decay, is the product of the electric dipole moment and the zero-point field of the resonant mode. For our system, an analogous analysis [126] (valid for  $\Omega/\Delta \ll 1$ ) leads to  $\Gamma = \Omega_{\vec{k}}^2 / \sqrt{\omega_0 \Delta}$ , containing the 1D mode density  $\rho \propto 1/\sqrt{\Delta}$  and  $H_{ge} \propto \hbar \Omega_{\vec{k}}$ , where  $\vec{k} = \sqrt{2m\Delta/\hbar}$  labels the resonant mode.

Because of the residual axial tube confinement,  $\omega_z$ , all measurements are taken for  $\Omega/\omega_z > 1$  and associated time scales shorter than  $\tau_z = 2\pi/\omega_z \sim 10$  ms. The measured  $|r\rangle$  population is shown in Fig. 7.2 for parameters in the (quasi-)Markovian regime  $(\Omega/\Delta)^2 \ll 1$  as a function of time (a) and detuning (b); the data in (a) are for  $\Omega/\Delta \approx 0.4$  at  $\Delta \approx 2\pi \times 2$  kHz (with  $\Gamma = 2\pi \times 72$  Hz). After a variable coupling time  $t$ , we observe an irreversible, exponential decay in agreement with the expectation; however, the measured population does not decay to zero but instead saturates at a finite value. We qualitatively explain this discrepancy by taking into account that an excited emitter is not isolated but part of a (mostly) ground-state array that enables reabsorption,

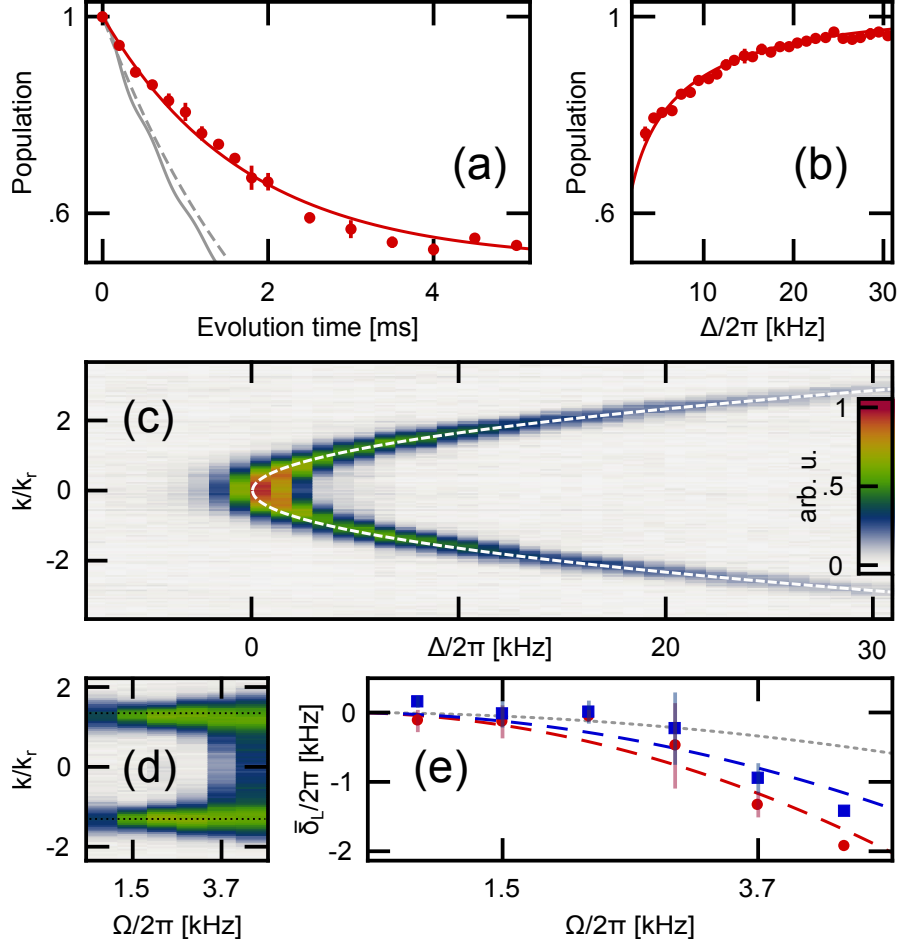


Figure 7.2: Markovian Regime. (a) Time evolution of the lattice population for  $\Omega = 2\pi \times 0.74(5)$  kHz and  $\Delta = 2\pi \times 1.9(3)$  kHz. Each point is the average of at least 3 measurements, bars are the standard error of the mean. The red line is a phenomenological exponential decay curve with a fitted rate of  $2\pi \times 94(3)$  Hz and an offset of  $0.503(4)$ . In contrast, the light gray lines represent the Markovian approximation (dashed,  $\Gamma = 2\pi \times 72(12)$  Hz) and the exact analytical solution for an isolated emitter [126] (solid). (b) Lattice population as a function of  $\Delta$  for  $t = 0.4$  ms and  $\Omega = 2\pi \times 1.5(1)$  kHz. The solid line is the Markovian expectation with the overall decay width  $\Gamma$  scaled by  $0.61(1)$ . (c) Detected momentum distribution of  $|b\rangle$  atoms versus  $\Delta$  for parameters as in (b). The dashed line is the single-particle dispersion; data for small positive and for negative detunings are outside the Markovian regime. (d) Raw TOF data for extracting the energy shift at  $\Delta = 2\pi \times 6.0(3)$  kHz. (e) Measured shifts  $\bar{\delta}_L = \Delta_{\bar{k}} - \Delta$  in the regime  $\Omega/\Delta < 1$ , for  $\tilde{\Omega}t = 1.24$  and averaged over  $\Delta = 2\pi \times 1, 2, 4, 6$  kHz. The data are extracted from the second moment (maximum) of the momentum distribution, shown using blue squares (red circles). The blue solid and red dashed lines are quadratic fits, the gray dotted line represents  $\delta_L(\Omega)$ .

in analogy to an optically thick medium. In the Weisskopf-Wigner formalism, the array is modeled by introducing site-dependent phases and projectors, resulting in [124]

$$\hat{H} = \sum_{k,j} \hbar g_k e^{i(\Delta_k t - k z_j)} |g_j\rangle \langle e_j| \hat{b}_k^\dagger + \text{H.c.} \quad (7.3)$$

Following the Master-equation based treatment in [125], we expect excitations to be transferred between neighbors on a timescale  $t \sim 1/\Gamma = 2$  ms, leading to a slowdown of the decay in qualitative agreement with Fig. 7.2 (a) (see also section 7.7). Moreover, the emitted atoms cannot escape in our system for long times, which motivates the formation of a steady state as  $t$  approaches  $\tau_z$ . Here, additional dephasing effects that are not captured in this model may arise from collisions between emitted atoms (scattering between modes in each tube). At early times  $t < 1/\Gamma$ , with still weak reabsorption, the decay at fixed time  $\tau$ , cf. Fig. 7.2 (b), approximately displays the expected detuning dependence of the Weisskopf-Wigner model,  $\exp[-\Gamma(\Delta)\tau] \sim 1 - \Gamma(\Delta)\tau$  (albeit with a downward rescaling of the actual value of  $\Gamma$  at the finite pulse time  $\tau = 0.4$  ms used, with reabsorption effects already apparent).

We next characterize the momentum distribution of the emitted atoms. For this purpose we apply a 0.4 ms long coupling pulse and then observe the location of the  $|b\rangle$  atoms after 15 ms of free fall, using state-selective absorptive imaging (see section 7.6 and chapter 2 section 2.2.1). Based on the Markovian approximation, isotropic emission with wave-packets centered near the resonant momentum  $\bar{k}(\Delta)$  is expected. Figure 7.2 (c) shows the observed momentum distribution as a function of  $\Delta$ ; the emission clearly traces the parabolic dispersion. Moreover, the spectral width  $\sigma_k$  of the separated wavepackets decreases with detuning, in qualitative agreement with the expectation ( $\sigma_k \propto 1/\Delta$  for large detunings [126]; a quantitative comparison is compromised by the finite time of flight). The ‘intensity’ of the emitted matter-wave pulse strongly depends on the detuning as already seen in Fig. 7.2 (b).

The standard Markovian treatment of the Weisskopf-Wigner model yields a Lamb shift of the ground and excited states as a unitary coupling to the vacuum. An analogous analysis for our system [124, 126] yields a shift  $\delta_L = \Omega^2/\omega_0$  of the excited-state energy, to  $(\Delta - \delta_L)$ . We measure the momentum distribution for variable  $\Omega$  at several values of  $\Delta$  and then calculate the mean kinetic energy of the wave-packets both from the second moment of the momentum distributions and from the location of their fitted maxima (see 7.6 for details). To facilitate comparison with the model, the data are taken for a constant effective pulse area  $\tilde{\Omega}t$ , where  $\tilde{\Omega} = (\Omega/\omega_0)^{1/3}\Omega$ , and  $t \leq 1$  ms to mitigate propagation effects. The results for the (quasi-)Markovian regime  $(\Omega/\Delta)^2 \ll 1$  are

shown in Fig. 7.2 (d, e) as a function of  $\Omega$ . The extracted shift has the sign and approximate quadratic dependence of  $\delta_L$ , but is a factor of roughly three too large. We caution that, while this alone could point toward the existence of collective enhancement, there is no indication for superradiance [124, 218] from the decay data (which is consistent with the fact that there is no overall population inversion in the array).

## 7.5 Non-Markovian Dynamics

Our system readily allows for the study of spontaneous emission outside the Markovian regime, as already visible in Fig. 7.2 (c). In particular, the diverging one-dimensional mode density near  $\varepsilon_k = 0$  greatly enhances the effects of the edge of the continuum. For emission at low excitation energy,  $\Delta/\Omega \ll 1$ , we expect dynamics reminiscent of a two-level system, with damping provided by low-energy modes. Results of measurements at  $\Delta = 0$  are shown in Fig. 7.3 (a). We observe oscillations similar to the predictions of our isolated-emitter model [126] (which now features a finite offset, in contrast to positive detunings) but with higher frequency and less damping, suggesting that the dynamics are coherently enhanced by low-energy modes, whose wavelengths can extend over several emitters (see also section 7.7).

For emission below the continuum edge, i.e. for  $\Delta < 0$ , we expect the formation of a stationary bound state [124, 126], as illustrated in Fig. 7.3 (c). For our one-dimensional system, this state consists of a partly excited emitter dressed by an evanescent, approximately exponentially decaying matter wave, with a binding energy  $\hbar\omega_B \approx \hbar\Delta$  and localization length [126]  $\xi = 1/\sqrt{2m|\omega_B|/\hbar}$ . To isolate the bound state, the coupling needs to be turned on slowly to prevent the additional population of freely propagating modes [126] representing a non-adiabatic, transient shedding of matter waves. However, we first proceed as before by switching on the coupling, at  $\Delta = -2\pi \times 1.7$  kHz. The lattice population, shown in Fig. 7.3 (b), shows a transient oscillation (with much lower amplitude than at the edge) settling to an asymptotic value below unity (with an observable  $|b\rangle$  population, cf. Fig. 7.2 (c)). Remarkably, our single-emitter model [126] now closely fits the data within the experimental uncertainties. Indeed, for the chosen parameters,  $\xi$  is less than half a lattice period, which should lead to a relative suppression of long-range couplings.

To access the properties of the bound state, we first determine the fraction of  $|b\rangle$  atoms by comparing the asymptotic lattice population for a sudden and for an exponential turn-on of the coupling. The results shown in Fig. 7.3 (d)

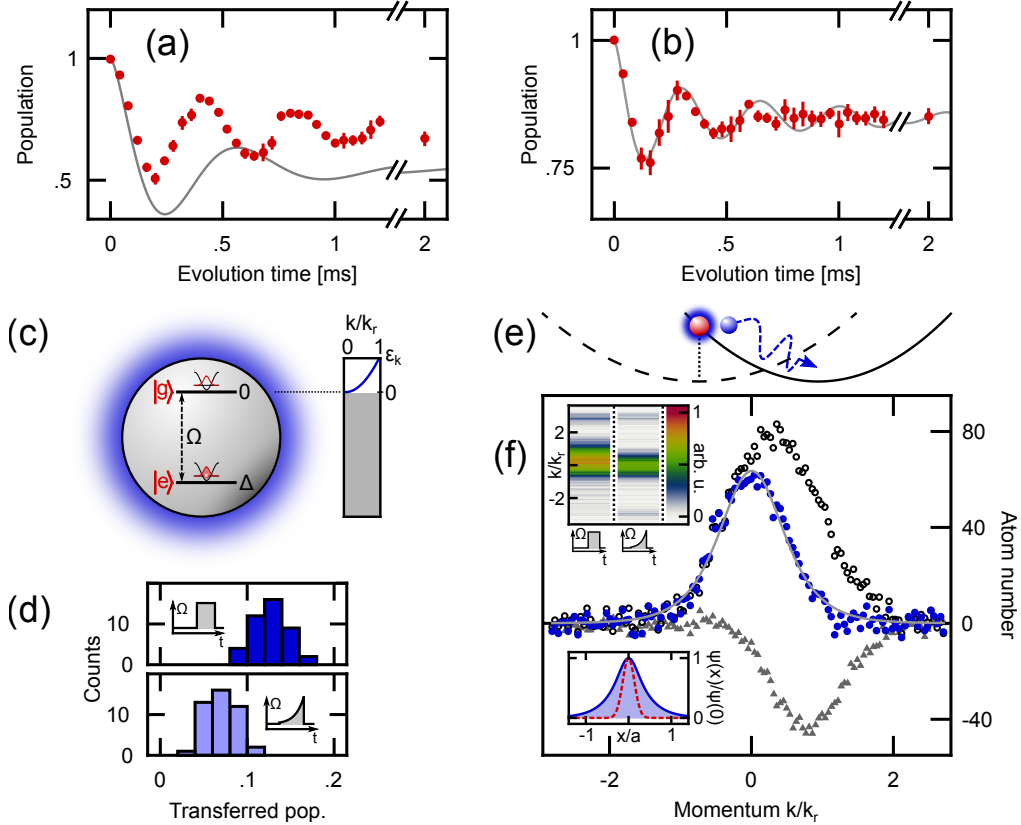


Figure 7.3: Non-Markovian dynamics and bound-state formation. (a) Time evolution of the  $|r\rangle$  population for  $\Delta = -2\pi \times 0.1(3)$  kHz and  $\Omega = 2\pi \times 3.0(3)$  kHz. The gray line is our analytical model. (b) Same as in (a) but for  $\Delta = -2\pi \times 1.7(3)$  kHz. The fit parameters of the analytic model are  $\Delta = -2\pi \times 2.08(3)$  kHz and  $\Omega = 2\pi \times 2.79(4)$  kHz. (c) Illustration of a stationary bound state for negative excitation energies. (d) Asymptotic fraction of  $|b\rangle$  atoms after  $t = 2.6$  ms, for  $\Omega$  as in (a) and  $\Delta = -2\pi \times 2.2(3)$  kHz. The top (bottom) histogram is for a sudden (adiabatic) turn-on of the coupling, 50 experimental runs each. (e) Illustration of separation of evanescent and propagating waves along the weakly confining tube axis. (f) Momentum distributions of  $|b\rangle$  atoms for the two scenarios considered in (d). Open (filled) circles are for the sudden (adiabatic) turn on of the coupling and their difference (triangles). The solid line represents the square of the Fourier-transform of the analytic evanescent wavefunction [126], fitted to the adiabatic data ( $\Delta_{\text{fit}} = 2\pi \times 2.1(1)$  kHz). The center of mass of the non-adiabatic data set is shifted by  $p_s = 0.32(1) \hbar k_r$  relative to the adiabatic data set; and that of their difference (with a half width at half maximum of  $0.57(1) \hbar k_r$ ) is shifted by  $p_s = 0.80(1) \hbar k_r$ . The expectation for free atoms is  $p_s = 0.83(7) \hbar k_r$ . Lower inset: Corresponding real-space evanescent wavefunction (blue, solid) and Wannier function of a lattice-trapped  $|r\rangle$  atom (dashed, red). Upper inset: Raw data for momentum distributions of (e) before subtraction of spurious higher-band contribution (see section 7.6).

show that 7.1(2)% of the population are in the evanescent wave, with a total  $|b\rangle$  population of 12.7(2)%. The observed fraction of  $|b\rangle$  atoms in the bound state

(55%) is close to the expectation [126] of 47% for the chosen parameters, with the excess possibly stemming from residual non-adiabaticity of the ramping (we noticed an inconsistency within [126] for the total  $|b\rangle$  fraction, but this does not affect the relative  $|b\rangle$  fraction in the bound state). Importantly, the recorded momentum distribution of the bound evanescent fraction of  $|b\rangle$  atoms, see Fig. 7.3 (f), can be directly compared to the prediction of our analytical model [126] due to the absence of propagation effects. Fitting the model to the data for the adiabatic ramp-up (with  $\Delta$  as the only fit parameter) reproduces its experimental value to within the experimental uncertainty, and the agreement between the model and the measured momentum distribution is indeed excellent. The localization length obtained from the exact model is  $\xi = 142(3)$  nm (we note that for the parameters chosen [126]  $\omega_B \approx 1.3\Delta$ ).

Finally, additional direct evidence for the non-adiabatically released part can be obtained by comparing the adiabatic momentum distribution to that recorded after the rectangular pulse. Since our sample is prepared off-center from the potential minimum along the tube direction (cf. Fig. 7.3 (e); see section 7.6), the distribution of the shed  $|b\rangle$  atoms can separate in momentum space from the bound fraction. The pulse duration used in this experiment corresponds to about a quarter oscillation period (2.6 ms) along the tube axis, thus maximizing this differential effect. As seen in Fig. 7.3 (f), the (symmetric) difference of the two momentum distributions is centered at a finite momentum expected for atoms released with zero velocity at the beginning of the pulse. This finding is consistent with the time evolution in Fig. 7.3 (b), which suggests that the release of the unbound fraction occurs within a short time ( $\sim 0.5$  ms) after the coupling is turned on. We note that, as a result of propagation in the tubes for a quarter oscillation period, the width of the momentum distribution of the released atoms reflects that of their distribution in real space ( $v_z = z\omega_z$ ). The extracted half width at half maximum of  $5.47(9)$   $\mu\text{m}$  is comparable to the Thomas-Fermi size of the initial condensate.

Much of the present work has focused on basic properties arising from the tunability of our Wigner-Weisskopf system, including the formation of bound states below the edge of the mode continuum. On the single-emitter level, this provides a direct analogy to atomic decay near the bandgap of a photonic crystal. We note that, in yet another context, the observed non-Markovian oscillatory dynamics also reproduces predictions for electron photo-detachment from negative ions [219, 220]. The optical lattice geometry opens up various additional avenues of inquiry. For emission sufficiently above the continuum edge, these may include novel types of superradiance that depend on the degree of coherence of the lattice population (superfluid or Mott-insulating) [124, 125] and have no analog in optical systems. Moreover, con-

trolling the longitudinal waveguide level spacing should allow for studies of the transition between the Dicke- and Tavis-Cummings-type models in quantum optics [102, 124] (restricted to co-rotating terms) including their modification in the non-Markovian regime. Unlike photons, the emitted atoms can directly interact with each other, which should give rise to additional, nonlinear effects modifying the population dynamics. For negative energies, the bound state lends itself to the realization of lattice models [124] with modified tunneling and interactions. Superficially, the structure of the bound state resembles that of a lattice polaron [93, 221] (for which a phononic Lamb-shift has recently been measured [170]), with massive vacuum excitations replacing massless Bogoliubov sound excitations. Rather than reducing transport, the bound state here leads to an enhancement of mobility. The presence of tunneling with a tunable range is, for example, of interest for studies of integrability and thermalization in one-dimensional geometries.

## 7.6 Experimental Details

### 7.6.1 Experimental Procedures

In this section we outline the experimental procedures and details that we used to take our experimental data.

#### Atom Detection

We suddenly switch off the microwave coupling  $\Omega$  and measure the population remaining in the lattice and access the momentum distribution of the released atoms with state-selective absorptive imaging, using a combination of band-mapping and Stern-Gerlach separation in time-of-flight (see also chapter 2 section 2.2.1).

The state detection begins with a 500  $\mu\text{s}$  bandmap step, during which all lattice potentials are ramped down to zero (the bandmap is done for technical reasons, inhibiting the rapid transverse expansion out of the tube potentials). Subsequently all remaining trapping potentials are turned off suddenly, and after a  $\sim 1$  ms expansion time, a pulse sequence for magnetic-field characterization (see below) is applied. This is immediately followed by a 5 ms long magnetic field gradient pulse to separate states of different magnetic moments. Finally, following a total of 14.5 ms after release from the optical potential, a 200  $\mu\text{s}$  long imaging pulse, using resonant light on the  $F = 2 \rightarrow F' = 3$  D<sub>2</sub> cycling transition, is used to detect the  $F = 2$  atoms, yielding a total effective time-of-flight (TOF) of 14.6 ms for atoms in this state. The  $F = 1$  atoms

are repumped for 100  $\mu\text{s}$  using resonant  $\text{D}_2$  light ( $F = 1 \rightarrow F' = 2$ ) after an additional 2.7 ms, immediately followed by another 200  $\mu\text{s}$  long imaging pulse ( $\text{D}_2$ ,  $F = 2 \rightarrow F' = 3$ ) to detect the repumped  $F = 1$  atoms for a total TOF of 17.6 ms. Since all magnetic moments are unique within  $F=1$  and  $F=2$  separately, we fully resolve the population in each individual hyperfine state  $|F, m_F\rangle$ . We note that, technically, the cloud centers of  $F = 1$  and  $F = 2$  along the imaging direction are still overlapped during the second imaging pulse; however, the  $F = 2$  atoms are pushed out of the field-of-view by the time the  $F = 1$  detection occurs.

### Momentum-space Calibration

Our standard momentum calibration relies on Kapitza-Dirac diffraction (KDD) [157] (see also section 2.2.2) from the  $z$  lattice. For a more precise determination of emission momenta, we take into account residual propagation in the tubes which slows the atomic motion. The tubes are created, after ramping up the  $z$  lattice, by partial retro-reflection of the Gaussian beams of our optical trap ( $1/e^2$  radius of  $w = 135 \mu\text{m}$ ) [134], which leads to an increase of the optical confinement  $\omega_z/2\pi$  from 72(1) Hz to 97(1) Hz (with gravity along  $z$ ). The tubes are again ramped down within 500  $\mu\text{s}$  after the microwave pulse (together with the  $z$  lattice, for band-mapping purposes), followed by a switch off of the optical trap. We numerically simulate the motion of atoms in the tubes, by assuming that the release (with momentum  $\pm\bar{k}$ ) occurs midway through the pulse at the center of the 72 Hz trap, and then calculate the trajectories in the time-dependent optical potential until detection after 14.6 ms of time-of-flight. We see that the calibration differs from the KDD results by  $-(0.5, 1, 6)\%$  for pulse durations of (0.2, 0.4, 1) ms, with negligible differences for shorter pulses. These corrections are included in Fig. 7.2.

## 7.6.2 Characterization of Magnetic Fields and Optical Potentials

The quoted uncertainty of 300 Hz in the detuning  $\Delta$  has contributions from both differential Zeeman- and AC-Stark shifts, which are characterized as follows:

### Magnetic Fields

All experiments are carried out at fields between 4.9998(1) G and 5.0002(1) G. Here the error bar corresponds to an uncertainty in the bare level splitting

between  $|r\rangle$  and  $|b\rangle$  of 70 Hz. The magnetic field for each iteration of the experiment is monitored using a series of Rabi-pulses during time of flight [129], in which atoms in  $|1, -1\rangle$  are redistributed to the  $|2, -2\rangle$  and  $|2, -1\rangle$  states. This method allows field reconstruction to within 100  $\mu\text{G}$  (for details see chapter 5). The inhomogeneity of the magnetic field across the sample is characterized via a Ramsey pulse sequence. It does not exceed 70  $\mu\text{G}$ , which corresponds to 15 Hz rms variation of  $\Delta$  across the sample for the  $|r\rangle$ ,  $|b\rangle$  state pair.

### Differential Optical Potential

The state-selective optical potential is created using a  $\sigma^-$ -polarized laser beam (waist  $w_0 = 230 \mu\text{m}$ ) at  $\lambda_z = 790.10(2) \text{ nm}$ . Polarization and wavelength are set (using a  $\lambda/4$ -waveplate and laser-controls) such that the lattice potential seen by the  $|r\rangle$ -atoms is maximized, while the  $|b\rangle$  atoms experience zero potential. The change in lattice potential with wavelength is  $0.12E_r/0.01 \text{ nm}$ , while the maximum theoretically possible polarization change ( $\sigma^-$  to  $\pi$ ) changes the potential by  $0.01 E_r$  (We note that the polarization is stable in the experiment). We characterize the state selectivity using a sequence of ten Kapitza-Dirac pulses (10  $\mu\text{s}$ ) spaced at the Talbot-resonance time (see also chapter 2 section 2.2.2) [160]  $\tau = (4E_{r,790.1}/h)^{-1} = 68 \mu\text{s}$ , to ensure a suppression of the optical potential for  $|b\rangle$  atoms by a factor of better than 100 ( $V_{|b\rangle}/V_{|r\rangle} < 100$ ), consistent also with the remaining wavelength uncertainty of 0.02 nm.

A crucial part of the experiment is a reliable determination of the resonance condition, or alternatively, the value of  $\Delta$ . Since the creation of our matter-wave emitter (in Fig. 7.1 (c)) starts with a detuned Rabi oscillation of two hyperfine states, we first (post-) stabilize the magnetic field as discussed above and in [129]. The resonance condition (‘excited state energy’) of the matter-wave emitters is determined by the detuning of the hyperfine spin and the zero point shifts to both states induced by the state-selective potential. Since we can currently control the wavelength to 0.02 nm rms accuracy only, the overall uncertainty is limited to a maximum of  $\pm 340 \text{ Hz}$  rms, with the most extreme fluctuations limited to 1 kHz. To address and monitor this issue, we bracket each measurement (such as measuring the time evolution at a given detuning) by a resonance curve, an average of which is shown in Fig. 7.4 (see also Fig. 5.5). The resonance curve is taken without any transverse lattices on and with a low atom number in the optical trap ( $\sim 30,000$  atoms) and at only partial transfer (maximally 30 percent) to minimize systematic mean field/density shifts. The residual systematic shift of the resonance condition due to mean-field/density effects is estimated to be less than 100 Hz via direct simulation of resonance

curves using the 1D-time-dependent Gross-Pitaevskii equation (see appendix A). The scatter of the center of resonance curves during a typical measurement has a rms value of 0.3 kHz, which is the quoted uncertainty of the detuning, and which also matches the expected wavelength reproducibility of 0.02 nm.

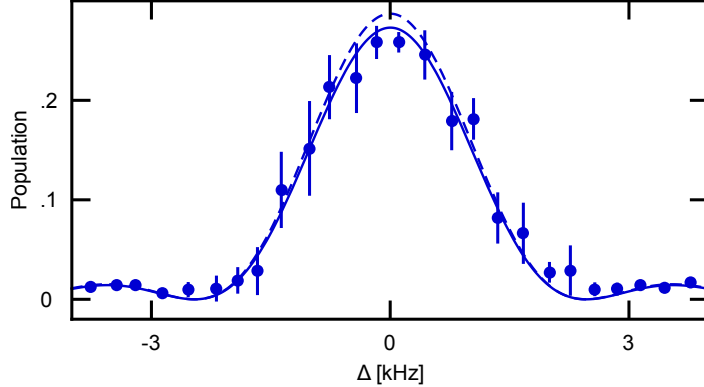


Figure 7.4: Average spectrum of coupling stationary atoms into the  $z$  lattice (generated from a series of 17 spectra taken over a one-day period whose fitted centers are shifted to zero). The coupling strength is  $\Omega = 740(10)$  Hz and the pulse time is  $400 \mu\text{s}$ , with the datapoints binned into 300 Hz wide bins. The solid curve is a fit to the data with  $\Omega$  as a free fit parameter, while the dashed curve has no free parameters, and the effective coupling strength has been calculated using the wavefunction overlap between free and trapped species of  $\gamma_0 = 0.72$ .

To characterize inhomogeneities of the state-selective optical potential, we first precisely calibrate the Rabi coupling strength (for a range of coupling strengths) in the absence of state-selective potentials. We then compare the maximum observed population transfer in a Rabi spectrum to the expected maximum population transfer into the lattice. Based on the comparison, we estimate an upper bound for the inhomogeneity of 300 Hz rms. We note that the inhomogeneities of the trapping potential at 1064nm do not exceed 20 Hz rms across the sample. For comparison, the absolute magnitude of the spectroscopic shift of ( $|1, -1\rangle \leftrightarrow |2, 0\rangle$ ) in the center of the optical trap does not exceed 400 Hz.

### (\*)Future Stabilization of the State-Selective Lattice Laser

In future experiments we want to stabilize the laser wavelength directly using a wavemeter which has higher accuracy and precision (four digits of precision

after the decimal of the nanometer in are needed instead of two digits). We are adding a more detailed calculation here which specifies exactly the differential shift in level splitting when the wavelength changes by 1 pm. For a wavelength shift of 1 pm, at tune-out wavelength for the free species and 30  $E_r$  potential depth for the trapped species, then the trapped species potential depth changes by  $\pm 0.015 E_r/\text{pm}$  (away from 30  $E_r$  while the potential depth of the free species changes from 0 to  $\pm 0.012 E_r/\text{pm}$ . For the free state we can assume that the potential is a weak perturbation: the potential is small compared to the two-photon recoil energy  $E_{2r} = 4E_r$ , which is the approximate kinetic energy required to modulate the wavefunction at the periodicity of the lattice potential. Using perturbation theory on a state that is flat on the scale of a lattice wavelength, we find that the energy shift of this optical potential onto the free state is simply the average value of the lattice potential, i. e. half the lattice potential:

$$\Delta E_{\text{free}} = \langle V_0 \sin^2(k_r x) \rangle \hat{=} 0.006 \frac{E_r}{\text{pm}} = h \times 22 \frac{\text{Hz}}{\text{pm}}$$

The confined species is tightly trapped, which allows us to approximate the ground state energy of the particle in the potential well using the harmonic approximation:  $\omega_0 = 2E_r\sqrt{s}/\hbar$  ( $s = V_0/E_r$  is the lattice depth in recoils), which has a ground state energy of  $\epsilon_0 = E_r\sqrt{s}$ . The slope of this is  $E_r/2\sqrt{s}$ , and hence

$$\Delta E_{\text{trapped}} = \Delta s \times \frac{E_r}{2\sqrt{s}} \hat{=} 0.0014 \frac{E_r}{\text{pm}} = h \times 5 \frac{\text{Hz}}{\text{pm}}$$

Hence the differential shift between the the two states is 17 Hz/pm. This means that the current stabilization/accuracy of the wavelength to 0.02 nm is not accurate enough to fix the level splitting to a 100 Hz level, which is however the stability given by magnetic field uncertainties.

The laser light for the state-selective lattice potential is generated using a Coherent-899 solid-state laser, pumped by a Coherent Verdi-V10 diode pumped solid-state laser. Measurements using a higher resolution wavemeter (Burleigh WA-1500, accurate to 1pm in wavelength, built in He-Ne reference) show that the laser is indeed very stable in the short term (over minutes), due to it being locked to the external reference cavity. Over the course of longer periods (half hour to several hours) the laser can undergo large wavelength changes (up to 0.02 nm change, undetected by the wavemeter in the laboratory) possibly due to a large external perturbation of the laser cavity (sound and noise) or due to the regulatory electronics running out of range. The laser

then resettles at that wavelength, and the change cannot be detected in our current setup.

In the future we plan to directly stabilize the laser either by buying a more accurate wavemeter and using, for example, the external laser scan control to feed back slowly onto the wavelength. The laser can be scanned around its current lock-point by  $\sim \pm 10$  GHz which is approximately 0.02 nm wavelength change, so the inputs provided by the laser should be sufficient to stabilize the lattice potential down to a 10 Hz accuracy given the correct wavemeter. In the long run it would be best to replace our current Ti-Sapph laser (Coherent 899) with a more modern Ti-Sapph laser, which can easily reach line-widths of 10 kHz at drifts of less than 1 GHz per day, which is sufficient for our experiments.

### 7.6.3 Background Subtraction

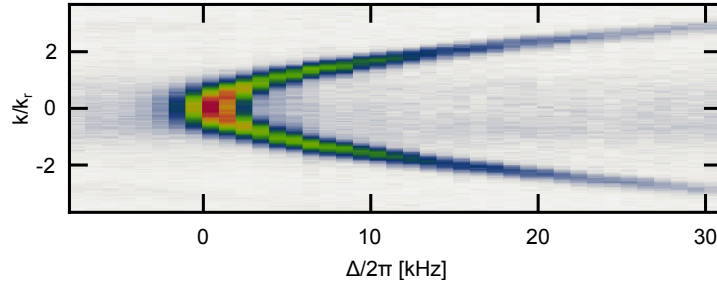


Figure 7.5: Raw momentum spectrum showing a detuning-independent, diffuse background of  $\sim 10^3$  atoms. Processed figure and details in Fig. 7.2 (c).

The sequence used to thin out the atomic sample leaves roughly  $10^3$  atoms in the  $|b\rangle$ -state before the microwave pulse is applied. This results in a diffuse background in the momentum distributions, as illustrated in Fig. 7.5. We remove this background by subtracting out reference data taken for zero pulse time. The result is Fig. 7.2 (c) of the main text.

In the main text in Fig. 7.3 (f) we also mention subtracting background due to the very small fraction of higher band population. The first excited band is expected at approximately  $2\pi \times 36(1)$  kHz or  $\pm 3\hbar k_r$ . For subtraction we first fit three Gaussian peaks for the adiabatic ramp and one soft edge box and two Gaussians to the sudden turn-on data, requiring identical atom numbers in the soft edge box and the small Gaussian. The fitted functions are subtracted from the data, which then yields the main plot in Fig. 7.3 (f).

The number of atoms emitted from higher bands is on the order of 510(30) for the sudden turn on and 260(30) for the adiabatic ramp, which is less than 1 atom in a higher band per tube. The total number emitted from higher bands changes with pulse area because the spurious emission from the higher bands is in the Markovian regime.

### 7.6.4 Energy Shift Data

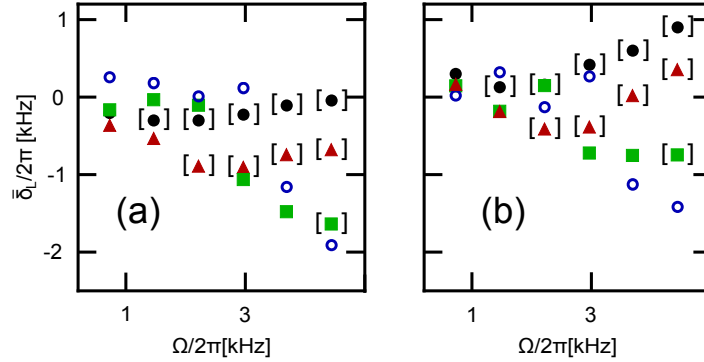


Figure 7.6: Raw data used to obtain the energy shift as shown in the text. (a) Second moment of  $k$  and (b) half separation squared both subtracted by  $\Delta/2\pi$ . The detunings are  $\Delta/2\pi = \{1000, 2000, 4000, 6000\}$  kHz for the disks (black), triangles (red), squares (green) and circles (blue) respectively. Points in brackets correspond to the non-Markovian regime  $\Omega/\Delta > 1$ .

The main motivation for a precise momentum calibration as described above lies in the smallness of the energetic shift. Another challenge is the blurring of the distribution due to propagation effects for small coupling strengths, i.e. long pulses. We use two measures for the determination of the energy of the emitted wave-packets; the squared separation of the wavepacket-centers (extracted by fitting) and the second moment of the (centered) distribution. The accuracy of the peak separation measure is limited by the fact that it ignores the physical broadening of the momentum distribution at larger coupling strengths and shorter times, while the second moment is sensitive to a blurring of the wavepackets during detection. The data obtained using both methods are shown in Fig. 7.6. In the non-Markovian regime  $\Omega/\Delta > 1$  the peaks become indistinguishable (apex of the parabola in Fig. 7.2 (c)) and a meaningful measure of a shift cannot be extracted with either method.

## 7.7 Numerical Simulation of Array Effects in Weak Harmonic Trapping Potential

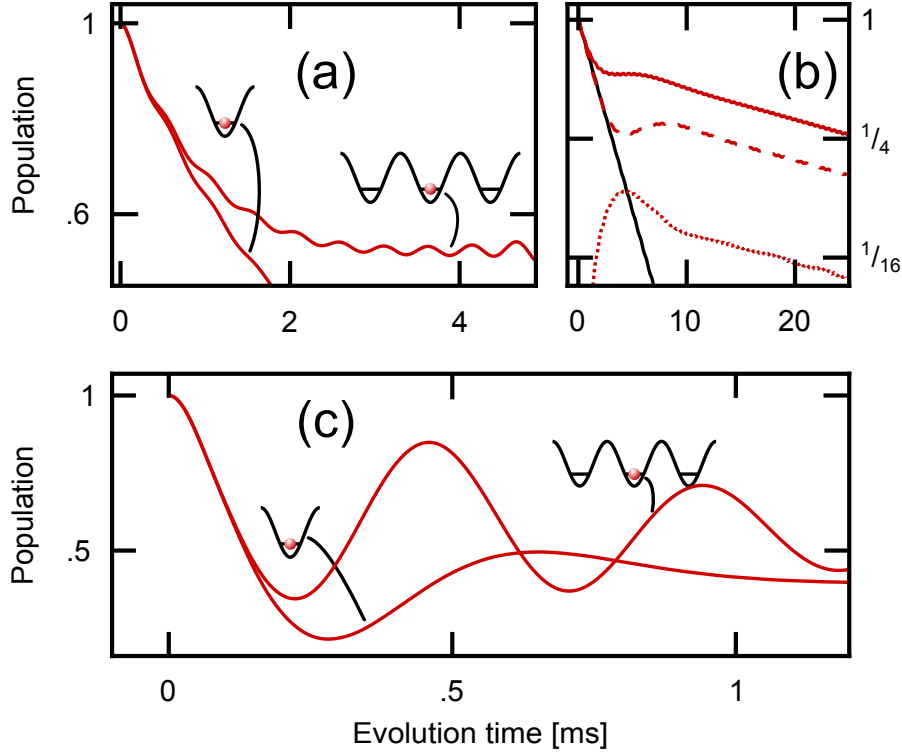


Figure 7.7: Simulated decay dynamics for a 1-site and 3-site model (with the central site initially populated), and for  $\omega_z = 2\pi \times 0.1$  kHz (a,c) and 5 Hz (b). (a) Dynamics for  $\Delta = 2\pi \times 1.9$  kHz and  $\Omega = 2\pi \times 0.74$  kHz. (b) Long-time decay dynamics of the 1-site (black) and 3-site (red) models for  $\Omega = 2\pi \times 0.74$  kHz and  $\Delta = 2\pi \times 1.9$  kHz. The dashed line shows the population of the central, initially populated, site; the dotted line shows the population of the neighboring sites. (c) Dynamics for  $\Delta = -2\pi \times 0.1$  kHz and  $\Omega = 2\pi \times 3$  kHz.

As stated in the main text, the Hamiltonian of the multi-site array [124] predicts the (resonant) transfer of excitations between neighboring emitters [125], in some similarity to the mechanisms for radiation trapping in an optically thick sample. Instead of attempting to solve this Hamiltonian, here we consider a simplistic model of an array of three emitters that is coupled to a quantized mode structure reflecting the weak longitudinal harmonic con-

finement. We chose our simplistic three-site model, with a centrally occupied site as the simplest spatially symmetric generalization of the isolated-emitter situation, which also corresponds to an ‘average segment’ in our system with approximately one empty neighbor on each side of a populated site.

We start from the Rabi-Hamiltonian (in the rotating wave approximation) and expand it to couple one or several sites ( $|r\rangle$  in the main text) to many different, weakly confined levels ( $|b\rangle$  in the main text). This Hamiltonian is (for simplicity only shown for two sites, but readily expanded to  $n$  sites)

$$\hat{H} = \frac{\hbar}{2} \begin{bmatrix} 2\bar{\delta}_1 & 0 & \Omega\gamma_{1,1} & \Omega\gamma_{1,2} & \cdots \\ 0 & 2\bar{\delta}_2 & \Omega\gamma_{2,1} & \Omega\gamma_{2,2} & \\ \Omega\gamma_{1,1} & \Omega\gamma_{2,1} & -2\Delta + \omega_z & 0 & \\ \Omega\gamma_{1,2} & \Omega\gamma_{2,2} & 0 & -2\Delta + 3\omega_z & \\ \vdots & & & & \ddots \end{bmatrix} \quad (7.4)$$

where  $\bar{\delta}_i = m\omega_z^2 r_i^2 / (2\hbar)$  is a site-dependent detuning (i.e. a site-dependent offset due to the weak harmonic confinement  $\omega_z$  experienced by both, the lattice-trapped, and free atoms), and the  $\gamma_{i,j}$  are overlaps between final and initial state wavefunctions (calculated numerically). We use modes up to a fixed frequency ( $\omega_{\max} = 2\pi \times 5\text{kHz}$ ) and restrict ourselves to  $\Delta + 2\Omega < \omega_{\max}$ .

The results of the simulation for the Markovian parameters of the main text are shown in Fig. 7.7 (a) and (b). The simulated decay for an isolated emitter reproduces the prediction of our analytical model [126] (small discrepancies arise from the fact that the latter neglects terms of order  $(\Delta/\omega_0)^2$  and  $(\Omega/\omega_0)^2$  and higher, whereas our numerical simulation retains all orders). For the three-site array, the presence of neighboring wells leads to a slowdown of the decay. The origin for this is reabsorption of emitted population by the initially empty neighbors as seen in Fig. 7.7 (b). For the array considered, the process also leads to the formation of a temporary plateau in the overall site population, which may be related to the offset observed in the experiment. However we caution that the long-time decay occurs in a regime not accessible experimentally (we assumed a denser mode structure in order to extend the continuum approximation; see below), and also the dynamics may be different in an optical lattice extending over the entire mode volume.

In Fig. 7.7 (c) we plot the dynamics in the extreme non-Markovian regime at the edge, where the coupling strength is much larger than the excited state energy. In this case we see that the single emitter displays oscillatory dynamics that quickly damps out and settles to a nonzero value, again in agreement with the analytic theory. On the other hand, the three-emitter array shows oscillatory dynamics that are of much greater amplitude and last longer. We

interpret this as a coherent enhancement of the dynamics through tunneling to nearest neighbors. The range of this tunneling diverges at the band edge causing the marked difference between single emitter and three emitters.

From our simulations we gain additional insight into the effects of the quantized mode structure. As discussed in the main text, the mode structure should act like a true continuum for short enough times where uncertainty should ‘wash out’ the levels. The simulations provide a quantitative test for this. The simplest comparison is for an isolated emitter in the Markovian limit. We see that for early times, the Markovian prediction [126] quantitatively agrees with the numerical solution, with a marked deviation (‘revival’, see Fig. 7.8) observable only at  $t^* > 0.25(\omega_z/2\pi)^{-1}$  (we restrict data taking to  $t < t^* = 2.6$  ms in the experiments in all but one case.) This is independent of the set harmonic trapping frequency or where the site is located in the array (center or off center). We note that similar results are also obtained if the continuum is discretized by assuming a periodic-box type potential, where the revival time depends on the length of the box. We furthermore note that our simulation does not reproduce  $\delta_L$  for long times.

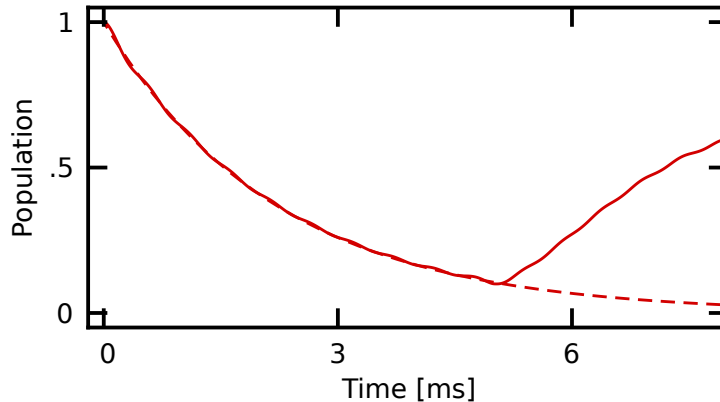


Figure 7.8: (\*) Simulated decay dynamics for a 1-site model, for  $\omega_z = 2\pi \times 0.1$  kHz,  $\Delta = 2\pi \times 1.9$  kHz and  $\Omega = 2\pi \times 0.74$  kHz. The dashed line is the prediction of the Markovian approximation. At a time corresponding to half the harmonic oscillator period (5 ms), we see a clear revival due to the finite size of the system.

## 7.8 (\*) Comparison to Non-Adiabatic Diffraction

As a final note we want to briefly point out that this work is related to work done in collaboration with J. Reeves [96] on non-adiabatic diffraction of matter waves. In the experiment by Reeves et. al [96], atoms in the freely propagating state (without transverse confinement) experience a coupling to the trapped state. While the experimental techniques developed in [96] work lay the foundation for this dissertation, we want to compare the conceptual differences between [96] and this work.

The most important difference between this work and [96] is the fact that the initial state here is in the lattice, and is made up of localized atoms (essentially in Wannier states) which reside on lattice sites. As a result, the initial state here is made up of contributions from a broad range of momenta, which leads to coupling to many different states, and hence is essential to the possibility of simulating an open quantum system. In contrast, the matter wave diffraction starts with an almost pure  $p = 0$  state, and only a discrete set of states ( $p = n \times 2\hbar k_r$ ) is ever populated, yielding effective few-level (four level) single particle dynamics.

Furthermore this work is restricted to coupling strengths which are much weaker than the two-photon recoil energy ( $E_{2r} = 4\hbar^2 k_r^2 / 2m \sim h \times 15$  kHz, which is the scale on which the coupling strength becomes large enough to effectively hybridize the optical potential of the free state (flat) and the bound state (lattice); the experiments in [96] were conducted at  $(0.5 \dots 1.0) E_{2r}$ .

# Chapter 8

## Conclusion and Outlook

The main result in this dissertation is the realization of a matter-wave analog to the Weisskopf-Wigner model in a structured one-dimensional medium. We realize the analogue by preparing a sample of atoms in a single hyperfine state that are strongly localized along all three spatial directions. Subsequent weak coupling to a hyperfine state which is approximately free along one spatial direction allows the recreation of a one-dimensional analog of the Weisskopf-Wigner model, where in our system we have, potentially coupled, arrays of artificial emitters rather than a single atom. Due to the exceptional tunability of our system, we can probe the model in unprecedented detail and see a transition from Markovian to non-Markovian time-evolution when the excited state energy becomes comparable to the coupling strength. In the extreme case of negative excited state energies, we observe the formation of a bound state, and characterize its localization length.

Since these experiments required the reliable detection of small atom numbers, an important technical prerequisite was the implementation of a fringe-removal technique to purge images of any residual artifacts which are not images of atoms. The method is implemented using empty ‘training’ images on which principal component analysis is done in order to generate a set of ‘typical’ problem images which can then be subtracted from the actual absorption images.

A major technical challenge was the control of magnetic fields in our apparatus to the level of  $\sim 50 - 100 \mu\text{G}$ . We developed a post-selection method that allows conducting experiments on a hyperfine pseudo-spin pair, and uses unused hyperfine levels to characterize the field shortly after the time of measurement. While this technique only allows for post-selection field reconstruction, the continuous monitoring of the field at exactly the position of the atoms allows for a level of stability needed. The measurement only takes 0.5 ms to

2 ms (depending on the needed accuracy) and can easily be implemented on any existing setup with hyperfine-state control.

In the future, we are interested in observing many-body effects of the matter-wave emitter system, such as superradiance [218] and especially its extension into the non-Markovian regime, as well as the emergence of effective Bose-Hubbard/Ising Hamiltonians when the excited state energy becomes negative, especially the possibility of directly tuning the tunneling range via the bound state energy. We are planning to investigate transport phenomena utilizing the bound state (e. g. Bloch oscillations) and want to study the precise influence of tuning the reservoir. The reservoir can be tuned by either applying a periodic potential to the reservoir as well, thus creating a situation where one can have an upper and a lower band edge. Another way of tuning the reservoir is to tune the weak harmonic trapping potential such that it becomes noticeably quantized (or equivalently conduct experiments for a longer time in the same weak confinement), thus realizing a Tavis-Cummings type model [124, 222].

Finally, we are interested in increasing the dimensionality for the state-selective potential in order to increase the effective dimensionality of the system from 1D to 2D or 3D, enabling us to study in detail how e. g. the diverging 1D density of states affects the dynamics close to zero excitation energy, as compared to the coherent dynamics of 2D and 3D geometries. We are excited to read about recent new proposals for our and analog systems [223, 224]. Furthermore, dimensionality plays a big role in superradiance of the system, since the density of the (matter) waves decreases in 2D and 3D away from the emitter, which is not the case in 1D.

# Bibliography

- [1] Wolfgang Nolting. *Grundkurs Theoretische Physik*. Springer, 2012.
- [2] Jun John Sakurai and Jim Napolitano. *Modern quantum mechanics*. Cambridge University Press, 2017.
- [3] Louis De Broglie. Recherches sur la théorie des quanta. *Annals of Physics (France)*, 10(3):22–128, 1925.
- [4] Albert Einstein. *Quantentheorie des einatomigen idealen Gases*. Akademie der Wissenschaften, in Kommission bei W. de Gruyter, 1924.
- [5] Satyendra Nath Bose. Plancks Gesetz und Lichtquantenhypothese. *Zeitschrift für Physik*, 26(1):178–181, 1924.
- [6] Franco Dalfovo, Stefano Giorgini, Lev P Pitaevskii, and Sandro Stringari. Theory of Bose-Einstein condensation in trapped gases. *Reviews of Modern Physics*, 71(3):463, 1999.
- [7] Enrico Fermi. Zur Quantelung des idealen einatomigen Gases. *Zeitschrift für Physik*, 36(11-12):902–912, 1926.
- [8] Paul Adrien Maurice Dirac. On the theory of quantum mechanics. *Proceedings of the Royal Society of London A*, 112(762):661–677, 1926.
- [9] Stefano Giorgini, Lev P Pitaevskii, and Sandro Stringari. Theory of ultracold atomic Fermi gases. *Reviews of Modern Physics*, 80(4):1215, 2008.
- [10] Pyotr Kapitza. Viscosity of liquid helium below the  $\lambda$ -point. *Nature*, 141(3558):74, 1938.
- [11] JF Allen and AD Misener. Flow of liquid helium II. *Nature*, 141(3558):75, 1938.

- [12] John Bardeen, Leon N Cooper, and J Robert Schrieffer. Microscopic theory of superconductivity. *Physical Review*, 106(1):162, 1957.
- [13] Carl J Hansen, Steven D Kawaler, and Virginia Trimble. *Stellar interiors: physical principles, structure, and evolution*. Springer Science & Business Media, 2012.
- [14] Mike H Anderson, Jason R Ensher, Michael R Matthews, Carl E Wieman, and Eric A Cornell. Observation of Bose-Einstein condensation in a dilute atomic vapor. *Science*, 269(5221):198–201, 1995.
- [15] Cl C Bradley, CA Sackett, JJ Tollett, and Randall G Hulet. Evidence of Bose-Einstein condensation in an atomic gas with attractive interactions. *Physical Review Letters*, 75(9):1687, 1995.
- [16] Curtis Charles Bradley, CA Sackett, and RG Hulet. Bose-Einstein condensation of lithium: Observation of limited condensate number. *Physical Review Letters*, 78(6):985, 1997.
- [17] K. B. Davis, M. O. Mewes, M. R. Andrews, N. J. van Druten, D. S. Durfee, D. M. Kurn, and W. Ketterle. Bose-Einstein Condensation in a Gas of Sodium Atoms. *Physical Review Letters*, 75:3969–3973, 1995.
- [18] Brian DeMarco and Deborah S Jin. Onset of Fermi degeneracy in a trapped atomic gas. *Science*, 285(5434):1703–1706, 1999.
- [19] MR Andrews, CG Townsend, H-J Miesner, DS Durfee, DM Kurn, and W Ketterle. Observation of interference between two Bose condensates. *Science*, 275(5300):637–641, 1997.
- [20] M-O Mewes, MR Andrews, DM Kurn, DS Durfee, CG Townsend, and W Ketterle. Output coupler for Bose-Einstein condensed atoms. *Physical Review Letters*, 78(4):582, 1997.
- [21] Immanuel Bloch, Theodor W Hänsch, and Tilman Esslinger. Atom laser with a cw output coupler. *Physical Review Letters*, 82(15):3008, 1999.
- [22] Edward W Hagley, Lu Deng, M Kozuma, J Wen, Kristian Helmerson, SL Rolston, , and William D Phillips. A well-collimated quasi-continuous atom laser. *Science*, 283(5408):1706–1709, 1999.
- [23] M-O Mewes, MR Andrews, NJ Van Druten, DM Kurn, DS Durfee, CG Townsend, and W Ketterle. Collective excitations of a Bose-Einstein condensate in a magnetic trap. *Physical Review Letters*, 77(6):988, 1996.

- [24] MR Andrews, DM Kurn, H-J Miesner, DS Durfee, CG Townsend, S Inouye, and W Ketterle. Propagation of sound in a Bose-Einstein condensate. *Physical Review Letters*, 79(4):553, 1997.
- [25] Alexander L Fetter. Rotating trapped Bose-Einstein condensates. *Reviews of Modern Physics*, 81(2):647, 2009.
- [26] C Raman, M Köhl, R Onofrio, DS Durfee, CE Kuklewicz, Z Hadzibabic, and W Ketterle. Evidence for a critical velocity in a Bose-Einstein condensed gas. *Physical Review Letters*, 83(13):2502, 1999.
- [27] R Onofrio, C Raman, JM Vogels, JR Abo-Shaeer, AP Chikkatur, and W Ketterle. Observation of superfluid flow in a Bose-Einstein condensed gas. *Physical Review Letters*, 85(11):2228, 2000.
- [28] S Inouye, AP Chikkatur, DM Stamper-Kurn, J Stenger, DE Pritchard, and W Ketterle. Superradiant Rayleigh scattering from a Bose-Einstein condensate. *Science*, 285(5427):571–574, 1999.
- [29] Dominik Schneble, Yoshio Torii, Micah Boyd, Erik W Streed, David E Pritchard, and Wolfgang Ketterle. The onset of matter-wave amplification in a superradiant Bose-Einstein condensate. *Science*, 300(5618):475–478, 2003.
- [30] Shin Inouye, Tilman Pfau, Subhadeep Gupta, Ananth Chikkatur, Axel Görlitz, David Pritchard, and Wolfgang Ketterle. Phase-coherent amplification of atomic matter waves. *Nature*, 402(6762):641, 1999.
- [31] Mikio Kozuma, Yoichi Suzuki, Yoshio Torii, Toshiaki Sugiura, Takahiro Kuga, EW Hagley, and L Deng. Phase-coherent amplification of matter waves. *Science*, 286(5448):2309–2312, 1999.
- [32] S Burger, K Bongs, S Dettmer, W Ertmer, K Sengstock, A Sanpera, GV Shlyapnikov, and M Lewenstein. Dark solitons in Bose-Einstein condensates. *Physical Review Letters*, 83(25):5198, 1999.
- [33] Kevin E Strecker, Guthrie B Partridge, Andrew G Truscott, and Randall G Hulet. Formation and propagation of matter-wave soliton trains. *Nature*, 417(6885):150, 2002.
- [34] S Inouye, MR Andrews, J Stenger, H-J Miesner, DM Stamper-Kurn, and W Ketterle. Observation of Feshbach resonances in a Bose-Einstein condensate. *Nature*, 392(6672):151, 1998.

- [35] Cheng Chin, Rudolf Grimm, Paul Julienne, and Eite Tiesinga. Feshbach resonances in ultracold gases. *Reviews of Modern Physics*, 82(2):1225, 2010.
- [36] J Stenger, S Inouye, A P Chikkatur, DM Stamper-Kurn, DE Pritchard, and W Ketterle. Bragg spectroscopy of a Bose-Einstein condensate. *Physical Review Letters*, 82(23):4569, 1999.
- [37] Jacob L Roberts, Neil R Claussen, Simon L Cornish, Elizabeth A Donley, Eric A Cornell, and Carl E Wieman. Controlled collapse of a Bose-Einstein condensate. *Physical Review Letters*, 86(19):4211, 2001.
- [38] Elizabeth A Donley, Neil R Claussen, Simon L Cornish, Jacob L Roberts, Eric A Cornell, and Carl E Wieman. Dynamics of collapsing and exploding Bose-Einstein condensates. *Nature*, 412(6844):295, 2001.
- [39] Dale G Fried, Thomas C Killian, Lorenz Willmann, David Landhuis, Stephen C Moss, Daniel Kleppner, and Thomas J Greytak. Bose-Einstein condensation of atomic hydrogen. *Physical Review Letters*, 81(18):3811, 1998.
- [40] Giovanni Modugno, Gabriele Ferrari, Giacomo Roati, Robert J Brecha, A Simoni, and Massimo Inguscio. Bose-Einstein condensation of potassium atoms by sympathetic cooling. *Science*, 294(5545):1320–1322, 2001.
- [41] Alice Robert, Olivier Sirjean, Antoine Browaeys, Julie Poupard, Stephan Nowak, Denis Boiron, Christoph I Westbrook, and Alain Aspect. A Bose-Einstein condensate of metastable atoms. *Science*, 292(5516):461–464, 2001.
- [42] Tino Weber, Jens Herbig, Michael Mark, Hanns-Christoph Nägerl, and Rudolf Grimm. Bose-Einstein condensation of cesium. *Science*, 299(5604):232–235, 2003.
- [43] Yosuke Takasu, Kenichi Maki, Kaduki Komori, Tetsushi Takano, Kazuhito Honda, Mitsutaka Kumakura, Tsutomu Yabuzaki, and Yoshiro Takahashi. Spin-singlet Bose-Einstein condensation of two-electron atoms. *Physical Review Letters*, 91(4):040404, 2003.
- [44] Axel Griesmaier, Jörg Werner, Sven Hensler, Jürgen Stuhler, and Tilman Pfau. Bose-Einstein condensation of chromium. *Physical Review Letters*, 94(16):160401, 2005.

- [45] Sebastian Kraft, Felix Vogt, Oliver Appel, Fritz Riehle, and Uwe Sterr. Bose-Einstein condensation of alkaline earth atoms: Ca 40. *Physical Review Letters*, 103(13):130401, 2009.
- [46] Simon Stellmer, Meng Khoon Tey, Bo Huang, Rudolf Grimm, and Florian Schreck. Bose-Einstein condensation of strontium. *Physical Review Letters*, 103(20):200401, 2009.
- [47] YN Martinez De Escobar, Pascal Gerry Mickelson, M Yan, BJ DeSalvo, Sarah B Nagel, and TC Killian. Bose-Einstein Condensation of Sr 84. *Physical Review Letters*, 103(20):200402, 2009.
- [48] K Aikawa, A Frisch, M Mark, S Baier, A Rietzler, R Grimm, and F Ferlaino. Bose-Einstein condensation of erbium. *Physical Review Letters*, 108(21):210401, 2012.
- [49] Mingwu Lu, Nathaniel Q Burdick, Seo Ho Youn, and Benjamin L Lev. Strongly dipolar Bose-Einstein condensate of dysprosium. *Physical Review Letters*, 107(19):190401, 2011.
- [50] Markus Greiner, Cindy A Regal, and Deborah S Jin. Emergence of a molecular Bose-Einstein condensate from a Fermi gas. *Nature*, 426(6966):537, 2003.
- [51] Martin W Zwierlein, Claudiu A Stan, Christian H Schunck, Sebastian MF Raupach, Subhadeep Gupta, Zoran Hadzibabic, and Wolfgang Ketterle. Observation of Bose-Einstein condensation of molecules. *Physical Review Letters*, 91(25):250401, 2003.
- [52] K-K Ni, S Ospelkaus, D Wang, G Quéméner, B Neyenhuis, MHG De Miranda, JL Bohn, J Ye, and DS Jin. Dipolar collisions of polar molecules in the quantum regime. *Nature*, 464(7293):1324, 2010.
- [53] S Ospelkaus, K-K Ni, D Wang, MHG De Miranda, B Neyenhuis, G Quéméner, PS Julienne, JL Bohn, DS Jin, and J Ye. Quantum-state controlled chemical reactions of ultracold potassium-rubidium molecules. *Science*, 327(5967):853–857, 2010.
- [54] Bo Yan, Steven A Moses, Bryce Gadway, Jacob P Covey, Kaden RA Hazzard, Ana Maria Rey, Deborah S Jin, and Jun Ye. Observation of dipolar spin-exchange interactions with lattice-confined polar molecules. *Nature*, 501(7468):521, 2013.

- [55] Mingwu Lu, Nathaniel Q Burdick, and Benjamin L Lev. Quantum degenerate dipolar Fermi gas. *Physical Review Letters*, 108(21):215301, 2012.
- [56] Igor Ferrier-Barbut, Holger Kadau, Matthias Schmitt, Matthias Wenzel, and Tilman Pfau. Observation of quantum droplets in a strongly dipolar Bose gas. *Physical Review Letters*, 116(21):215301, 2016.
- [57] Yu B Ovchinnikov, JH Müller, MR Doery, EJD Vredenburg, K Helmerston, SL Rolston, and WD Phillips. Diffraction of a released Bose-Einstein condensate by a pulsed standing light wave. *Physical Review Letters*, 83(2):284, 1999.
- [58] Oliver Morsch and Markus Oberthaler. Dynamics of Bose-Einstein condensates in optical lattices. *Reviews of Modern Physics*, 78(1):179, 2006.
- [59] Markus Greiner, Olaf Mandel, Tilman Esslinger, Theodor W Hänsch, and Immanuel Bloch. Quantum phase transition from a superfluid to a Mott insulator in a gas of ultracold atoms. *Nature*, 415(6867):39, 2002.
- [60] Immanuel Bloch, Jean Dalibard, and Wilhelm Zwerger. Many-body physics with ultracold gases. *Reviews of Modern Physics*, 80(3):885, 2008.
- [61] Waseem S Bakr, Jonathon I Gillen, Amy Peng, Simon Fölling, and Markus Greiner. A quantum gas microscope for detecting single atoms in a Hubbard-regime optical lattice. *Nature*, 462(7269):74, 2009.
- [62] Waseem S Bakr, Amy Peng, M Eric Tai, Ruichao Ma, Jonathan Simon, Jonathon I Gillen, Simon Foelling, Lode Pollet, and Markus Greiner. Probing the superfluid-to-Mott insulator transition at the single-atom level. *Science*, 329(5991):547–550, 2010.
- [63] Jacob F Sherson, Christof Weitenberg, Manuel Endres, Marc Cheneau, Immanuel Bloch, and Stefan Kuhr. Single-atom-resolved fluorescence imaging of an atomic Mott insulator. *Nature*, 467(7311):68, 2010.
- [64] Lawrence W Cheuk, Matthew A Nichols, Melih Okan, Thomas Gersdorf, Vinay V Ramasesh, Waseem S Bakr, Thomas Lompe, and Martin W Zwierlein. Quantum-gas microscope for fermionic atoms. *Physical Review Letters*, 114(19):193001, 2015.

- [65] Maxwell F Parsons, Florian Huber, Anton Mazurenko, Christie S Chiu, Widagdo Setiawan, Katherine Wooley-Brown, Sebastian Blatt, and Markus Greiner. Site-resolved imaging of fermionic Li 6 in an optical lattice. *Physical Review Letters*, 114(21):213002, 2015.
- [66] Ahmed Omran, Martin Boll, Timon A Hilker, Katharina Kleinlein, Guillaume Salomon, Immanuel Bloch, and Christian Gross. Microscopic observation of Pauli blocking in degenerate fermionic lattice gases. *Physical Review Letters*, 115(26):263001, 2015.
- [67] Elmar Haller, James Hudson, Andrew Kelly, Dylan A Cotta, Bruno Peaudecerf, Graham D Bruce, and Stefan Kuhr. Single-atom imaging of fermions in a quantum-gas microscope. *Nature Physics*, 11(9):738, 2015.
- [68] GJA Edge, R Anderson, D Jervis, DC McKay, R Day, S Trotzky, and JH Thywissen. Imaging and addressing of individual fermionic atoms in an optical lattice. *Physical Review A*, 92(6):063406, 2015.
- [69] Laurent Sanchez-Palencia and Maciej Lewenstein. Disordered quantum gases under control. *Nature Physics*, 6(2):87, 2010.
- [70] Thomas Uehlinger, Gregor Jotzu, Michael Messer, Daniel Greif, Walter Hofstetter, Ulf Bissbort, and Tilman Esslinger. Artificial graphene with tunable interactions. *Physical Review Letters*, 111(18):185307, 2013.
- [71] Gregor Jotzu, Michael Messer, Rémi Desbuquois, Martin Lebrat, Thomas Uehlinger, Daniel Greif, and Tilman Esslinger. Experimental realization of the topological Haldane model with ultracold fermions. *Nature*, 515(7526):237, 2014.
- [72] Monika Aidelsburger, Marcos Atala, Michael Lohse, Julio T Barreiro, B Paredes, and Immanuel Bloch. Realization of the Hofstadter Hamiltonian with ultracold atoms in optical lattices. *Physical Review Letters*, 111(18):185301, 2013.
- [73] Hirokazu Miyake, Georgios A Siviloglou, Colin J Kennedy, William Cody Burton, and Wolfgang Ketterle. Realizing the Harper Hamiltonian with laser-assisted tunneling in optical lattices. *Physical Review Letters*, 111(18):185302, 2013.
- [74] Y-J Lin, K Jiménez-García, and Ian B Spielman. Spin-orbit-coupled Bose-Einstein condensates. *Nature*, 471(7336):83, 2011.

- [75] Victor Galitski and Ian B Spielman. Spin-orbit coupling in quantum gases. *Nature*, 494(7435):49, 2013.
- [76] Lianghai Huang, Zengming Meng, Pengjun Wang, Peng Peng, Shao-Liang Zhang, Liangchao Chen, Donghao Li, Qi Zhou, and Jing Zhang. Experimental realization of two-dimensional synthetic spin-orbit coupling in ultracold Fermi gases. *Nature Physics*, 12(6):540, 2016.
- [77] Daniel Greif, Thomas Uehlinger, Gregor Jotzu, Leticia Tarruell, and Tilman Esslinger. Short-range quantum magnetism of ultracold fermions in an optical lattice. *Science*, 340(6138):1307–1310, 2013.
- [78] Russell A Hart, Pedro M Duarte, Tsung-Lin Yang, Xinxing Liu, Thereza Paiva, Ehsan Khatami, Richard T Scalettar, Nandini Trivedi, David A Huse, and Randall G Hulet. Observation of antiferromagnetic correlations in the Hubbard model with ultracold atoms. *Nature*, 519(7542):211, 2015.
- [79] Anton Mazurenko, Christie S Chiu, Geoffrey Ji, Maxwell F Parsons, Márton Kanász-Nagy, Richard Schmidt, Fabian Grusdt, Eugene Demler, Daniel Greif, and Markus Greiner. A cold-atom Fermi-Hubbard antiferromagnet. *Nature*, 545(7655):462, 2017.
- [80] Timon A Hilker, Guillaume Salomon, Fabian Grusdt, Ahmed Omran, Martin Boll, Eugene Demler, Immanuel Bloch, and Christian Gross. Revealing hidden antiferromagnetic correlations in doped Hubbard chains via string correlators. *Science*, 357(6350):484–487, 2017.
- [81] Peter T Brown, Debayan Mitra, Elmer Guardado-Sanchez, Peter Schauf, Stanimir S Kondov, Ehsan Khatami, Thereza Paiva, Nandini Trivedi, David A Huse, and Waseem S Bakr. Spin-imbalance in a 2D Fermi-Hubbard system. *Science*, 357(6358):1385–1388, 2017.
- [82] Jean-Philippe Brantut, Jakob Meineke, David Stadler, Sebastian Krinner, and Tilman Esslinger. Conduction of ultracold fermions through a mesoscopic channel. *Science*, 337(6098):1069–1071, 2012.
- [83] Sebastian Krinner, David Stadler, Dominik Husmann, Jean-Philippe Brantut, and Tilman Esslinger. Observation of quantized conductance in neutral matter. *Nature*, 517(7532):64, 2015.
- [84] Y. I. Manin. *Vychislimoe i Nevychislimoe (Computable and Noncomputable)*. Sovetskoye Radio, 1980.

- [85] Richard P Feynman. Simulating physics with computers. *International Journal of Theoretical Physics*, 21(6-7):467–488, 1982.
- [86] Maciej Lewenstein, Anna Sanpera, and Verònica Ahufinger. *Ultracold Atoms in Optical Lattices: Simulating quantum many-body systems*. Oxford University Press, 2012.
- [87] Michael Schreiber, Sean S Hodgman, Pranjal Bordia, Henrik P Lüschen, Mark H Fischer, Ronen Vosk, Ehud Altman, Ulrich Schneider, and Immanuel Bloch. Observation of many-body localization of interacting fermions in a quasi-random optical lattice. *Science*, 349(6250):842–845, 2015.
- [88] René Harald Reimann. Quantum Gases in State-Dependent Optical Potentials. Master’s thesis, Stony Brook University, SUNY, 2009.
- [89] Daniel Alexander Pertot. *Two-Component Bosons in State-Dependent Optical Lattices*. PhD thesis, Stony Brook University, SUNY, 2011.
- [90] Bryce Russell Gadway. *Bose Gases in Tailored Optical and Atomic Lattices*. PhD thesis, Stony Brook University, SUNY, 2012.
- [91] Jeremy Brian Reeves. *Dynamics of Atomic Matter Waves in Optical Lattices*. PhD thesis, Stony Brook University, SUNY, 2015.
- [92] Daniel Pertot, Bryce Gadway, and Dominik Schneble. Collinear Four-Wave Mixing of Two-Component Matter Waves. *Physical Review Letters*, 104:200402, 2010.
- [93] Bryce Gadway, Daniel Pertot, René Reimann, and Dominik Schneble. Superfluidity of Interacting Bosonic Mixtures in Optical Lattices. *Physical Review Letters*, 105:045303, 2010.
- [94] Bryce Gadway, Daniel Pertot, Jeremy Reeves, Matthias Vogt, and Dominik Schneble. Glassy Behavior in a Binary Atomic Mixture. *Physical Review Letters*, 107:145306, 2011.
- [95] Bryce Gadway, Daniel Pertot, Jeremy Reeves, and Dominik Schneble. Probing an ultracold-atom crystal with matter waves. *Nature Physics*, 8(7):544–549, 2012.
- [96] J. Reeves, L. Krinner, M. Stewart, A. Pazmiño, and D. Schneble. Nonadiabatic diffraction of matter waves. *Physical Review A*, 92:023628, 2015.

- [97] Angel Rivas and Susana F Huelga. *Open Quantum Systems*. Springer, 2012.
- [98] Ulrich Weiss. *Quantum dissipative systems*, volume 13. World Scientific, 2012.
- [99] Ingrid Rotter and JP Bird. A review of progress in the physics of open quantum systems: theory and experiment. *Reports on Progress in Physics*, 78(11):114001, 2015.
- [100] V. Weisskopf and E. Wigner. Berechnung der natürlichen Linienbreite auf Grund der Diracschen Lichttheorie. *Zeitschrift für Physik*, 63(1):54–73, 1930.
- [101] E. M. Purcell. Spontaneous Emission Probabilities at Radio Frequencies. *Physical Review*, 69:681, 1946.
- [102] Pierre Meystre and Murray Sargent III. *Elements of Quantum Optics*. Springer Verlag Berlin Heidelberg, 2007.
- [103] Vladimir P Bykov. Spontaneous emission from a medium with a band spectrum. *Soviet Journal of Quantum Electronics*, 4(7):861, 1975.
- [104] Sajeew John. Strong localization of photons in certain disordered dielectric superlattices. *Physical Review Letters*, 58:2486–2489, 1987.
- [105] Eli Yablonovitch. Inhibited Spontaneous Emission in Solid-State Physics and Electronics. *Physical Review Letters*, 58:2059–2062, 1987.
- [106] Daniel Kleppner. Inhibited Spontaneous Emission. *Physical Review Letters*, 47:233–236, 1981.
- [107] Eli Yablonovitch, TJ Gmitter, and KM Leung. Photonic band structure: The face-centered-cubic case employing nonspherical atoms. *Physical Review Letters*, 67(17):2295, 1991.
- [108] Shawn-yu Lin, JG Fleming, DL Hetherington, BK Smith, R Biswas, KM Ho, MM Sigalas, W Zubrzycki, SR Kurtz, and Jim Bur. A three-dimensional photonic crystal operating at infrared wavelengths. *Nature*, 394(6690):251, 1998.
- [109] Michael D. Tocci, Michael Scalora, Mark J. Bloemer, Jonathan P. Dowling, and Charles M. Bowden. Measurement of spontaneous-emission enhancement near the one-dimensional photonic band edge of semiconductor heterostructures. *Physical Review A*, 53(4):2799–2803, 1996.

- [110] EP Petrov, VN Bogomolov, II Kalosha, and SV Gaponenko. Spontaneous emission of organic molecules embedded in a photonic crystal. *Physical Review Letters*, 81(1):77, 1998.
- [111] SG Romanov, AV Fokin, and RM De La Rue. Eu 3+ emission in an anisotropic photonic band gap environment. *Applied Physics Letters*, 76(13):1656–1658, 2000.
- [112] Shinpei Ogawa, Masahiro Imada, Susumu Yoshimoto, Makoto Okano, and Susumu Noda. Control of Light Emission by 3D Photonic Crystals. *Science*, 305(5681):227–229, 2004.
- [113] Peter Lodahl, A. Floris van Driel, Ivan S. Nikolaev, Arie Irman, Karin Overgaag, Daniel Vanmaekelbergh, and Willem L. Vos. Controlling the dynamics of spontaneous emission from quantum dots by photonic crystals. *Nature*, 430(7000):654–657, 2004.
- [114] Michael Barth, Roman Schuster, Achim Gruber, and Frank Cichos. Imaging single quantum dots in three-dimensional photonic crystals. *Physical Review Letters*, 96(24):243902, 2006.
- [115] Qin Wang, Søren Stobbe, and Peter Lodahl. Mapping the local density of optical states of a photonic crystal with single quantum dots. *Physical Review Letters*, 107(16):167404, 2011.
- [116] Ulrich Hoeppe, Christian Wolff, Jens Küchenmeister, Jens Niegemann, Malte Drescher, Hartmut Benner, and Kurt Busch. Direct Observation of Non-Markovian Radiation Dynamics in 3D Bulk Photonic Crystals. *Physical Review Letters*, 108(4):043603, 2012.
- [117] Qiong Liu, Hongwei Song, Wei Wang, Xue Bai, Yu Wang, Biao Dong, Lin Xu, and Wei Han. Observation of Lamb shift and modified spontaneous emission dynamics in the YBO 3: Eu 3+ inverse opal. *Optics Letters*, 35(17):2898–2900, 2010.
- [118] S-P Yu, JD Hood, JA Muniz, MJ Martin, Richard Norte, C-L Hung, Seán M Meenehan, Justin D Cohen, Oskar Painter, and HJ Kimble. Nanowire photonic crystal waveguides for single-atom trapping and strong light-matter interactions. *Applied Physics Letters*, 104(11):111103, 2014.

- [119] A Goban, C-L Hung, S-P Yu, JD Hood, JA Muniz, JH Lee, MJ Martin, AC McClung, KS Choi, Darrick E Chang, et al. Atom-light interactions in photonic crystals. *Nature Communications*, 5:3808, 2014.
- [120] A. Goban, C. L. Hung, J. D. Hood, S. P. Yu, J. A. Muniz, O. Painter, and H. J. Kimble. Superradiance for Atoms Trapped Along a Photonic Crystal Waveguide. *Physical Review Letters*, 115(6):063601, 2015.
- [121] Jonathan D. Hood, Akihisa Goban, Ana Asenjo-Garcia, Mingwu Lu, Su-Peng Yu, Darrick E. Chang, and H. J. Kimble. Atom-atom interactions around the band edge of a photonic crystal waveguide. *Proceedings of the National Academy of Sciences*, 113(38):10507–10512, 2016.
- [122] Yanbing Liu and Andrew A. Houck. Quantum electrodynamics near a photonic bandgap. *Nature Physics*, 13(1):48–52, 2017.
- [123] Neereja M Sundaresan, Rex Lundgren, Guanyu Zhu, Alexey V Gorshkov, and Andrew A Houck. Interacting Qubit-Photon Bound States with Superconducting Circuits. *arXiv preprint arXiv:1801.10167*, 2018.
- [124] Inés de Vega, Diego Porras, and J. Ignacio Cirac. Matter-Wave Emission in Optical Lattices: Single Particle and Collective Effects. *Physical Review Letters*, 101:260404, 2008.
- [125] Carlos Navarrete-Benlloch, Inés de Vega, Diego Porras, and J Ignacio Cirac. Simulating quantum-optical phenomena with cold atoms in optical lattices. *New Journal of Physics*, 13(2):023024, 2011.
- [126] Michael Stewart, Ludwig Krinner, Arturo Pazmiño, and Dominik Schneble. Analysis of non-Markovian coupling of a lattice-trapped atom to free space. *Physical Review A*, 95:013626, 2017.
- [127] Inés de Vega and Daniel Alonso. Dynamics of non-Markovian open quantum systems. *Reviews of Modern Physics*, 89:015001, 2017.
- [128] Sajeev John and Jian Wang. Quantum optics of localized light in a photonic band gap. *Physical Review B*, 43:12772–12789, 1991.
- [129] Ludwig Krinner, Michael Stewart, Arturo Pazmiño, and Dominik Schneble. In situ magnetometry for experiments with atomic quantum gases. *Review of Scientific Instruments*, 89(1):013108, 2018.

- [130] Wolfgang Ketterle, Dallin S Durfee, and DM Stamper-Kurn. Making, probing and understanding Bose-Einstein condensates. *arXiv preprint cond-mat/9904034*, 1999.
- [131] Stephan Gerhard Albert. Cooling, Trapping, and Transport of Atom Clouds. Master's thesis, Stony Brook University, SUNY, 2007.
- [132] Daniel Günther Greif. Evaporative cooling and Bose-Einstein Condensation of Rb-87 in a moving-coil TOP trap geometry. Master's thesis, Stony Brook University, SUNY, 2007.
- [133] David E Sproles. Laser Spectroscopy and Magneto-Optical Trapping of Rubidium Atoms. Master's thesis, The Graduate School, Stony Brook University: Stony Brook, NY., 2008.
- [134] Daniel Pertot, Daniel Greif, Stephan Albert, Bryce Gadway, and Dominik Schneble. Versatile transporter apparatus for experiments with optically trapped Bose-Einstein condensates. *Journal of Physics B: Atomic, Molecular and Optical Physics*, 42(21):215305, 2009.
- [135] C. J. Pethick and H. Smith. *Bose-Einstein Condensation in Dilute Gases*. Cambridge University Press, 2nd edition edition, 2008.
- [136] D. Wineland and H. Dehmelt. Proposed  $10^{14}\Delta\nu < \nu$  Laser Fluorescence Spectroscopy on Tl+ Mono-Ion Oscillator III. *Bulletin of the American Physical Society*, 20:637, 1975.
- [137] Theodor W Hänsch and Arthur L Schawlow. Cooling of gases by laser radiation. *Optics Communications*, 13(1):68–69, 1975.
- [138] E. L. Raab, M. Prentiss, Alex Cable, Steven Chu, and D. E. Pritchard. Trapping of Neutral Sodium Atoms with Radiation Pressure. *Physical Review Letters*, 59:2631–2634, 1987.
- [139] AM Steane, M Chowdhury, and CJ Foot. Radiation force in the magneto-optical trap. *Journal of the Optical Society of America B*, 9(12):2142–2158, 1992.
- [140] Steven Chu, Leo Hollberg, John E Bjorkholm, Alex Cable, and Arthur Ashkin. Three-dimensional viscous confinement and cooling of atoms by resonance radiation pressure. *Physical Review Letters*, 55(1):48, 1985.

- [141] Paul D Lett, Richard N Watts, Christoph I Westbrook, William D Phillips, Phillip L Gould, and Harold J Metcalf. Observation of atoms laser cooled below the Doppler limit. *Physical Review Letters*, 61(2):169, 1988.
- [142] Jean Dalibard and Claude Cohen-Tannoudji. Laser cooling below the Doppler limit by polarization gradients: simple theoretical models. *Journal of the Optical Society of America B*, 6(11):2023–2045, 1989.
- [143] Harold J Metcalf and Peter Van der Straten. *Laser cooling and trapping of neutral atoms*. Wiley Online Library, 2007.
- [144] Daniel A. Steck. Rubidium 87 d line data, available online at <http://steck.us/alkalidata> (revision 2.1.5, 13 january 2015). *Rubidium 87 D Line Data, available online at <http://steck.us/alkalidata>*, revision 2.1.5, 13 January 2015.
- [145] Alan L Migdall, John V Prodan, William D Phillips, Thomas H Bergeman, and Harold J Metcalf. First observation of magnetically trapped neutral atoms. *Physical Review Letters*, 54(24):2596, 1985.
- [146] Wolfgang Petrich, Michael H. Anderson, Jason R. Ensher, and Eric A. Cornell. Stable, Tightly Confining Magnetic Trap for Evaporative Cooling of Neutral Atoms. *Physical Review Letters*, 74:3352–3355, 1995.
- [147] Yu T Baiborodov, MS Ioffe, VM Petrov, and RI Sobolev. An adiabatic trap with combined magnetic field. *Journal of Nuclear Energy. Part C, Plasma Physics, Accelerators, Thermonuclear Research*, 5(6):409, 1963.
- [148] David E. Pritchard. Cooling Neutral Atoms in a Magnetic Trap for Precision Spectroscopy. *Physical Review Letters*, 51:1336–1339, 1983.
- [149] Myoung-Sun Heo, Jae-yoon Choi, and Yong-il Shin. Fast production of large  $^{23}\text{Na}$  Bose-Einstein condensates in an optically plugged magnetic quadrupole trap. *Physical Review A*, 83:013622, 2011.
- [150] R. Dubessy, K. Merloti, L. Longchambon, P.-E. Pottie, T. Liennard, A. Perrin, V. Lorent, and H. Perrin. Rubidium-87 Bose-Einstein condensate in an optically plugged quadrupole trap. *Physical Review A*, 85:013643, 2012.
- [151] Rudolf Grimm, Matthias Weidemüller, and Yurii B Ovchinnikov. Optical dipole traps for neutral atoms. In *Advances in Atomic, Molecular, and Optical Physics*, pages 95–170. Elsevier, 2000.

- [152] Harald F Hess. Evaporative cooling of magnetically trapped and compressed spin-polarized hydrogen. *Physical Review B*, 34(5):3476, 1986.
- [153] Charles S Adams, Heun Jin Lee, Nir Davidson, Mark Kasevich, and Steven Chu. Evaporative cooling in a crossed dipole trap. *Physical Review Letters*, 74(18):3577, 1995.
- [154] MD Barrett, JA Sauer, and MS Chapman. All-optical formation of an atomic Bose-Einstein condensate. *Physical Review Letters*, 87(1):010404, 2001.
- [155] Walther Gerlach and Otto Stern. Der experimentelle Nachweis der Richtungsquantelung im Magnetfeld. *Zeitschrift für Physik*, 9(1):349–352, 1922.
- [156] Phillip L Gould, George A Ruff, and David E Pritchard. Diffraction of atoms by light: The near-resonant Kapitza-Dirac effect. *Physical Review Letters*, 56(8):827, 1986.
- [157] Bryce Gadway, Daniel Pertot, René Reimann, Martin G Cohen, and Dominik Schneble. Analysis of Kapitza-Dirac diffraction patterns beyond the Raman-Nath regime. *Optics Express*, 17(21):19173–19180, 2009.
- [158] Subhadeep Gupta, Aaron E Leanhardt, Alexander D Cronin, and David E Pritchard. Coherent manipulation of atoms with standing light waves. *Comptes Rendus Academy of Sciences*, 2(3):479–495, 2001.
- [159] Bryce Gadway, Jeremy Reeves, Ludwig Krinner, and Dominik Schneble. Evidence for a Quantum-to-Classical Transition in a Pair of Coupled Quantum Rotors. *Physical Review Letters*, 110:190401, 2013.
- [160] L. Deng, E. W. Hagley, J. Denschlag, J. E. Simsarian, Mark Edwards, Charles W. Clark, K. Helmerson, S. L. Rolston, and W. D. Phillips. Temporal, Matter-Wave-Dispersion Talbot Effect. *Physical Review Letters*, 83:5407–5411, 1999.
- [161] C. Ryu, M. F. Andersen, A. Vaziri, M. B. d’Arcy, J. M. Grossman, K. Helmerson, and W. D. Phillips. High-Order Quantum Resonances Observed in a Periodically Kicked Bose-Einstein Condensate. *Physical Review Letters*, 96:160403, 2006.

- [162] Isidor I Rabi, Sidney Millman, P Kusch, and Jerrold Reinach Zacharias. The Molecular Beam Resonance Method for Measuring Nuclear Magnetic Moments. The Magnetic Moments of  ${}^6\text{Li}$ ,  ${}^7\text{Li}$  and  ${}^{19}\text{F}$ . *Physical Review*, 55(6):526, 1939.
- [163] G. Breit and I. I. Rabi. Measurement of Nuclear Spin. *Physical Review*, 38(11):2082–2083, 1931.
- [164] Alan Corney. *Atomic and laser spectroscopy*. Clarendon Press Oxford, 1978.
- [165] Ivan H. Deutsch and Poul S. Jessen. Quantum-state control in optical lattices. *Physical Review A*, 57(3):1972–1986, 1998.
- [166] D. McKay and B. DeMarco. Thermometry with spin-dependent lattices. *New Journal of Physics*, 12, 2010.
- [167] D. C. McKay and B. DeMarco. Cooling in strongly correlated optical lattices: prospects and challenges. *Reports on Progress in Physics*, 74(5):054401, 2011.
- [168] David C McKay, Carolyn Meldgin, David Chen, and Brian DeMarco. Slow thermalization between a lattice and free Bose gas. *Physical Review Letters*, 111(6):063002, 2013.
- [169] R Scelle, T Rentrop, A Trautmann, T Schuster, and MK Oberthaler. Motional coherence of fermions immersed in a Bose gas. *Physical Review Letters*, 111(7):070401, 2013.
- [170] T. Rentrop, A. Trautmann, F. A. Olivares, F. Jendrzejewski, A. Komnik, and M. K. Oberthaler. Observation of the Phononic Lamb Shift with a Synthetic Vacuum. *Physical Review X*, 6:041041, 2016.
- [171] Felix Schmidt, Daniel Mayer, Michael Hohmann, Tobias Lausch, Farina Kindermann, and Artur Widera. Precision measurement of the Rb 87 tune-out wavelength in the hyperfine ground state  $F=1$  at 790 nm. *Physical Review A*, 93(2):022507, 2016.
- [172] Daniel Mayer, Felix Schmidt, Daniel Adam, Steve Haupt, Jennifer Koch, Tobias Lausch, Jens Nettersheim, Quentin Bouton, and Artur Widera. Controlled doping of a bosonic quantum gas with single neutral atoms. *arXiv preprint arXiv:1805.01313*, 2018.

- [173] LJ LeBlanc and JH Thywissen. Species-specific optical lattices. *Physical Review A*, 75(5):053612, 2007.
- [174] Felix Bloch. Über die Quantenmechanik der Elektronen in Kristallgittern. *Zeitschrift für Physik*, 52(7-8):555–600, 1929.
- [175] Charles Kittel. *Introduction to solid state physics*. Wiley New York, 1996.
- [176] JK Freericks and H Monien. Phase diagram of the Bose-Hubbard model. *Europhysics Letters*, 26(7):545, 1994.
- [177] Gretchen K Campbell, Jongchul Mun, Micah Boyd, Patrick Medley, Aaron E Leanhardt, Luis G Marcassa, David E Pritchard, and Wolfgang Ketterle. Imaging the Mott insulator shells by using atomic clock shifts. *Science*, 313(5787):649–652, 2006.
- [178] John H Moore, Christopher C Davis, Michael A Coplan, and Sandra C Greer. *Building scientific apparatus*. Cambridge University Press, 2009.
- [179] Custom Thermoelectric. <https://customthermoelectric.com/products/water-blocks/water-blocks.html>. Accessed: 2018-06-18.
- [180] David R Lide et al. *CRC handbook of chemistry and physics*. CRC Boca Raton, 2012.
- [181] Thorlabs. [https://www.thorlabs.com/navigation.cfm?guide\\_id=2224](https://www.thorlabs.com/navigation.cfm?guide_id=2224). Accessed: 2018-07-10.
- [182] Thomas Volz, Stephan Dürr, Sebastian Ernst, Andreas Marte, and Gerhard Rempe. Characterization of elastic scattering near a Feshbach resonance in 87 Rb. *Physical Review A*, 68(1):010702, 2003.
- [183] Michael Erhard. *Experimente mit mehrkomponentigen Bose-Einstein-Kondensaten*. PhD thesis, Universität Hamburg, 2004.
- [184] Jochen Kronjäger. *Coherent dynamics of spinor Bose-Einstein condensates*. PhD thesis, Universität Hamburg, 2007.
- [185] CF Ockeloen, AF Tauschinsky, RJC Spreeuw, and S Whitlock. Detection of small atom numbers through image processing. *Physical Review A*, 82(6):061606, 2010.

- [186] Xiaolin Li, Min Ke, Bo Yan, and Yuzhu Wang. Reduction of interference fringes in absorption imaging of cold atom cloud using eigenface method. *Chinese Optics Letters*, 5(3):128–130, 2007.
- [187] Ian Jolliffe. Principal component analysis. In *International encyclopedia of statistical science*, pages 1094–1096. Springer, 2011.
- [188] Lawrence Sirovich and Michael Kirby. Low-dimensional procedure for the characterization of human faces. *Journal of the Optical Society of America A*, 4(3):519–524, 1987.
- [189] Jeffery A Hanson and Haw Yang. A general statistical test for correlations in a finite-length time series. *The Journal of Chemical Physics*, 128(21):214101, 2008.
- [190] Dan M. Stamper-Kurn and Masahito Ueda. Spinor Bose gases: Symmetries, magnetism, and quantum dynamics. *Reviews of Modern Physics*, 85(3):1191–1244, 2013.
- [191] I. K. Kominis, T. W. Kornack, J. C. Allred, and M. V. Romalis. A sub-femtotesla multichannel atomic magnetometer. *Nature*, 422(6932):596–599, 2003.
- [192] W. Wasilewski, K. Jensen, H. Krauter, J. J. Renema, M. V. Balabas, and E. S. Polzik. Quantum Noise Limited and Entanglement-Assisted Magnetometry. *Physical Review Letters*, 104(13):133601, 2010.
- [193] Stephan Wildermuth, Sebastian Hofferberth, Igor Lesanovsky, Elmar Haller, L. Mauritz Andersson, Sonke Groth, Israel Bar-Joseph, Peter Kruger, and Jörg Schmiedmayer. Bose-Einstein condensates: Microscopic magnetic-field imaging. *Nature*, 435(7041):440–440, 2005.
- [194] M. Vengalattore, J. M. Higbie, S. R. Leslie, J. Guzman, L. E. Sadler, and D. M. Stamper-Kurn. High-Resolution Magnetometry with a Spinor Bose-Einstein Condensate. *Physical Review Letters*, 98(20), 2007.
- [195] Fan Yang, Alicia J. Kollár, Stephen F. Taylor, Richard W. Turner, and Benjamin L. Lev. Scanning Quantum Cryogenic Atom Microscope. *Physical Review Applied*, 7(3):034026, 2017.
- [196] W. Muessel, H. Strobel, D. Linnemann, D. B. Hume, and M. K. Oberthaler. Scalable spin squeezing for quantum-enhanced magnetometry with Bose-Einstein condensates. *Physical Review Letters*, 113(10):103004, 2014.

- [197] Pascal Böhi, Max F. Riedel, Johannes Hoffrogge, Jakob Reichel, Theodor W. Hänsch, and Philipp Treutlein. Coherent manipulation of Bose-Einstein condensates with state-dependent microwave potentials on an atom chip. *Nature Physics*, 5(8):592–597, 2009.
- [198] Christian Groß. *Spin-squeezing and nonlinear atom-interferometry with Bose-Einstein condensates*. PhD thesis, Universität Heidelberg, 2010.
- [199] N. Lundblad, P. J. Lee, I. B. Spielman, B. L. Brown, W. D. Phillips, and J. V. Porto. Atoms in a Radio-Frequency-Dressed Optical Lattice. *Physical Review Letters*, 100:150401, 2008.
- [200] A. Recati, P. O. Fedichev, W. Zwerger, J. von Delft, and P. Zoller. Atomic Quantum Dots Coupled to a Reservoir of a Superfluid Bose-Einstein Condensate. *Physical Review Letters*, 94(4), 2005.
- [201] Peter P. Orth, Ivan Stanic, and Karyn Le Hur. Dissipative quantum Ising model in a cold-atom spin-boson mixture. *Physical Review A*, 77(5), 2008.
- [202] J. M. Taylor, P. Cappellaro, L. Childress, L. Jiang, D. Budker, P. R. Hemmer, A. Yacoby, R. Walsworth, and M. D. Lukin. High-sensitivity diamond magnetometer with nanoscale resolution. *Nature Physics*, 4(10):810–816, 2008.
- [203] Bartington Magnetometers. <http://www.bartington.com/presentation/mag-03-three-axis-magnetic-field-sensor>. Accessed: 2018-08-02.
- [204] Paul Adrien Maurice Dirac. The quantum theory of the emission and absorption of radiation. *Proceedings of the Royal Society of London A*, 114(767):243–265, 1927.
- [205] P. W. Milonni. *The Quantum Vacuum: An Introduction to Quantum Electrodynamics*. Academic Press, Inc., 1994.
- [206] Yoshihisa Yamamoto and Atac Imamoglu. *Mesoscopic quantum optics*. John Wiley & Sons, Inc., New York, 1999.
- [207] Hans A Bethe. The electromagnetic shift of energy levels. *Physical Review*, 72(4):339, 1947.

- [208] Ludwig Krinner, Michael Stewart, Arturo Pazmiño, Joonhyuk Kwon, and Dominik Schneble. Spontaneous Emission in a Matter-Wave Open Quantum System. *arXiv preprint arXiv:1712.07791*, 2017.
- [209] Ludwig Krinner, Michael Stewart, Arturo Pazmiño, Joonhyuk Kwon, and Dominik Schneble. Spontaneous emission of matter waves from a tunable open quantum system. *Nature*, 559(7715):589–592, 2018.
- [210] Ángel Rivas and Susana F Huelga and Martin B Plenio. Quantum non-Markovianity: characterization, quantification and detection. *Reports on Progress in Physics*, 77(9):094001, 2014.
- [211] Heinz-Peter Breuer, Elsi-Mari Laine, Jyrki Piilo, and Bassano Vacchini. Colloquium: Non-Markovian dynamics in open quantum systems. *Reviews of Modern Physics*, 88(2):021002, 2016.
- [212] R. Miller, T. E. Northup, K. M. Birnbaum, A. Boca, A. D. Boozer, and H. J. Kimble. Trapped atoms in cavity QED: coupling quantized light and matter. *Journal of Physics B: Atomic, Molecular and Optical Physics*, 38(9):S551, 2005.
- [213] Herbert Walther, Benjamin TH Varcoe, Berthold-Georg Englert, and Thomas Becker. Cavity quantum electrodynamics. *Reports on Progress in Physics*, 69(5):1325, 2006.
- [214] Serge Haroche and Jean-Michel Raimond. *Exploring the quantum: atoms, cavities, and photons*. Oxford University Press, 2006.
- [215] P Lambropoulos, Georgios M Nikolopoulos, Torben R Nielsen, and Søren Bay. Fundamental quantum optics in structured reservoirs. *Reports on Progress in Physics*, 63(4):455, 2000.
- [216] Sajeev John and Jian Wang. Quantum electrodynamics near a photonic band gap: Photon bound states and dressed atoms. *Physical Review Letters*, 64:2418–2421, 1990.
- [217] J. S. Douglas, H Habibian, C. L. Hung, A. V. Gorshkov, H. J. Kimble, and D. E. Chang. Quantum many-body models with cold atoms coupled to photonic crystals. *Nature Photonics*, 9(5):326–331, 2015.
- [218] R. H. Dicke. Coherence in Spontaneous Radiation Processes. *Physical Review*, 93(1):99–110, 1954.

- [219] K. Rzażewski, M. Lewenstein, and J. H. Eberly. Threshold effects in strong-field photodetachment. *Journal of Physics B: Atomic and Molecular Physics*, 15:L661–L667, 1982.
- [220] M. Lewenstein and K. Rzażewski. Quantum anti-Zeno effect. *Physical Review A*, 61:022105, 2000.
- [221] Martin Bruderer, Alexander Klein, Stephen R. Clark, and Dieter Jaksch. Polaron physics in optical lattices. *Physical Review A*, 76:011605, 2007.
- [222] Michael Tavis and Frederick W Cummings. Exact solution for an N-molecule-radiation-field Hamiltonian. *Physical Review*, 170(2):379, 1968.
- [223] A González-Tudela and JI Cirac. Non-Markovian Quantum Optics with Three-Dimensional State-Dependent Optical Lattices. *arXiv preprint arXiv:1806.02528*, 2018.
- [224] T Shi, Y-H Wu, A González-Tudela, and JI Cirac. Effective many-body Hamiltonians of qubit-photon bound states. *arXiv preprint arXiv:1806.02527*, 2018.
- [225] Russell Anderson. *Nonequilibrium dynamics and relative phase evolution of two-component Bose-Einstein condensates*. PhD thesis, Swinburne University, 2010.
- [226] Anthony J Leggett, SDAFMGA Chakravarty, AT Dorsey, Matthew PA Fisher, Anupam Garg, and W Zwerger. Dynamics of the dissipative two-state system. *Reviews of Modern Physics*, 59(1):1, 1987.
- [227] AM Kaufman, RP Anderson, Thomas M Hanna, Eite Tiesinga, Paul S Julienne, and DS Hall. Radio-frequency dressing of multiple Feshbach resonances. *Physical Review A*, 80(5):050701, 2009.
- [228] Artur Widera, Olaf Mandel, Markus Greiner, Susanne Kreim, Theodor W Hänsch, and Immanuel Bloch. Entanglement interferometry for precision measurement of atomic scattering properties. *Physical Review Letters*, 92(16):160406, 2004.
- [229] Aviv Keshet and Wolfgang Ketterle. A distributed, graphical user interface based, computer control system for atomic physics experiments. *Review of Scientific Instruments*, 84(1):015105, 2013.
- [230] Amy Wan-Chih Peng. *Quantum gas microscope with optical lattice*. PhD thesis, Harvard University, 2010.

[231] Embedded Micro. <https://embeddedmicro.com/products/mojo-v3>.  
Accessed: 2018-07-06.

# Appendix A

## Simulation of Mean-Field Shift

In this chapter we briefly summarize the simulation used to estimate the residual mean field shift in chapter 7. When weakly coupling (compared to  $E_{2r} = 4\hbar^2 k_r^2 / 2m$ ) a weakly trapped 3D-BEC to a lattice-trapped state, the lattice trapped state will experience significantly higher densities (compared to the non-lattice trapped state) due to the compression into the lattice wells. This changes the mean-field energy or interaction energy of the system, which results in a density dependent shift of the resonance frequency. We estimate this shift here directly using numerical simulation. We begin with the two component, coupled, time dependent Gross Pitaevskii-equation (TDGPE) in one dimension [135, 225]:

$$\begin{aligned} i\hbar\partial_t\psi_1 &= \left[ -\frac{\hbar^2\partial_x^2}{2m} + V_1(x) + g_{11}|\psi_1|^2 + g_{12}|\psi_2|^2 + \frac{\hbar\Delta}{2} \right] \psi_1 \\ &\quad + \frac{\hbar\Omega}{2}\psi_2 \\ i\hbar\partial_t\psi_2 &= \left[ -\frac{\hbar^2\partial_x^2}{2m} + V_2(x) + g_{22}|\psi_2|^2 + g_{12}|\psi_1|^2 - \frac{\hbar\Delta}{2} \right] \psi_2 \\ &\quad + \frac{\hbar\Omega}{2}\psi_1. \end{aligned} \tag{A.1}$$

Here, we have two species with wavefunctions  $\psi_1(x)$  and  $\psi_2(x)$   $g_{11}$  and  $g_{22}$  are the intra-species interaction parameters and  $g_{12}$  is the inter-species interaction parameter.  $V_{\{1,2\}}(x)$  are the potentials for either species and  $\Delta$  and  $\Omega$  are the detuning and Rabi-frequency known from Rabi oscillations.

We numerically integrate Eqns. A.1 directly, starting with all population in  $\psi_1$ . The potential  $V_1(x)$  is simply a harmonic trap centered at  $x = 0$  with  $\omega = 2\pi \times 72$  Hz, and the potential  $V_2(x) = V_1(x) + 30E_r \sin(k_r x)^2$ . The spatial distribution  $\psi_1(x)$  has minimum energy (is in the ground state). The ratio

of the interaction parameters  $g_{11}$  and the total atom number  $\int |\psi_1|^2(x)dx$  are set such that initially  $g_{11} |\psi_1(0)|^2 \approx \hbar \times 2\pi \times 750$  Hz, which is approximately the mean field energy of a  $3 \times 10^4$ -atom BEC in a 72 Hz trap. We then time evolve for  $400 \mu s$  the using variable detuning and a  $\Omega = 2\pi \times 630$  Hz coupling strength used in the experiment to create a simulation of the lattice spectrum seen in Fig. 7.4.

We simulate Eqns. A.1 for both, interactions turned to zero, and for interactions turned to the relative values of  $^{87}\text{Rb}$ . The result is shown in Fig. A.1. We can see that for the low numbers and low population transfer used in our experiment the interaction shift is indeed negligible (less than 100 Hz) and thus negligible for the experiments described in chapter 7.

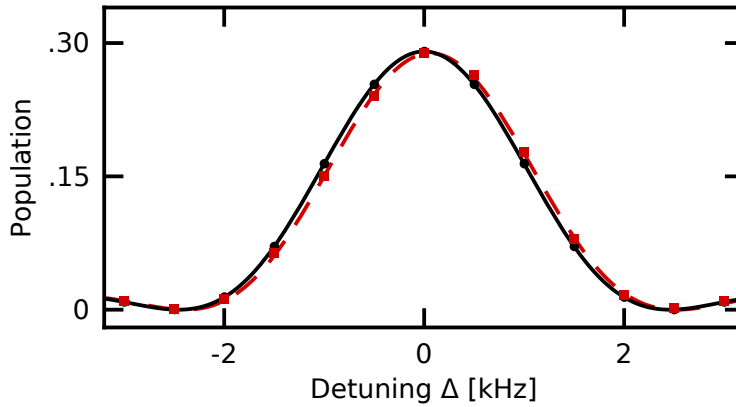


Figure A.1: Spectrum obtained via simulation of coupled time dependent Gross-Pitaevskii equation A.1. Coupling strength is  $\Omega = 2\pi \times 630$  Hz, pulse time is  $\tau = 400 \mu s$ . The red squares are with interactions turned on, and the black circles are with interactions turned off. The solid black line and the dashed red line are fits to the black circles and red squares respectively (fit function is Eq. 2.4). Relative shift of the two curve-centers is  $\delta\Delta = 2\pi \times 64$  Hz.

# Appendix B

## Other Measurements

During my PhD, we have also conducted a few measurements which detail other aspects of our apparatus, but that do not quite fit the context of the main dissertation. We will briefly describe them here, since they may be important for future experiments.

### B.1 Controlling the Scattering Length: Interspecies Feshbach Resonances

In previous dissertations from our group [89–91] there was a focus also on interacting Bose-Hubbard models (BHM [59]) and spin-boson models [200,201,226]. An important feature here is the interspecies s-wave scattering length which details the point-interaction of bosons.

Ultracold atomic bosons (such as  $^{87}\text{Rb}$ ) usually interact in such a way, that it can be described using only an effective contact interactions. This is called the s-wave scattering regime, where a single parameter (the s-wave scattering length  $a_s$ ) fully describes the interaction of two particles, with the interaction energy given by

$$\epsilon_I = \int dx 4\pi a_s \hbar^2 n(x)^2 / m$$

where  $n(x) = |\Psi(x)|^2$  is the density of atoms in space and  $\Psi(x)$  is the many-body wavefunction of the atoms. The scattering length  $a_s$  is determined by the far-field phase-shift that occurs when a low energy wavefunction scatters on a potential (e. g. a wavefunction scattering off a barrier, or one atom scattering off another atoms). A positive (negative) scattering length translates to repulsive (attractive) effective interactions.

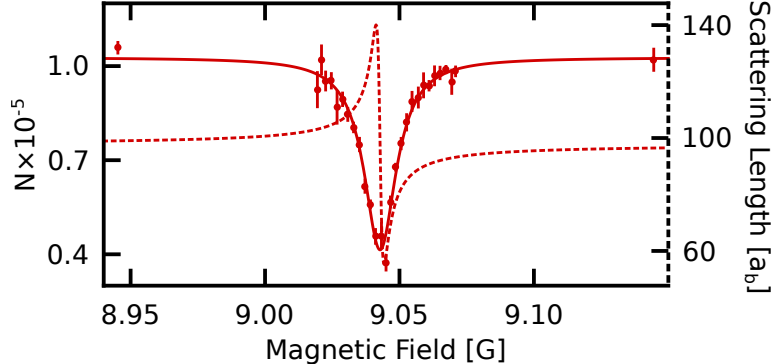


Figure B.1: Interspecies Feshbach resonance. Total atom vs. magnetic field of a mixture of  $|2, 0\rangle$  and  $|1, 1\rangle$ -atoms (46(7)% are  $|F = 2, m_F = 0\rangle$ ), showing a loss signal at 9.0428(2) G (systematic uncertainty of up to 2 mG not included). The solid line is a Lorentzian fit to the data of width 14(1) mG, signifying the presence of an inelastic Feshbach resonance between the two states. The dashed line (labeled by the dashed axis) is the expected modification of the real part of the scattering length, centered at the center of the loss feature (other parameters taken from [227]).

Since the scattering phase-shift depends on the microscopic details of the potential landscape between the atoms as their separation decreases, one can tune  $a_s$  using a so-called Feshbach resonance [34, 35]. Here the change in the microscopic interaction at zero incident wave energy occurs due to bound molecular states coming into resonance (i. e. when a molecular bound state approaches zero binding energy). These molecular states can usually be tuned relative to the free wavefunctions using magnetic fields.

Feshbach resonances can furthermore obtain imaginary character if different freely propagating states (different from the input states) are energetically allowed, causing two-body losses to become greatly enhanced. Typically Feshbach resonances are measured using losses (due to enhancement of two- or three-body losses) but the real part of the s-wave scattering length can also be measured directly, e. g. through interferometry [228].

In our apparatus we are specifically interested in inter-species Feshbach resonances, where in Fig. B.1 we observe a loss feature when two species are in our optical trap and we scan the magnetic field, indicating the presence of an inelastic Feshbach resonance. The scattering length takes the form [227]:

$$a(B) = a_{BG} \left( 1 - \frac{\Delta B}{B - B_0 - i\gamma_B/2} \right)$$

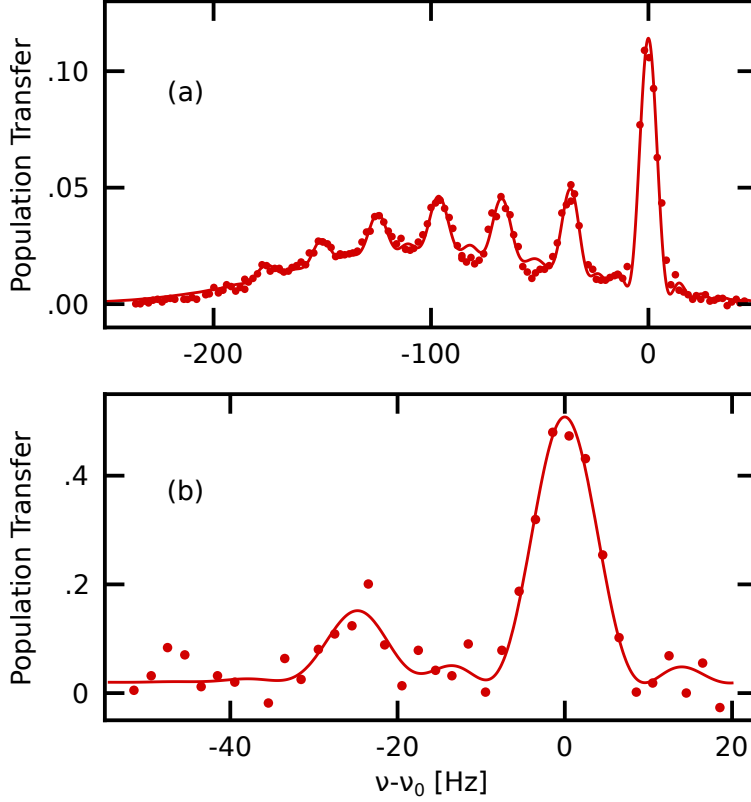


Figure B.2: Two-photon spectroscopy of a Mott-insulator. Relative population transfer to the  $|2, 1\rangle$ -state from the  $|1, -1\rangle$ -state for two-photon radio-frequency spectroscopy using a 100 ms pulse. The atoms sit in a 3-D deeply confining optical lattice of spacing 532 nm and depth  $30 E_{r,1064}$  (a) Result of spectroscopy for  $190(5) \times 10^3$  atoms, showing sites which are populated by up to 7 atoms. (b) Result of spectroscopy for  $5(1) \times 10^3$  atoms. A second peak is barely visible.

where  $a_{BG}$  is the background scattering length,  $B_0$  is the center of the Feshbach resonance,  $\Delta B$  is the width (zero crossing if the resonance were fully elastic) and  $\gamma_B$  is the inelastic width. The interaction energy can then be calculated by the real part of the scattering length only, while the imaginary part induces two-body losses.

We see a well resolved loss feature when approaching a field of  $9.043(2)$  G (value measured in [227] is  $9.0448(5)$  G), indicating the presence of the inelastic Feshbach resonance and hence control also over the real part of the scattering length and the interaction energies.

## B.2 Measuring Mott-Shell Populations

Following an experiment conducted by [177] we became interested in the occupation number of our atomic Mott insulators. We prepared a Mott-insulating sample of  $|1, -1\rangle$  atoms by loading them into a deep ( $30E_{r,1064}$  depth) 3-D lattice of lattice spacing 532 nm. We then dial the magnetic field to 3.23 G where the differential quadratic shift between  $|1, -1\rangle$  and  $|2, 1\rangle$  vanishes, allowing us to use pulses of  $\sim 1$  Hz coupling strength and as long as 100 ms. This allows for highly accurate spectroscopy which can resolve the shift in scattering length between  $|1, -1\rangle \leftrightarrow |1, -1\rangle$  and  $|1, -1\rangle \leftrightarrow |2, 1\rangle$  (which is  $100.4 a_b$  vs.  $97.7 a_b$  (where  $a_b$  is the bohr radius). We use microwave radiation at  $\sim 6.8$  GHz and radio-frequency radiation at  $\sim 2$  MHz, resulting in an effective two-photon Rabi-Frequency of less than 5 Hz.

Results are shown in Fig. B.2 where we can clearly see populations of up to 7 atoms per site for high total atom numbers (on top of a thermal background) whereas for low total atom numbers we can see at most 2 atoms per site.

# Appendix C

## Electronics

We regularly develop and maintain in-house built electronics, as part of daily laboratory operation. Here we present a few important electronic schematics which were built during my time in the group.

### C.1 AC-line Trigger

The ac-line trigger (see Fig. C.1) is implemented with the help of the Cicero and Atticus Software [229] and an Opal Kelly XEM3001 Spartan-3 FPGA (field programmable gate array). We implement a simple Schmitt-trigger circuit (see appendix C.2) connected to the AC-mains, which generates a 0 – 5 V trigger signal to synchronize with the AC line signal. The FPGA board is programmed by Cicero/Atticus using the manual instructions to wait for the next high signal at the re-trigger input pin (in this case pins JP2-46 (signal) and JP2-49 (ground)) immediately before starting any magnetic field sensitive measurements. The FPGA is programmed to generate and distribute timing information/triggers to the computer’s analog and digital cards based on an internal crystal oscillator which creates a master clock at frequency 10 MHz, from which slower frequencies are derived to time the experimental sequence, thus enabling the necessary wait for synchronization with the line after evaporation and before sensitive experiments.

### C.2 Schmitt-Trigger Circuit

As mentioned in section C.1 we use a Schmitt-trigger-type circuit to derive a clock signal which is line-synchronous. The circuit is shown in Fig. C.2. We use op-amps to create a standard Schmitt-trigger circuit. The input pin

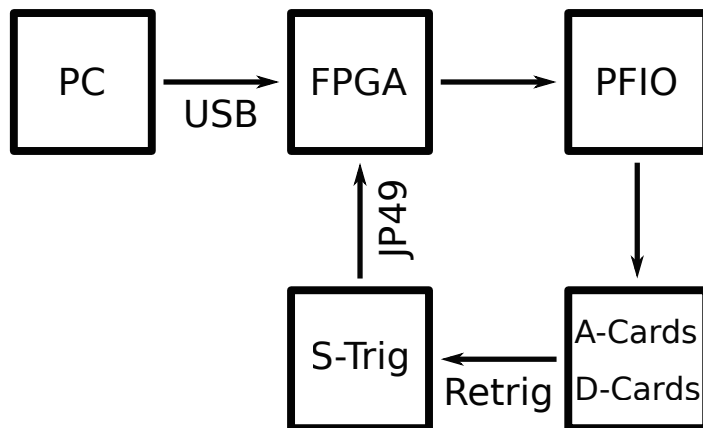


Figure C.1: Schematic of the setup for the line trigger. The computer communicates the details for the entire experimental sequence to the FPGA board via USB. The FPGA board generates timing for the sequences at variable time resolution. The timing is sent to the computer via the PFIO input. Before magnetically sensitive experiments, the FPGA halts, and the digital outputs enable the Schmitt-trigger circuit to go high at the start of the next AC-clock cycle. The retrigger signal is sent to a dedicated pin on the FPGA which then resumes the sequence.

for the FPGA is value sensing, not edge sensing, hence if the trigger signal is given directly to the FPGA, it would start when the Schmitt-trigger is high, and not (as is required for us) at the same phase during each AC-cycle. To circumvent this problem, we first pass the trigger signal through a Q-flip-flop which is clocked by the Schmitt trigger. The input to the Schmitt-trigger circuit is a digital output from the PC, which goes high only when a retrigger is requested, thus correctly communicating with the FPGA.

### C.3 Stable Amplified Photo-diodes.

Accurately stabilizing optical intensities is very important for the experiments in our laboratory. Following description in [230] we built temperature compensated photo-diode amplifiers which convert the photo-diode current into a measurable voltage which is not sensitive to drifts in temperature, using the AD8304 integrated circuit and a standard FDS-100 photo-diode from Thorlabs. The output of the circuit is the logarithm of photo-diode current.

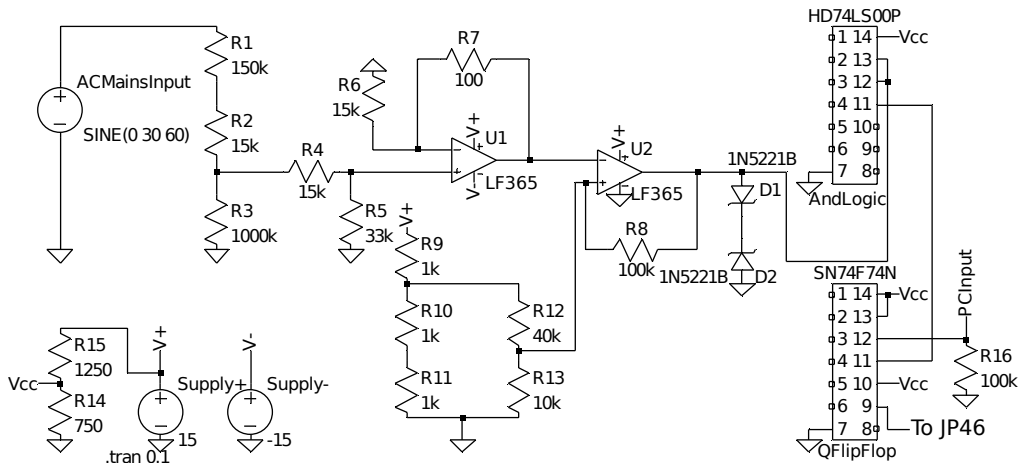


Figure C.2: Schmitt trigger circuit for line synchronization built using two LF365 operation-amplifiers. R12 and R13 are actually one trim-pot for adjusting the trigger phase. R14 and R15 are also a trim-pot for adjusting the Vcc drive voltage for the logic devices. The AndLogic device conditions the direct output of the Schmitt-trigger op-amp to proper logic levels and the Q-flip-flop blocks trigger signals until requested by the PC, digital control cards.

In order to incorporate this into a PI-stabilization loop we use an ADL-5330-EVAL variable gain amplifier (VGA) which is then connected to a Mini-circuits ZHL-1A power amplifier in order to drive an acousto-optic modulator (AOM). The RF-source which is amplified by the VGA is a Wenzel temperature stabilized crystal oscillator.

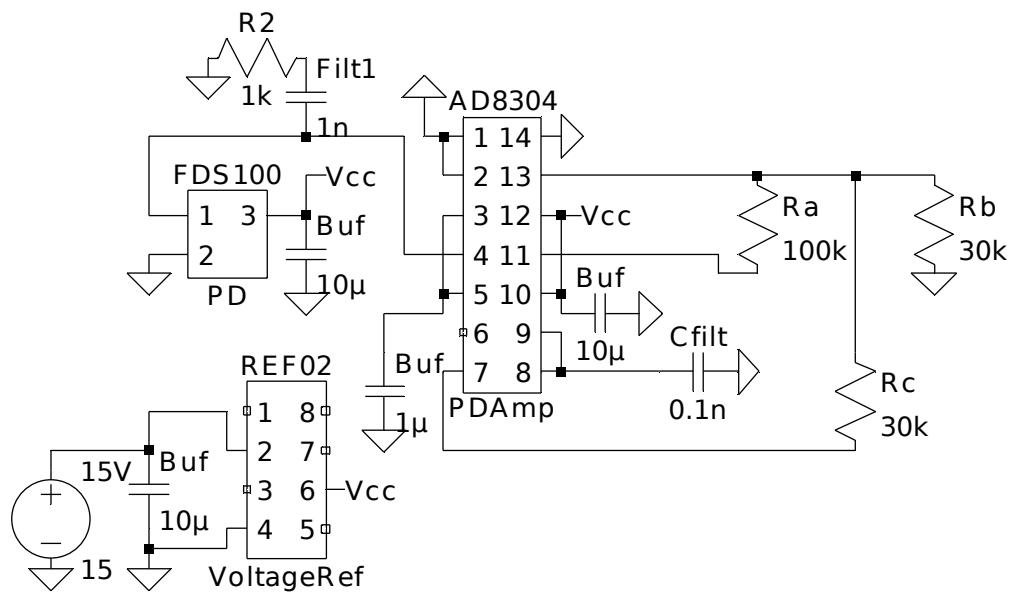


Figure C.3: Logarithmic temperature stabilized photo-diode amplifier, as used for the optical dipole trap. The sensitivity and minimum detectable optical intensity can be easily adjusted by changing resistors Ra, Rb and Rc (details in the data-sheet of AD8394).

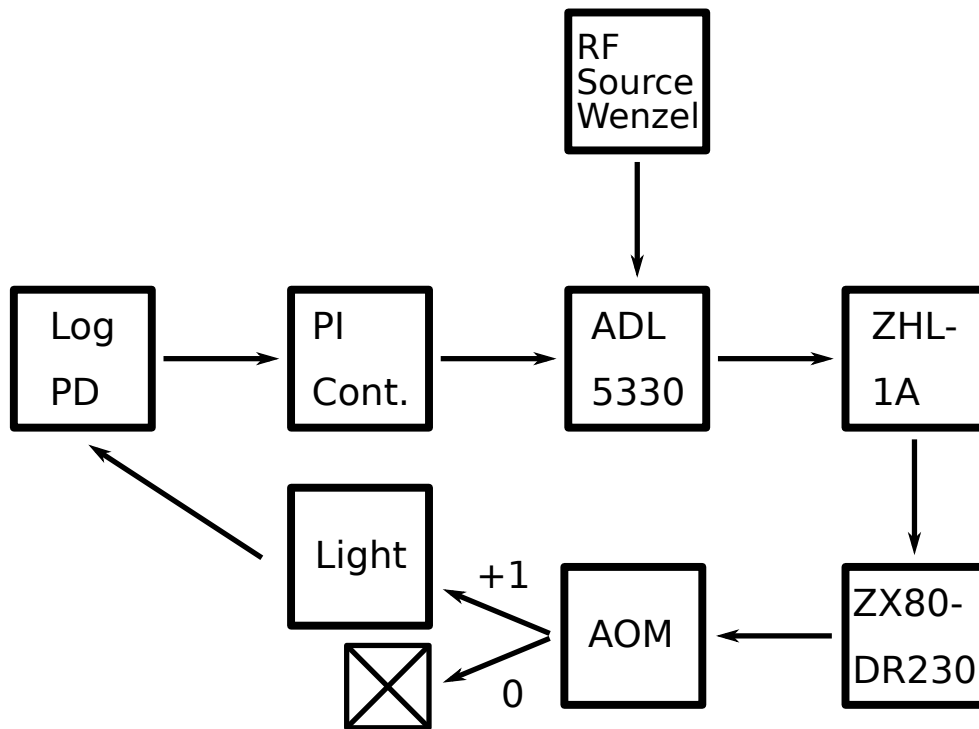


Figure C.4: Schematic for PI-control of optical intensity using logarithmic photo-diodes and variable gain amplifiers ADL5330.

## Appendix D

# Development of Smart Laboratory Devices

It was mentioned in section C.1 that we use an FPGA to generate a variable time base for synchronizing and timing our experiments. As a result of this we got interested in working more with FPGA devices and were able to find good introductory projects from colleagues at Stony Brook.

An FPGA (Field Programmable Gate Array) is a highly customizable digital electronic device which has a collection of typically  $10^4$  to  $10^6$  logic cells that can be interconnected arbitrarily to each other, and typically  $10^2$  in/out pins that can be freely defined by the user. As a result one can build arbitrary complex logic functions on these devices, or implement highly parallelized computations or data-acquisitions. FPGAs are a complementary device to microprocessor chips, which are very good and very fast at sequentially executing one complex task, while an FPGA is typically more geared towards parallel executions of many simpler tasks. The outstanding customizeability of FPGAs comes at the penalty of typically slower clock speeds ( $\sim 10^8$  Hz) compared to modern day processors ( $\sim 10^9$  Hz) and less ease of use for programming the device (FPGAs are typically still programmed closer to the actual machine logic than microprocessors which offer a wide variety of high-level programming environments, such as Matlab, Mathematica, or Python).

I will outline two projects on two different FPGA platforms that showcase how FPGAs can be used in an experimental physics laboratory, and that showcase the utility of these devices.

## D.1 Introductory Project: FPGA Based Down Counter for Ultrafast Experiments

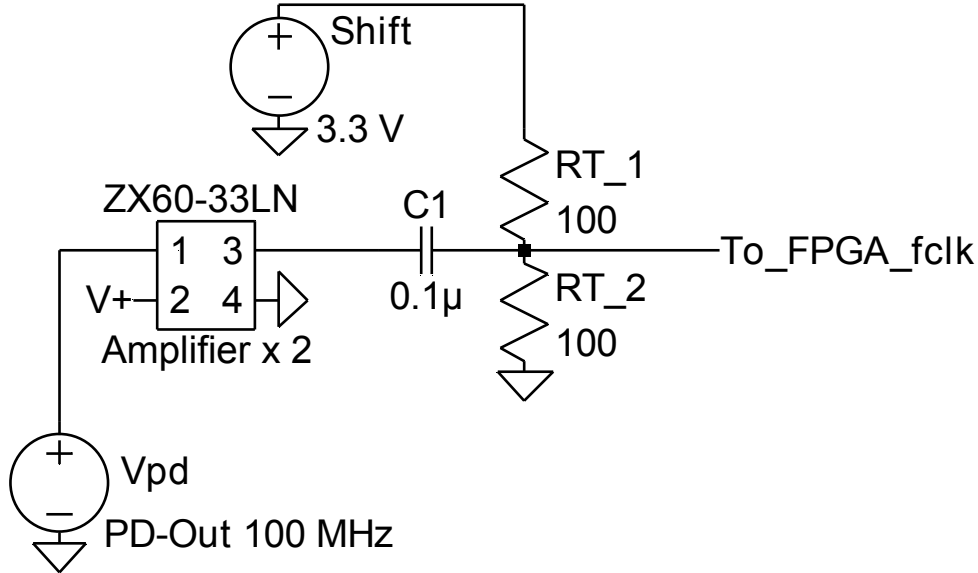


Figure D.1: Circuit used to condition photo-diode signal to reach logic levels in order to be used as a clock input to the FPGA.

An early project we did with FPGAs is to implement a so-called count-down circuit. I will describe it here since it is a very easy introductory project to familiarize oneself with FPGAs and the syntax of the programming language. Furthermore it perfectly showcases how easy it is on an FPGA to generate different clock frequencies from a master clock, which is the basis for the variable time-base used in the experiments (see section C.1).

The lab of T. Weihnacht utilizes a laser oscillator which generates ultra-short laser pulses ( $\sim 30$  fs) at a repetition rate of  $\sim 10^8$  Hz, which need to be amplified. Since other equipment (for example cameras) can usually only sustain a repetition rate of  $\sim 1$  kHz, the amplifier is only operated at a this repetition rate, while all other pulses are discarded. The lowered repetition rate of the amplifier and the other equipment has to be derived as an integer

multiple of the repetition rate of the laser-oscillator such that the amplifier and the camera remain properly synchronized with the laser oscillator.

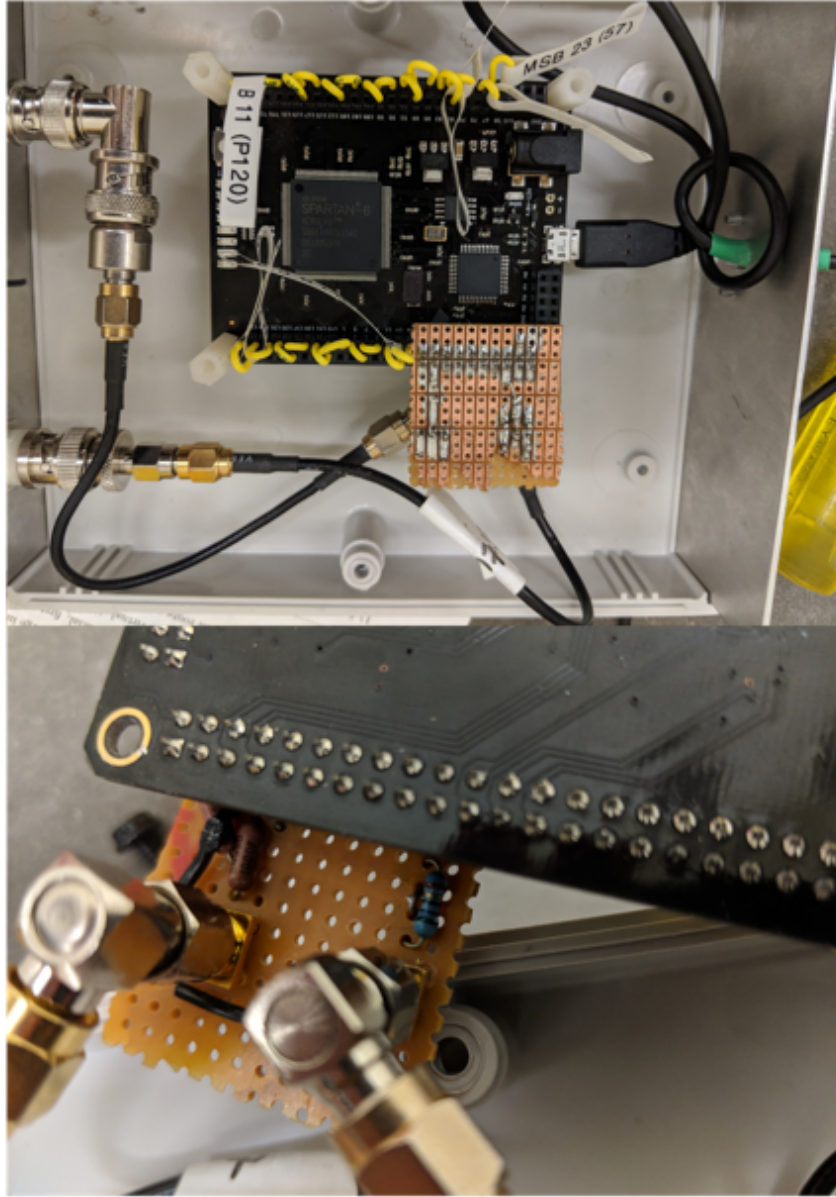


Figure D.2: Photographs of FPGA board (black) and photodiode conditioning circuit.

The current way of deriving a lowered repetition rate clock is to trigger a circuit made from IC-flip-flops and IC-decade counters using a photo-diode

signal which records the output of the laser-oscillator. The circuit effectively counts down the original frequency of the laser-oscillator and gives a trigger only once every  $\sim 10^5$ -th pulse, thus synchronizing the amplification and the experiment. In practice this requires careful soldering and patience when the circuit does break, and once constructed the circuit can only count down by one number, which cannot be easily changed.

It turns out that this task is relatively easy to implement using FPGA logic. In turn this makes the circuit more easy to customize and more easy to replace once broken, since the little soldering that is involved initially uses components that are less prone to failure and the main FPGA board can be easily bough off the shelf.

### D.1.1 Basic Idea: Code snippet

FPGA devices normally have no internal mechanism for clocking or synchronization; clocking or synchronization is usually supplied externally by the user or by a crystal oscillator on typical FPGA board which is directly connected to the FPGA-chip. This is the basic idea which the final device is based on. If we can condition the photo-diode signal which monitors the output power of the laser-oscillator sufficiently to use it as a ‘clock’, the implementation of the down-count circuit is straightforward. A ‘clock’ in this context is a signal which has a sharp rising edge which defines the start of each clock cycle. Typically it also has a duty cycle of 50% so that a typical clock will be a square-wave which is 0V half of the time and 3.3V% (or whatever the logic levels of the device are) the other half of the time. The only important feature of a clock is the sharp rising edge

The central code for this looks as follows:

```
always @ (posedge fclk)
//At each clock-edge execute this block
//fclk is the photo-diode signal
//counter_store is half the number the
//input clock is divided by
//sclk is the output clock
begin
//Beginning of block
    if (rst_n == 1'b0)
//Reset and read in new number
        begin
            counter <= 24'h000000;
            counter_store <= count_set;
        end
    else if (counter == counter_store)
//Invert output when count is reached
        begin
            counter <= 24'h000000;
            sclk <= ~sclk;
```

```

        end
        else
        //Increment counter
        begin
            counter <= counter + 1'b1;
        end
    end
end

```

where the variable `count_set` is set by the user by interconnecting various inputs pins to the FPGA, and the clock `fclk` is supplied externally by the user to a special clock pin. In the current setup, input pins can be directly connected to neighboring pins that are set permanently high or permanently low, which in turn programs a 24-bit number. The number is only updated upon reset to guarantee reliable operation. The variable `sclk` is directly connected to an output and can be used to trigger as it is logic level 3.3V-CMOS standard. All that is left is to supply a constraints file which defines which pins the inputs and outputs are connected to and a circuit which conditions the photo-diode signal.

## D.1.2 Hardware and Implementation

The hardware which this was implemented on was an Embedded Micro Mojo V3 [231]. The full source code and constraints files are listed at the end of this chapter and the circuit which was used to condition the photo-diode signal is shown in Fig. D.1. A photograph of the devices is shown in Fig. D.2.

## D.1.3 Entire Source Code

In the following I recreate the entire source code for this project. First is the base code which manages counting:

```

module downcounter(
input fclk ,
input [23:0] count_set ,
input rst_n ,
output sclk
);

//Front matter
//Counter Register For DownCounting
reg [23:0] counter = 24'h000000;
//Counter Register to store count to number
reg [23:0] counter_store = 24'h000FFF;
//Helper Register For Assigning Into Output
reg helper = 1'b0;
assign sclk = helper;
//assign cnt = counter;

always @ (posedge fclk)
begin
    if (rst_n == 1'b0)

```

```

begin
    counter <= 24'h000000;
    counter_store <= count_set;
end
else if (counter == counter_store)
begin
    counter <= 24'h000000;
    helper <= ~helper;
end
else
begin
    counter <= counter + 1'b1;
end
end
endmodule

```

Second is the top or wrapper module which manages auxiliary variables:

```

module mojo_top(
input fclk ,
input [23:0] count_set ,
input rst_n ,
output sclk ,
output [23:0] highs ,
output [23:0] lows ,
output led
);
reg halp = 1'b0;
assign lows = 24'h000000;
assign highs = 24'hFFFFFF;
assign led = halp;
always @ (posedge fclk)
begin
    if (rst_n == 1'b0)
begin
        halp = 1'b1;
end
else
begin
        halp = 1'b0;
end
end

downcounter inst_downcount (
.fclk(fclk),
.count_set(count_set),
.rst_n(rst_n),
.sclk(sclk)
);
endmodule

```

And this is the entire constraints file:

```

NET "fclk" LOC = P51 | IOSTANDARD = LVCMOS33;
NET "sclk" LOC = P24 | IOSTANDARD= LVCMOS33;
NET "rst_n" LOC = P38 | IOSTANDARD = LVCMOS33;
NET "count_set<23>" LOC = P57 | IOSTANDARD = LVTTTL;
NET "count_set<22>" LOC = P74 | IOSTANDARD = LVTTTL;
NET "count_set<21>" LOC = P78 | IOSTANDARD = LVTTTL;
NET "count_set<20>" LOC = P82 | IOSTANDARD = LVTTTL;

```

```

NET "count_set<19>" LOC = P84 | IOSTANDARD = LVTTTL;
NET "count_set<18>" LOC = P92 | IOSTANDARD = LVTTTL;
NET "count_set<17>" LOC = P94 | IOSTANDARD = LVTTTL;
NET "count_set<16>" LOC = P99 | IOSTANDARD = LVTTTL;
NET "count_set<15>" LOC = P101 | IOSTANDARD = LVTTTL;
NET "count_set<14>" LOC = P111 | IOSTANDARD = LVTTTL;
NET "count_set<13>" LOC = P114 | IOSTANDARD = LVTTTL;
NET "count_set<12>" LOC = P118 | IOSTANDARD = LVTTTL;
NET "count_set<11>" LOC = P120 | IOSTANDARD = LVTTTL;
NET "count_set<10>" LOC = P123 | IOSTANDARD = LVTTTL;
NET "count_set<9>" LOC = P131 | IOSTANDARD = LVTTTL;
NET "count_set<8>" LOC = P133 | IOSTANDARD = LVTTTL;
NET "count_set<7>" LOC = P139 | IOSTANDARD = LVTTTL;
NET "count_set<6>" LOC = P141 | IOSTANDARD = LVTTTL;
NET "count_set<5>" LOC = P1 | IOSTANDARD = LVTTTL;
NET "count_set<4>" LOC = P5 | IOSTANDARD = LVTTTL;
NET "count_set<3>" LOC = P9 | IOSTANDARD = LVTTTL;
NET "count_set<2>" LOC = P11 | IOSTANDARD = LVTTTL;
NET "count_set<1>" LOC = P16 | IOSTANDARD = LVTTTL;
NET "count_set<0>" LOC = P21 | IOSTANDARD = LVTTTL;
NET "highs<23>" LOC = P58 | IOSTANDARD = LVTTTL;
NET "highs<22>" LOC = P75 | IOSTANDARD = LVTTTL;
NET "highs<21>" LOC = P79 | IOSTANDARD = LVTTTL;
NET "highs<20>" LOC = P83 | IOSTANDARD = LVTTTL;
NET "highs<19>" LOC = P85 | IOSTANDARD = LVTTTL;
NET "highs<18>" LOC = P93 | IOSTANDARD = LVTTTL;
NET "highs<17>" LOC = P95 | IOSTANDARD = LVTTTL;
NET "highs<16>" LOC = P100 | IOSTANDARD = LVTTTL;
NET "highs<15>" LOC = P102 | IOSTANDARD = LVTTTL;
NET "highs<14>" LOC = P112 | IOSTANDARD = LVTTTL;
NET "highs<13>" LOC = P115 | IOSTANDARD = LVTTTL;
NET "highs<12>" LOC = P119 | IOSTANDARD = LVTTTL;
NET "highs<11>" LOC = P121 | IOSTANDARD = LVTTTL;
NET "highs<10>" LOC = P124 | IOSTANDARD = LVTTTL;
NET "highs<9>" LOC = P132 | IOSTANDARD = LVTTTL;
NET "highs<8>" LOC = P134 | IOSTANDARD = LVTTTL;
NET "highs<7>" LOC = P140 | IOSTANDARD = LVTTTL;
NET "highs<6>" LOC = P142 | IOSTANDARD = LVTTTL;
NET "highs<5>" LOC = P2 | IOSTANDARD = LVTTTL;
NET "highs<4>" LOC = P6 | IOSTANDARD = LVTTTL;
NET "highs<3>" LOC = P10 | IOSTANDARD = LVTTTL;
NET "highs<2>" LOC = P12 | IOSTANDARD = LVTTTL;
NET "highs<1>" LOC = P17 | IOSTANDARD = LVTTTL;
NET "highs<0>" LOC = P22 | IOSTANDARD = LVTTTL;
NET "lows<23>" LOC = P66 | IOSTANDARD = LVTTTL;
NET "lows<22>" LOC = P67 | IOSTANDARD = LVTTTL;
NET "lows<21>" LOC = P80 | IOSTANDARD = LVTTTL;
NET "lows<20>" LOC = P81 | IOSTANDARD = LVTTTL;
NET "lows<19>" LOC = P87 | IOSTANDARD = LVTTTL;
NET "lows<18>" LOC = P88 | IOSTANDARD = LVTTTL;
NET "lows<17>" LOC = P97 | IOSTANDARD = LVTTTL;
NET "lows<16>" LOC = P98 | IOSTANDARD = LVTTTL;
NET "lows<15>" LOC = P104 | IOSTANDARD = LVTTTL;
NET "lows<14>" LOC = P105 | IOSTANDARD = LVTTTL;
NET "lows<13>" LOC = P116 | IOSTANDARD = LVTTTL;
NET "lows<12>" LOC = P117 | IOSTANDARD = LVTTTL;
#lows<11> and not assigned, GND nearby, use GND;
#NET "lows<10>" LOC = P126 | IOSTANDARD = LVTTTL;
#Not set, use LED pin, serves dual purpose of LED and low pin;
NET "lows<9>" LOC = P127 | IOSTANDARD = LVTTTL;

```

```

NET "lows<8>" LOC = P137 | IOSTANDARD = LVTTTL;
NET "lows<7>" LOC = P138 | IOSTANDARD = LVTTTL;
NET "lows<6>" LOC = P143 | IOSTANDARD = LVTTTL;
NET "lows<5>" LOC = P144 | IOSTANDARD = LVTTTL;
NET "lows<4>" LOC = P7 | IOSTANDARD = LVTTTL;
NET "lows<3>" LOC = P8 | IOSTANDARD = LVTTTL;
NET "lows<2>" LOC = P14 | IOSTANDARD = LVTTTL;
NET "lows<1>" LOC = P15 | IOSTANDARD = LVTTTL;
NET "lows<0>" LOC = P26 | IOSTANDARD = LVTTTL;
#Set lows<11> and lows<10> in order
#to be able to synthesize the circuit.
NET "lows<11>" LOC = P29 | IOSTANDARD = LVTTTL;
NET "lows<10>" LOC = P30 | IOSTANDARD = LVTTTL;
NET "led" LOC = P126 | IOSTANDARD = LVTTTL;

```

The pinout is also visualized in Fig. D.3 for clarity, where the Figure represents the layout of the board which was used.

Pin		P22	P17	P15	P12	P10	P8	P6	P2	P144	P142	P140	P138	P134	P132	P127	P124		P24
H/L Bit		H	H	L	H	H	L	H	H	L	H	H	L	H	H	L	H		sclk
H/L Bit	L	0	1	L	2	3	L	4	5	L	6	7	L	8	9	L	10		fclk
Pin	P26	P21	P16	P14	P11	P9	P7	P5	P1	P143	P141	P139	P137	P133	P131	P126	P123		P51

Pin	P58	P67	P75	P79	P81	P83	P85	P88	P93	P95	P98	P100	P102	P105	P112	P115	P117	P119	P121
H/L Bit	H	L	H	H	L	H	H	L	H	H	L	H	H	L	H	H	L	H	H
H/L Bit	23	L	22	21	L	20	19	L	18	17	L	16	15	L	14	13	L	12	11
Pin	P57	P66	P74	P78	P80	P82	P84	P87	P92	P94	P97	P99	P101	P104	P111	P114	P116	P118	P120

Figure D.3: Pinout visualization for downcounter circuit, to visualize how to set bits.

## D.2 Outlook

In the future one can use more advanced FPGA devices like the Red Pitaya which already has DA-chips and AD-chips installed for live signal processing or fast PID stabilization of signals.